DEVELOPING AND TESTING A COUPLED REGIONAL MODELING SYSTEM FOR ESTABLISHING AN INTEGRATED MODELING AND OBSERVATIONAL FRAMEWORK FOR DUST AEROSOL

A Thesis
Presented to
The Academic Faculty

by

Anton S. Darmenov

In Partial Fulfillment
of the Requirements for the Degree
Doctor of Philosophy in the
School of Earth and Atmospheric Sciences

Georgia Institute of Technology
May 2009

DEVELOPING AND TESTING A COUPLED REGIONAL MODELING SYSTEM FOR ESTABLISHING AN INTEGRATED MODELING AND OBSERVATIONAL FRAMEWORK FOR DUST AEROSOL

Approved by:

Professor Irina Sokolik, Adviser
School of Earth and Atmospheric Sciences
Georgia Institute of Technology

Professor Judith Curry
School of Earth and Atmospheric Sciences
Georgia Institute of Technology

Associate Professor Athanasios Nenes
School of Earth and Atmospheric Sciences & School of Chemical and Biomolecular Engineering
Georgia Institute of Technology

Associate Professor Marc Stieglitz
School of Earth and Atmospheric Sciences & School of Civil and Environmental Engineering
Georgia Institute of Technology

Dr. Olga Kalashnikova
Jet Propulsion Laboratory
NASA

Date Approved: December 15, 2008

To all my teachers,

who showed me the beauty of knowledge.

ACKNOWLEDGEMENTS

First, I would like to express my gratitude to my advisor, Dr. Sokolik, whose expertise, understanding, and patience, added considerably to my graduate experience. I would also like to thank Dr. Curry, Dr. Kalashnikova, Dr. Nenes and Dr. Stieglitz for agreeing to be on my thesis committee despite their extremely busy schedules.

Many thanks to my friends and family. In particular, I must acknowledge my wife and best friend, Kremena, without whose love, encouragement and editing assistance, I would not have finished this thesis. I would like to thank my friends Anton Ouzounov, Zornitsa Krasteva, Dimitar Krastev and Lennon Haas for proofreading this manuscript. And finally, thanks to my cats Elmo and Leopolde, whose purring and constant need for attention relaxed me during the stressful times.

The research in this dissertation was funded in part by the NASA and ONR grants.

TABLE OF CONTENTS

LIST OF TABLES

LIST OF FIGURES

SUMMARY

The impact of mineral dust aerosols upon climate has been a topic of active research during the last decade. To this date, estimates of the climate response to mineral dust remain largely uncertain because of our limited capability to quantify dust distribution in the atmosphere. Focusing on the Central and East Asian dust source regions, this thesis aims to develop a coupled regional dust modeling system to provide an improved modeling capability of atmospheric dust as well as to aid the integration of ground-based and satellite observations. The specific objectives of this study are as follows: 1) evaluate the capabilities of the available data to detect and quantify mineral dust in the atmosphere; 2) develop and test a coupled regional dust modeling system able to simulate size resolved dust concentrations accounting for the regional specifics of Central and East Asia; and 3) outline a methodology for data and modeling integration.

The capabilities of ground-based and satellite data to characterize dust in the atmosphere are examined in great details. Based on analysis of MODIS data reflectance and radiances, we found evidence for regional signature of dust in near-IR and proposed a new probabilistic dust-cloud mask that explicitly takes into account the spatial variability characteristics of dust aerosols. These findings can aid to the development of new algorithms for dust detection and discrimination from clouds, improving the overall quality of satellite remote sensing of dust.

We developed a coupled regional dust modeling system (WRF-DuMo) by incorporating a dust emission module (DuMo) into the community NCAR Weather Research Forecast (WRF) model. The WRF-DuMo unique capabilities include explicit treatment of land surface properties in Central and East Asia, a suite of dust emission schemes with different levels of complexity, multiple options for dust injection in the atmosphere and flexible

parameters of the initial size distribution of emitted dust. Such capabilities allow for the first time to bracket within a single modeling system the uncertainties associated with modeling the dust emission and atmospheric dust fields (including dust optical thickness, visibility, and deposition rate).

Two representative dust events that originated in East Asia in the springs of 2001 and 2007 have been modeled with WRF-DuMo. Simulations with different initial size distribution of dust, injection and emission parameterizations have been performed to investigate their relative role on the modeled dust fields. In addition, we evaluated the performance of the WRF-DuMo against observations to identify the major sources of uncertainties in characterization of spatiotemporal distribution of atmospheric dust.

We performed an integrated analysis of modeled dust fields and satellite observations by introducing an ensemble model dust index, which used in conjunction with satellite dust retrievals improves the capability to characterize dust fields. Finally, we provide recommendations for the development of an integrated observational and modeling dust framework.

CHAPTER I

INTRODUCTION

Arid and semiarid regions cover about 30% of Earth's land surface (Figure 1) and are home to more than 1.2 billion people - one quarter of the human population in the year 2000. In the presence of strong winds, natural bare surfaces (deserts, dry river and lake beds) as well as anthropogenic sources (caused by human disturbances of land surfaces) can generate several billion tons of mineral dust aerosols per year [*Tegen*, 2003; *Cakmur et al.*, 2006]. Once lifted into the atmosphere, dust particles can affect the Earth's climate system via a number of complex processes: directly perturb the radiation balance by scattering and absorbing ultraviolet, visible and infrared radiation [*Sokolik and Toon*, 1996], modify properties of warm and cold clouds [*Rudich et al.*, 2002; *Yin et al.*, 2002; *DeMott et al.*, 2003; *Mahowald and Kiehl*, 2003; *Sassen et al.*, 2003; *Levin et al.*, 2005; *Nee et al.*, 2007], alter precipitation [*Rosenfeld et al.*, 2001; *Levin et al.*, 2005; *Miller et al.*, 2004b; *Yoshioka et al.*, 2007], affect the chemistry and composition of the atmosphere [*Bian and Zender*, 2003; *Tang et al.*, 2004; *Jeong and Sokolik*, 2007], affect sea surface temperature (SST), planetary boundary layer (PBL) processes and large-scale atmospheric dynamics [*Miller and Tegen*, 1998; *Miller et al.*, 2004a; *Pérez et al.*, 2006; *Evan et al.*, 2006a; *Ahn et al.*, 2007; *Zhu et al.*, 2007; *Heinold et al.*, 2008; *Foltz and McPhaden*, 2008; *Evan et al.*, 2008]. Mineral dust also influences the biogeochemical cycle by providing nutrients (iron) needed for phytoplankton growth in the oceans [*Fung et al.*, 2000; *Gao et al.*, 2003; *Mahowald et al.*, 2005; *Fan et al.*, 2006]. Dust particles deteriorate visibility and air quality, and can disrupt socioeconomic activities [*Prospero*, 1999; *Shao and Dong*, 2006; *Lu et al.*, 2007]. Furthermore, affecting the state of the atmosphere, ocean and land, dust can trigger or modulate important feedbacks within the Earth system. Because of the complex nature of

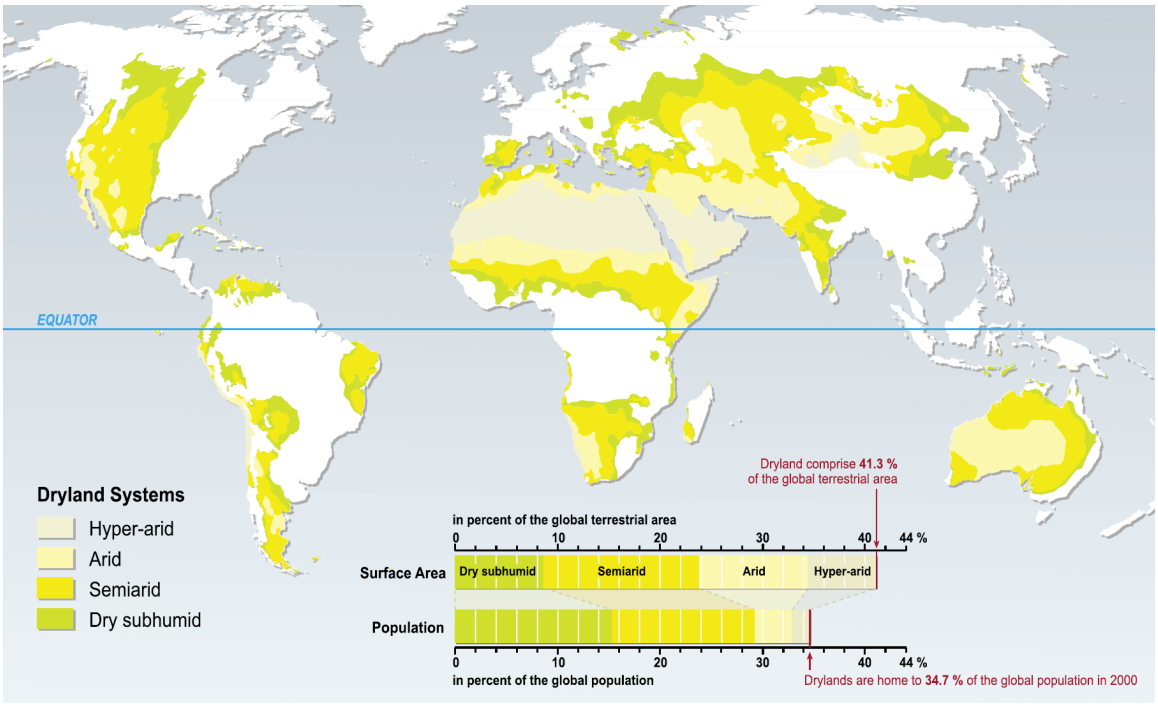

Figure 1: World's present-day drylands. (source: Millennium Ecosystem Assessment, 2005)

dust and the various ways it interacts with the different components of the Earth's climate system, assessments of the impact of dust upon the climate and environment at global and regional scales pose a complex problem.

The major factors governing the impacts of dust are the spatiotemporal distribution of dust loadings and its physicochemical properties (such as mineralogical composition and particle size spectra). The spatiotemporal distribution of dust in the atmosphere is controlled by its diverse, heterogeneous sources as well as by non-linear processes that are involved in the lifecycle of dust particles such as emission, turbulent mixing in the PBL, advection, dry and wet removal, cloud processing and heterogeneous chemistry. These and other processes, in turn, cause various changes in the physicochemical properties of dust, called dust aging. Furthermore, the properties of dust strongly vary between dust sources [*Sokolik et al.*, 1998; *Claquin et al.*, 1999; *Caquineau et al.*, 2002]. In particular, the mineralogical composition, which is a key factor governing the solar and infrared (IR)

radiative properties of dust, exhibits strong dependence on the source. The ratio of soluble to insoluble constituents is also controlled by the dust composition, hence the ability of dust particles to serve as water or ice nuclei may differ between the source regions [*Kelly et al.*, 2007; *Andreae and Rosenfeld*, 2008].

Thus, taking into account regional differences of dust aerosols will be needed to improve the prediction of the radiative forcing of dust and its effect on clouds and precipitation (direct and indirect effects). Focusing on Central and East Asian dust sources, this thesis aims to develop a coupled regional dust modeling system to provide an improved modeling capability of atmospheric dust as well as to aid in integration of ground-based and satellite observations.

Dust particles are hard to measure and difficult to represent realistically in regional and climate models because size, shape, composition and regional distribution of dust particles vary at a wide range of spatial and temporal scales. Simultaneous measurements of dust chemical, physical, optical properties, and related effects on climate are needed at the appropriate space and time scales [*Sokolik et al.*, 2001; *Kohfeld et al.*, 2005]. However, such measurements are very limited and rarely performed in a coordinated fashion. The bulk of available data originates primarily from ground-based observations (including meteorological stations and short-term field measurements), short duration field campaigns that include aircraft observations, and more recently, space-borne remote sensing instruments, although many of them were not designed to retrieve dust properties.

Basic surface measurements, such as wind speed at 10 meters, visibility and present weather category that are systematically reported by the World Meteorological Organization (WMO) stations have been widely used in dust studies. Ground-based measurements of aerosol optical properties such as spectral aerosol optical depth and column-mean particle size are reported by the global sun photometer network AERONET (Aerosol Robotic

Network). Other specialized sites include lidars, for instance the Japanese National Institute for Environmental Studies (NIES) lidar network. Lidar measurements provide information on the vertical profiles of aerosol backscatter and extinction. Significant limitations of the surface observations are the single point measurements and the intermittency of the reported data. Data coming from the surface stations are unevenly distributed and generally are not available within active dust regions. Nonetheless, visibility measurements and/or reported dust weather type have been extensively used for qualitative and quantitative characterization of dust loadings and transport routes [*Sun et al.*, 2001; *Zhang et al.*, 2003; *Darmenova et al.*, 2005]. In this thesis we examine the use of ground-based data that are available from sites located in the Central and East Asian dust source regions and downwind in the scope of the development of an integrative framework that also includes a regional model and satellite data.

Compared to ground-based measurements, satellite observations offer a more efficient way of determining key characteristics of aerosols at temporal and spatial scales that are needed to study and monitor aerosol impacts upon the climate system. Traditionally, satellite aerosol retrievals have been limited to oceans and deep-water bodies that are dark in the visible and near-IR. Over land and especially over bright surfaces such as arid regions, retrieving aerosols from satellite observations is a challenging problem because one needs to separate the signal from the surface from that of the aerosols, which requires precise characterization of the surface reflectance or emissivity. In addition, the aerosol products greatly depend on the correct discrimination between clouds and aerosols because aerosol retrievals are only possible in cloud-free conditions.

Column integrated quantities (such as aerosol optical thickness, AOT) are obtained from passive sensors that work in UV, visible and IR. Complimentary information about the vertical structure of aerosols can be obtained with active remote sensing instruments, e.g., the Cloud-Aerosol Lidar with Orthogonal Polarization (CALIOP) on board of the Cloud-Aerosol Lidar and Infrared Pathfinder Satellite Observation (CALIPSO) satellite.

Remote sensing from Sun-synchronous near-polar orbiting platforms such as the Moderate Resolution Imaging Spectroradiometer (MODIS) offer systematic global coverage; however, single location is covered by the same satellite once during daytime. Geostationary satellites (i.e., METEOSAT, FY-2C, MTSAT-1R) can cover about a third of the globe at temporal resolution of 15 minutes or higher and are well suited at monitoring of regional-scale aerosol events.

Despite its limitations over land, MODIS AOT has been used extensively during the past decade in studies of dust, especially for validation of regional and global transport models [*Colarco et al.*, 2003; *Tanré et al.*, 2003]. The "Deep Blue" aerosol retrieval algorithm [*Hsu et al.*, 2004, 2006] has been recently developed to enhance the MODIS retrievals over land. The Multi-angle Imaging Spectro-Radiometer (MISR) provides measurements of aerosol properties based on its sensitivity to the shape of aerosol scattering phase functions [*Kalashnikova et al.*, 2005]. MISR AOT has been used to trace the transport of dust plumes [*Di Girolamo et al.*, 2004; *Kalashnikova and Kahn*, 2006], to constrain dust modeling [*Stier et al.*, 2005] and to validate AOT retrieved from other instruments.

The Total Ozone Monitoring Satellite (TOMS) aerosol index (AI) provides semi-quantitative information regarding the presence of UV absorbing aerosols such as dust and smoke. Despite its qualitative nature, TOMS AI has been one of the most extensively used products for characterization of dust spatial fields [*Husar et al.*, 2001; *Prospero et al.*, 2002; *Gong et al.*, 2003], mainly because of its robustness over both land and ocean. Another dust index, the infrared difference dust index (IDDI), was specifically developed for remote sensing of dust in arid regions by *Legrand et al.* [2001]. The IDDI is based on the fact that dust affects the daytime thermal infrared radiance observed from space. In the presence of dust the outgoing thermal radiation is attenuated, resulting in a reduction in the outgoing longwave radiation at the top of the atmosphere when compared to clear conditions [*Ackerman*, 1997; *Legrand et al.*, 2001]. In addition, dust scatters the shortwave radiation and decreases the solar flux that reaches the surface [*Legrand et al.*, 2001; *Christopher et al.*,

2006; *Tanré et al.*, 2003], therefore decreasing the surface temperature compared to clear conditions. Both effects lead to a reduction of the thermal infrared radiation that reaches the top of the atmosphere, therefore increasing the thermal contrast between clear and dust-laden atmosphere. IDDI was used for validation of dust models [*Marticorena et al.*, 1997] and for real time forecasting of Asian dust storms [*Hu et al.*, 2008].

Recently, *Evan et al.* [2006b,c] developed an over-water dust detection algorithm that utilized the 5-channel Advanced Very High Resolution Radiometer (AVHRR) imager. The algorithm was designed to discriminate dust from clouds, including very optically thick dust plumes ($0.6 < AOT < 4.5$). It is based on the spatial and thermal uniformity differences between aerosols and clouds, and the depression of the brightness temperature (BT) difference between BT($11\,\mu m$) and BT($12\,\mu m$) exhibited by dust plumes. The algorithm can flag a pixel as being dusty or not, thus avoiding contamination of dusty data from smoke and other detected aerosols. The resulting dust product has been validated against AERONET measurements and showed a good operational accuracy. However, *Evan et al.* also showed few cases for which the AVHRR dust algorithm failed to detect pixels containing dust and misclassified cloudy pixels as dusty. Furthermore, neither the AVHRR dust index nor the IDDI take into account the regional specifics of dust properties.

Accurate discrimination of dust from clouds and other aerosols is a key step required in remote sensing of atmospheric dust. The approaches suggested by past studies include the splitwindow technique, the tripectral technique and the spatial variability technique. The splitwindow and tripectral approaches employ brightness temperatures calculated from satellite radiance measurements in the $8–12\,\mu m$ atmospheric window region. Either two or three channels can be used to calculate the bispectral or trispectral BT differences [*Ackerman*, 1997; *Dunion and Velden*, 2004; *Evan et al.*, 2006c]. These techniques rely on a fixed BT difference threshold to detect mineral dust. The prescribed threshold is usually selected after the examination of a representative sample of dust and cloud data. The result is a universal threshold value that is used to detect dust over diverse geographical regions.

Considering several representative mineral mixtures, a modeling study by *Sokolik* [2002] showed that differences in composition, especially differences in the amount of clays and quartz, have a large impact on spectral brightness temperatures. Using MODIS observations in the IR, in this thesis we examine the regional radiative signature of atmospheric dust and implications to IR remote sensing and dust detection.

In solar remote sensing, discrimination between clouds and aerosols is commonly performed using the spatial variability approach. This approach is based on the fact that clouds are more inhomogeneous on scales of a few kilometers compared to aerosols [*Martins et al.*, 2002]. The spatial inhomogeneity is commonly expressed in terms of the standard deviation of the reflectances of a group of pixels (e.g., 3×3 pixels). A fixed threshold value is applied to screen clouds from aerosols [*Martins et al.*, 2002]. Operational aerosol retrievals (e.g., MODIS and AVHRR) rely on the same fixed standard deviation threshold regardless of the type of aerosols, which could lead to misclassification of dust as clouds because of the high reflectance of dust plumes. Another inherent problem with the fixed standard deviation threshold approach is the inability to classify mixed dust and cloud pixels. Given that dust is often observed in the presence of clouds, due to the natural association of dust outbreaks with mid-latitude cyclones, and the large interest in the community to study dust-cloud interactions with satellite data, an accurate discrimination between dust, clouds and mixed dust-cloud pixels is of great interest. To this end, we perform a statistical analysis of multi-year MODIS observations to develop an improved technique for dust detection and to examine the capability of detection of mixed dust-cloud scenes with passive remote sensing. MODIS along with several other satellite sensors are also used for validation of the regional model developed under this thesis within the integrated observational and modeling framework.

A number of global and regional dust modeling systems have been developed during the last decades. General Circulation Models (GCMs) have proven to reproduce reasonably well the large-scale regional and seasonal dust features [*Tegen*, 2003; *Zender et al.*, 2003;

Cakmur et al., 2004]. However, not all dust sources can be accurately resolved because of the GCM coarse spatial resolution (1.5°– 5°). Furthermore, global models utilize simplified parameterizations of land-surface processes, boundary-layer physics, microphysical processes, cloud physics and precipitation that are all important for dust modeling. In contrast to global models, regional models provide advantageous capabilities in resolving surface properties, transport and removal processes on smaller than the synoptic scale, which is critical for an accurate prediction of the dust lifecycle [*Heinold et al.*, 2007]. Moreover, regional models are better suited for comparison and integration with ground-based and satellite observations of individual dust events.

The existing dust models employ different parameterizations of dust emission. Some use the so-called "simple" dust emission schemes, in which the emitted dust mass is proportional to the third or fourth power of the wind speed [*Uno et al.*, 2001; *Liu et al.*, 2003], while others [*Gong et al.*, 2003; *Laurent et al.*, 2006] use more complex physically based parameterizations, accounting explicitly for land surface properties. *Uno et al.* [2006] performed an intercomparison study between several dust modeling systems and found significant discrepancies between the modeled dust fields. These differences were mainly attributed to the differences in the modeled dust emission fluxes.

Despite the existence of complex dust emission schemes which take into account land surface properties, their incorporation in numerical models has been proven difficult. One problem arises from the incompatibility of the aeolian scales (millimeters to centimeters) on which the dust emission schemes operate and the regional and global scales (tens to hundreds of kilometers) that are representative of atmospheric transport models. Another problem comes from the lack of the required input parameters (such as undisturbed soil grain size distribution, top-layer soil moisture and surface roughness) on aeolian scales. Soil moisture is a critical variable because it affects the threshold wind speed so that increasing soil moisture suppresses the dust emission. Friction velocity is another parameter that is commonly predicted by regional models by using a fixed aerodynamic roughness.

The latter might be several orders of magnitude larger than the aeolian roughness required in dust emission schemes. Since dust emission strongly depends on wind forcing, accurate modeling of the friction velocity is of utmost importance.

Once dust particles are released into the atmosphere they are subjected to the following processes: advection, turbulent mixing, gravitational sedimentation, deposition onto the surface and wet removal by in- and below-cloud scavenging. The distribution of dust aerosols in the atmosphere is modeled numerically by integrating the mass conservation equation for the dust concentration $c(x, y, z, t)$

$$\frac{\partial c}{\partial t} = -\frac{\partial uc}{\partial x} - \frac{\partial vc}{\partial y} - \frac{\partial (w - v_s)c}{\partial z} + D_x + D_y + D_z + \left(\frac{\partial c}{\partial t}\right)_{src} - \left(\frac{\partial c}{\partial t}\right)_{snk} \quad (1)$$

Here u, v, w are the components of the wind vector in x, y and z directions; v_s is gravitational settling velocity; D_x, D_y and D_z are turbulent mixing terms in x, y and z; $(\partial c/\partial t)_{src}$ is the dust source term; $(\partial c/\partial t)_{snk}$ is the dust sink term which includes dry and wet deposition.

The source term $(\partial c/\partial t)_{src}$ describes the rate of change of the freshly mobilized dust particles concentration. It is, therefore, controlled by the dust emission and the immediate injection (initial mixing) of the fresh dust particles in the atmosphere. As pointed out by *Uno et al.* [2003, 2004], the initial dust uplift height is highly uncertain. To the best of our knowledge, only a few studies consider explicitly the dust injection mechanisms and their implementation in regional models. In the regional model DREAM [*Nickovic et al.*, 2001], the initial concentration is calculated in the first (surface) model layer. In the CFORS regional model [*Uno et al.*, 2003, 2004], the initial dust uplift height is determined by the model predicted vertical profile of the potential temperature, while the mass mixing ratio of the freshly emitted dust is distributed uniformly within the mixing height. In their modeling study *Park et al.* [2007] used AURAMS CTM model to investigate the impact of the method used to inject the emitted dust particles. They considered the following scenarios - the emitted dust particles were injected only into the bottom layer (1-layer injection), whose top is at 10 m; and into the lowest three model layers (3-layer injection), whose top is at 90 m.

Dust particles exhibit different shapes and a wide range of sizes - from sub-micron to tens of micrometers. Hence Equation 1 also needs to take into account that atmospheric dust is polydisperse. There is a distinct difference between the processes that control the size distribution of the fresh and aged dust in the atmosphere. In particular, the size distribution of freshly emitted dust particles depends on the wind speed, surface conditions and soil characteristics which govern the mobilization of soil grains, while during the transport in the atmosphere the particle size distribution is continuously modified by size dependent removal processes. Thus, the dust particle size distribution should be represented realistically in three-dimensional transport models to accurately model the transport of dust and its radiative and biogeochemical impacts [*Foret et al.*, 2006].

One can expect that the initial dust size distribution and injection height can significantly affect the atmospheric dust loading because they control the source term in the mass conservation equation. The lack of multiple physical parameterizations of dust emission, injection and initial size of freshly emitted dust within the same modeling framework makes it difficult to pinpoint the factors that matter the most in the observed discrepancies between the existing dust models. The development of a coupled dust modeling system that includes multiple physical parameterizations of dust processes can address this problem and can help to constrain the sensitivity of the modeled dust fields to the uncertainties in the dust microphysical properties and critical physical processes such as dust emission and removal. Development of such regional modeling system is a key goal of this thesis.

A number of dust modeling studies [*Nickovic et al.*, 2001; *Lu and Shao*, 2001; *Shao et al.*, 2002; *Shao and Dong*, 2006; *Sun et al.*, 2006] introduced "integrated" dust modeling systems where the term "integrated" stands for a combination of a terrestrial processor that provides information about land surface properties, a dust emission module, and a transport driver. Also, recent efforts have been made to develop integrated dust modeling systems based on the assimilation of surface or/and satellite data. For instance, *Cakmur*

et al. [2006] used AOTs from AERONET, AVHRR and TOMS, surface concentrations, deposition and size distribution data to constrain the magnitude of the global dust cycle by minimizing the difference between the modeled (GISS AGCM) dust distribution and observations. *Yumimoto et al.* [2007] and *Uno et al.* [2008] went a step further and developed the four-dimensional variational (4DVAR) data assimilation system RAMS/CFORS-4DVAR (RC4). They optimized the model dust emission by assimilating data from the NIES LIDAR network. *Gong and Zhang* [2008] described an integrated system for observation and modeling targeted for operational dust forecasting, which is based on 3DVAR data assimilation and uses PM_{10} concentrations, visibility and dust loading retrievals from the geostationary satellite FY-C2.

Given the very initial stage in the development of such integrated dust systems, the goal of this thesis is to develop new modeling tools and recommendations for an integrated observational and modeling framework consisting of a new regional dust modeling system for Central and East Asia, and ground-based and satellite observations. The specific objectives are as follows:

1. Develop a coupled regional dust modeling system (WRF-DuMo) by incorporating a dust emission module (DuMo) into the community NCAR Weather Research Forecast (WRF) model that is capable to simulate size resolved dust concentrations, explicitly treat land surface properties in dust emission, have multiple options for dust injection in the atmosphere and offer flexible parameters of the initial size distribution of emitted dust. Such capabilities will allow for the first time to bracket within a single modeling system the uncertainties associated with modeling the dust emission and atmospheric dust fields (including dust optical thickness, visibility, and deposition rate).

2. Examine the capabilities of ground-based and satellite observations to characterize mineral aerosols in Asian dust source regions and downwind. Investigate the regional signature of dust from remote sensing data. Test and improve the approaches

for dust detection and discrimination from clouds. Explore the possibility for the development of a new probabilistic dust detection technique, including characterization of dust-cloud mixed scenes.

3. Evaluate the performance of WRF-DuMo against observations to identify and quantify the major sources of uncertainties in characterization of spatiotemporal distribution of atmospheric dust. Provide recommendations for the development of an integrated observational and modeling dust framework.

This thesis is organized as follows. Chapter 2 describes the development and capabilities of the new regional modeling system WRF-DuMo. Using WRF-DuMo, we examine the role of the initial dust size distribution and injection height in affecting dust particle sizes, aerosol optical thickness, visibility, deposition rate and dust vertical structure during dust episodes. Our approach was to simulate a historical dust event to ensure that realistic meteorological fields were used in the sensitivity analysis and to vary the initial size distribution and injection height independently from the dust emission scheme. In particular, we simulated the "Perfect Dust Storm" event that occurred in Spring of 2001 and analyzed a 27-member ensemble of WRF-DuMo runs driven by NCEP reanalysis data (Figure 2).

In Chapter 3 we examine the capability of ground-based and satellite observations to characterize atmospheric dust, and investigate regional differences in dust properties. We also perform a statistical analysis of satellite visible reflectances and investigate the possibility to discriminate mixed dust and cloud pixels from dust pixels and cloud pixels. Based on the results from the statistical analysis of the spatial variability of visible reflectances we calculated the probability for a pixel to be dusty, cloudy or mixed dust and cloud. Our findings can aid the development of a probabilistic dust-cloud mask that takes into account the specifics of mineral dust aerosols and can help improve the overall quality of satellite remote sensing of dust. In addition, dust presence probability derived independently from observations and modelling can be used as a common metrics in an integrated modeling and observational system to better characterize dust fields and their uncertainties.

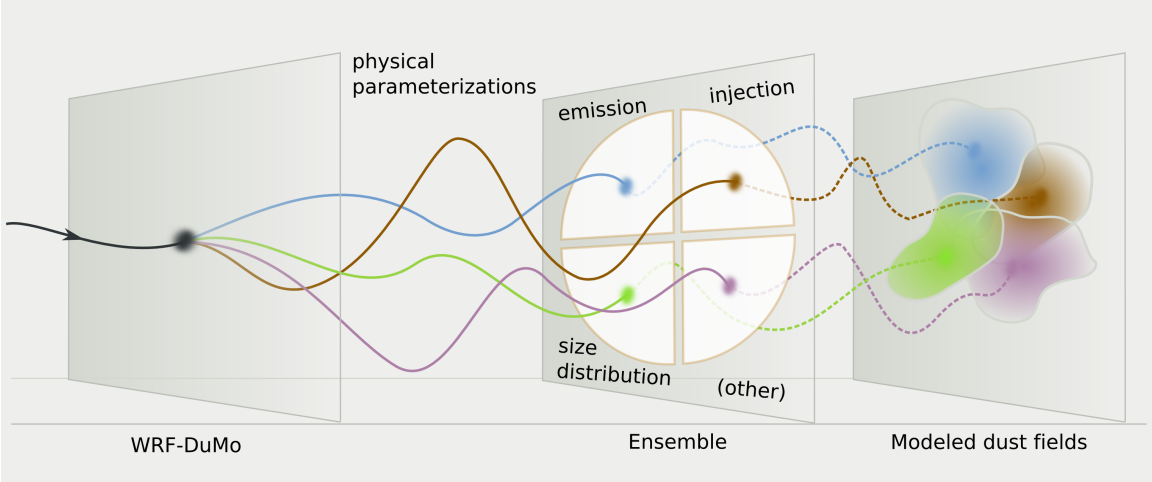

Figure 2: The unique capabilities of WRF-DuMo allow to simulate dust events and to bracket the uncertainties in the modeled dust fields by means of an ensemble of WRF-DuMo model runs with different physical parameterizations of dust emission, initial injection height and fresh particle size distribution.

In Chapter 4 we investigate the sensitivity of modeled dust fields to dust emission schemes. We also perform an integrated analysis of dust fields inferred from satellite observations and an ensemble of WRF-DuMo runs (Figure 2) with two physically-based dust emission schemes and a simple dust emission scheme. A representative event that occurred in Spring of 2007 was simulated and satellite data was used to tune the model soil moisture. Modeled dust optical thickness is compared against observations to identify the model biases, thus providing guidance for future improvements in WRF-DuMo. We performed integrated analysis of modeled dust fields and satellite observations by introducing model dust index, which helps to resolve some inherent problems of individual data sets and the model itself. The "integrated dust index" methodology is demonstrated by merging TOMS AI and modeled dust index as an example of an integrated dust product.

The main findings of the thesis are summarized in Chapter 5.

CHAPTER II

DEVELOPMENT OF A COUPLED REGIONAL DUST MODELING SYSTEM WRF-DUMO

2.1 Introduction

This Chapter describes the development of a new coupled regional dust modeling system WRF-DuMo. The Dust Module (DuMo) is implemented as a component of the Weather Research and Forecasting (WRF) model and modified version of the chemistry module CHEM. We will focus our discussion on the following WRF-DuMo modules: dust emission, dust injection, dust optics, and dust transport-deposition.

In Section 2.2, the important mechanisms of dust emission, transport and deposition, and their representation in models are discussed by examining previous studies. This section also addresses the deficiencies of existing dust models and motivates the need for improvements. Section 2.3 describes the physics of key components of the WRF-DuMo modeling system, including emission, injection, dry removal and optics. In Section 2.4 we investigate the effect of the initial size distribution and injection on the modeled dust particle sizes, concentration, visibility, optical thickness and vertical structure. Section 2.5 summarizes our main findings.

2.2 Deficiencies and needs in representation of dust processes in regional and global transport models

Modeling of dust distribution in the atmosphere requires adequate representation of dust sources, sinks and transport processes. The prognostic equation[a] of the dust aerosol distribution is:

[a]Similar equation can be written in terms of the aerosol mass concentration (i.e. Equation 1) or in terms of the aerosol mass/number mixing ratio.

$$\frac{\partial n(r_p)}{\partial t} = f[n(r_p)] \tag{2}$$

where r_p is the aerosol radius, $n(r_p)$ is the aerosol paricle number size distribution and $f[n(r_p)]$ is a complex function that describes the evolution of the aerosol distribution, i.e., changes due to emission, advection, interaction with other aerosols or clouds, etc. Ideally, all dust related processes have to be implemented in a numerical model (e.g., through parameterizations of different levels of complexity). In practice, however, no single dust model accounts for all processes and the majority of models rely on a rather simplified treatment of dust sources and sinks. An example of such simplification is given with Equation 3 where the rate of change of the aerosol size distribution is divided for transport, sources, dry removal (deposition and sedimentation) and wet removal (in- and bellow-cloud scavenging):

$$\frac{\partial n(r_p)}{\partial t} = \frac{\partial n}{\partial t}\Big|_{transport} + \frac{\partial n}{\partial t}\Big|_{sources} + \frac{\partial n}{\partial t}\Big|_{dry} + \frac{\partial n}{\partial t}\Big|_{wet} \tag{3}$$

A number of global [*Tegen*, 2003; *Zender et al.*, 2003; *Cakmur et al.*, 2004] and regional dust models have been developed over the last decade. Examples of regional dust models are as follows: Dust Regional Atmospheric Model (DREAM) [*Nickovic et al.*, 2001], ChimereDust [*Menut et al.*, 2007], COAMPS [*Liu et al.*, 2003], CARMA-MM5 [*Barnum et al.*, 2004], NARCM [*Gong et al.*, 2003], WEMS [*Shao*, 2001], RegCM [*Zakey et al.*, 2006], MesoNH [*Grini et al.*, 2006] and LM-Muscat [*Heinold et al.*, 2007]. In comparison to global dust models, regional modeling is better suited for resolving surface properties, emission and transport processes, which are essential for a precise dust cycle prediction [*Heinold et al.*, 2007].

A critical component of the accurate prediction of dust loadings and spatiotemporal patterns is the simulation of realistic size resolved vertical dust fluxes. However, parameterization of dust emission has been the source of significant uncertainties in the dust models [*Tegen*, 2003; *Uno et al.*, 2006]. Dust emission schemes range from simple type schemes, in which the dust vertical flux depends on a prescribed erodible fraction and fixed

threshold friction velocity (or threshold surface wind), to advanced schemes, in which a threshold value of friction velocity is predicted as a function of surface soil characteristics [*Marticorena and Bergametti*, 1995; *Lu and Shao*, 2001]. The choice of a particular dust emission scheme will result in a range of uncertainties in the predicted dust mass. For instance, *Zhao et al.* [2006] showed significant differences in the model predicted fluxes with two different dust emission parameterizations based on the work of *Shao* [2004] and *Alfaro and Gomes* [2001].

Being a complex physical process, dust emission is parameterized by using separate models for threshold friction velocity, saltation fluxes and vertical dust fluxes. To further complicate the issue, the existing parameterizations of the same quantity (for instance threshold friction velocity) require different input parameters. Ideally, different parameterizations should provide very similar values of the modeled quantity. In practice, however, the values can be quite different due to lack of direct relationship between the different external parameters feeding the parameterizations. Furthermore, the existing dust emission parameterizations are validated for different dust source regions - for example, Shao parameterization is derived for Australian soils, while Alfaro and Gomes parameterization is fitted for Saharan soils. Thus, dust emission parameterizations can be biased when their use is extended for other deserts. None of the existing dust modeling studies discussed the issues outlined above or compared the sources of discrepancies between the existing physically based dust emission parameterizations. The majority of the existing regional dust models have incorporated a single dust emission scheme. Implementing multiple dust emission schemes within a single modeling system will make it possible to investigate the sensitivity of the modeled dust fields to dust emission schemes in a consistent manner, and most importantly, to bracket uncertainties in the modeled dust fluxes.

Observational evidence suggests that dust plumes can reach a multitude of heights, ranging from the PBL surface layer up to the tropopause [*Husar et al.*, 2001; *Uno et al.*, 2001]. This indicates that there are efficient mechanisms for vertical mixing of the freshly

emitted dust particles. In dust models, linking the emission from the surface with the rate of change of concentration due to mobilization of dust particles in the atmosphere requires the introduction of a characteristic height - uplift or injection height. Several studies (e.g., *Uno et al.* [2003, 2004]) pointed out that the initial dust uplift height is highly uncertain. To the best of our knowledge, only a few studies address the dust injection mechanisms and their implementation in the models. One of them is a study by *Nickovic et al.* [2001]. In their model, the emitted dust is distributed in the first model layer. In CFORS model [*Uno et al.*, 2003, 2004] the initial dust uplift height is determined by the vertical profile of the potential temperature. The uplifted dust mass mixing ratio is distributed uniformly within the mixing height. In their modeling study *Park et al.* [2007] used AURAMS CTM model to investigate the impact of the method used to inject the emitted dust particles. They considered the following scenarios - the emitted dust particles were injected only into the bottom layer (1-layer injection), whose top is at 10 m; and into the lowest three model layers (3-layer injection), whose top is at 90 m. One can expect that the initial dust injection can affect the atmospheric dust fields significantly. The importance of this issue motivated us to implement three different injection schemes in WRF-DuMo (see Section 2.3.2.2). This new modeling capability enables us to perform an in-depth investigation of the role of the initial injection height on the modeled spatiotemporal distribution of dust (see Section 2.4).

Measurements show that dust particles have a wide range of sizes spanning from sub-micrometers to tens of micrometers. Given that dust emission and removal processes are size dependent, it is important to represent and model accurately the size distribution of dust. Two common methods exist for representation of particle size distributions: modal and sectional (bin) representation (Figure 3). In the sectional approach, the aerosol size distribution is represented by a set of contiguous, non-overlapping, discrete size bins. The majority of the existing regional dust models employ the sectional approach due to its flexibility in treating aerosol microphysical processes such as coagulation, condensation and

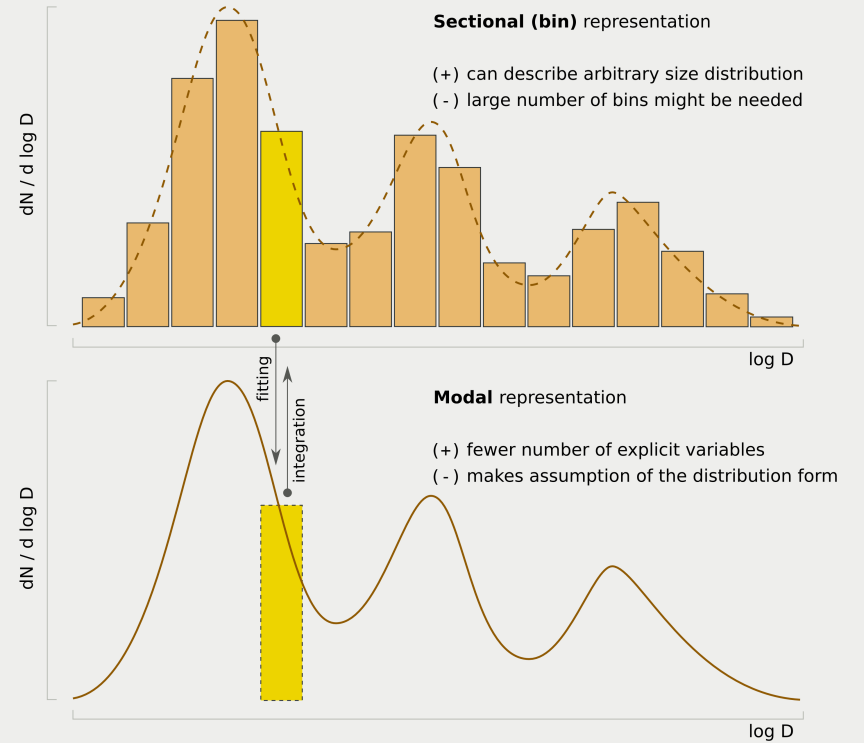

Figure 3: Sectional and modal representation of particle size distributions.

chemical processes (Table 1). In the modal approach, each distinct aerosol subpopulation is represented by an analytical modal distribution function (e.g., [*Binkowski and Shankar*, 1995]). The WRF model, for example, employs a three-modal lognormal distribution to describe aerosol particles.

One of the outstanding issues related to modeling of dust particle size distribution are the uncertainties in the measured size distribution of freshly emitted dust particles. Very limited information on initial dust size distributions exists in the literature [*d'Almeida*, 1987; *Alfaro et al.*, 1998; *Zhang et al.*, 2003].

d'Almeida [1987] measured dust particle number distributions in Niger, Sahara Desert for background clean conditions, wind carrying dust (visibility less than 8 km) and sand-storms (visibility less than 2 km). Dust aerosol particles were collected with a modified Winkler compactor able to collect particles smaller than 5 μm. The measured distributions were then fitted to trimodal lognormal functions (Table 2). The 'Background' modes of

Table 1: Representation of particle size distribution and removal processes in existing global and regional models.

Model	Model type	Size distribution	Dry deposition	Wet removal
CARMA-MM5	Regional	10 bins	2 layer method	N/A (precipitation suppresses dust emission)
NARCM (CAM)	Regional	(12+) bins	ADOM scheme	In-cloud and below cloud scavenging
MesoNH	Regional	3-modal	Resistance concept	Washout
LM-MUSCAT	Regional	5 bins	Resistance concept	N/A
RegCM	Regional	4 bins	Turbulent transfer and gravitational settling	In-cloud and below cloud scavenging
WRF-CHEM	Regional	3-modal	Resistance concept	N/A for dust
MASINGAR	Global	10 bins	Resistance concept	In-cloud and below cloud scavenging
DEAD	Global	hybrid (bins and modal sub-bin)	Resistance concept	In-cloud and below cloud scavenging

dust suggested by *d'Almeida* were used in the DEAD model [*Zender et al.*, 2003] as a representative source modes.

To obtain size distributions of mineral aerosols released by wind erosion, *Alfaro et al.* [1998] used two soil samples of loamy soils from Spain and sandy soils from Niger. The dry distributions of the erodible fractions of the soils were determined by dry sieving and fit to lognormaly distributed populations. *Alfaro et al.* found that for both samples the soil aggregate size distributions were dominated by a single population with a mean diameter between 200 and 300 μm. Then for each soil and at four different wind speeds in the LISA wind tunnel, the dust size distributions were determined in the 1–160 μm size range with a laser particle sizer. Because *Alfaro et al.* were interested in particles with sizes that cause significant optical effects, they considered only aerosol particles with diameter less than 20 μm. A major finding of their study was that regardless of the wind speed the aerosols produced by the two different soils have very similar lognormal distributions and only the proportions in which they appear in the aerosol seem to depend on the friction velocity. The dust aerosol lognormal distributions are given in Table 3. These size distributions were incorporated into the dust emission scheme developed by *Marticorena and Bergametti* [1995].

Zhang et al. [2003] performed measurements of the size distribution of dust aerosols in Chinese source regions during 1994–2001 within and on the edge of several deserts (Mu Us, Kumutage, Ulan Buh, Taklamakan). The impactor for measuring the dust-size distribution only gave fractions for particles smaller than 0.25 μm and larger than 16 μm due to the size cutoff. Between 0.25 and 16 μm, observations were approximated by a lognormal fit. Measured size distributions are presented in Table 4. They were used in the regional model developed by *Gong et al.* [2003].

Predicting the distribution of mineral dust in the atmosphere requires not only realistic representation of the sources and transport processes, but also dust sinks. Sink processes are dry deposition, and wet removal (in-cloud and below-cloud scavenging). The majority

Table 2: Parameters of lognormal distributions for desert aerosol. After *d'Almeida* [1987].

	r_1, μm	r_2, μm	r_3, μm	σ_1	σ_2	σ_3	N_1, cm^{-3}	N_2, cm^{-3}	N_1, cm^{-3}
Background	0.08	0.7	5	2.10	1.90	1.6	301±22	21.99±6	1×10^{-3}
Wind carrying dust	0.052	1.5	12	2.15	2.07	1.7	1710±102	22.7 ±5	5×10^{-3}
Sandstorm	0.05	1.5	16	2.15	2.50	1.8	2502±126	29.2 ±7	1.2

Table 3: Geometric mean mass diameters (d) and geometric standard deviations (σ) for the three aerosol particle populations that can be released from arid soils. After *Alfaro et al.* [1998].

	Mode 1	Mode 2	Mode 3
$d(\mu m)$	1.5	6.7	14.2
σ	1.7	1.6	1.5

Table 4: Average size distributions for ground-based mineral aerosol during local dust-storm events at five desert sites in Spring of 1994 and 2001. After *Zhang et al.* [2003] and *Gong et al.* [2003].

	Size distribution (d, μm)				
	0.25 to 16 (Lognormal distribution)				
	$<0.25\%$	MMD	σ	%	$>16\%$
Mu Us Desert	0.52	3.7	1.5	72	28
Kumutage Desert	0.37	5.2	1.5	74	26
Taklimakan and Ulan Buh Desert	4.7	7.3	1.6	69	25
Average of Chinese deserts	1.7	4.5	1.5	69	30

of regional models (see Table 1), including WRF-CHEM and WRF-DuMo employ the resistance concept for parameterization of the dry deposition [*Wesley*, 1989].

The in-cloud scavenging rate of dust aerosol is commonly calculated using the first-order loss rate (i.e., the scavenging rate is directly proportional to the dust mixing ratio) (see Table 5). Below-cloud scavenging is considered to be proportional to the precipitation rate and the dust mixing ratio. Currently WRF-DuMo does not account for dust wash-out, however, a new parameterization for dust cloud interaction is under development [*Kumar et al.*, 2008] and will be soon incorporated in the model. Dust removal processes are extremely sensitive to the size concentration of the dust particles. In addition, correct modeling of wet removal requires knowledge of soluble component at the surface of the dust particles and correct modeling of cloud properties (e.g., size distribution, phase, vertical extend of the cloud, precipitation rate).

The different spatiotemporal resolution, parameterizations of model physics and dust processes used by different dust models makes intercomparison between modeled dust fields and emission a challenging task. To better quantify the diverse effects of dust on climate, it is necessary to bracket the uncertainties in modeled dust fields due to differences and limitations in the existing physical parameterizations of dust processes. This motivated us to develop a new state-of-the-art regional dust model that offers several dust emission schemes with different complexity, flexible run-time options for dust injection, initial size distributions and terrestrial preprocessor providing different set of land surface parameters. The following sections present the development and testing of the coupled regional dust modeling system WRF-DuMo, with emphasis on the effect of the initial dust size distributions and injection heights on the modeled 3D dust fields.

2.3 Development of WRF-DuMo

2.3.1 Description of WRF and chemical module CHEM

The Weather Research and Forecasting (WRF) model is a next-generation mesoscale numerical weather prediction system. WRF is designed to be a flexible, state-of-the-art, portable code that is efficient in a massively parallel computing environment. It offers numerous physics options, thus addressing the specific needs and experience of the broad modeling community. The WRF model is suitable for use in a broad spectrum of applications across scales ranging from meters to thousands of kilometers. Such applications include research and operational numerical weather prediction (NWP), data assimilation and parameterized-physics research, downscaling climate simulations, driving air quality models, atmosphere-ocean coupling, and idealized simulations (e.g., boundary-layer eddies, convection, baroclinic waves). The principal components of the WRF system are depicted in Figure 4. The WRF Software Framework (WSF) provides the infrastructure that accommodates multiple dynamics solvers, physics packages that plug into the solvers through a standard physics interface, programs for initialization, and the WRF variational data assimilation (WRF-Var) system. Two dynamics solvers exist in the WSF: the Advanced Research WRF (ARW) solver (originally referred to as the Eulerian mass or "em" solver) developed primarily at NCAR, and the NMM (Nonhydrostatic Mesoscale Model) solver developed at NCEP.

In this thesis the advanced research ARW WRF model (version 2.2.1) is being used. The ARW dynamics solver integrates the compressible, nonhydrostatic Euler equations. The equations are cast in flux form using variables that have conservation properties, following the framework of *Ooyama* [1990]. The ARW may be run with initial conditions that are defined analytically for idealized simulations, or it may be run using interpolated data from either a large-scale analysis or forecast for real-data cases. Output from the ARW system initial condition programs is suitable as input to the WRF variational assimilation package WRF-Var. The ARW supports horizontal nesting that allows resolution to

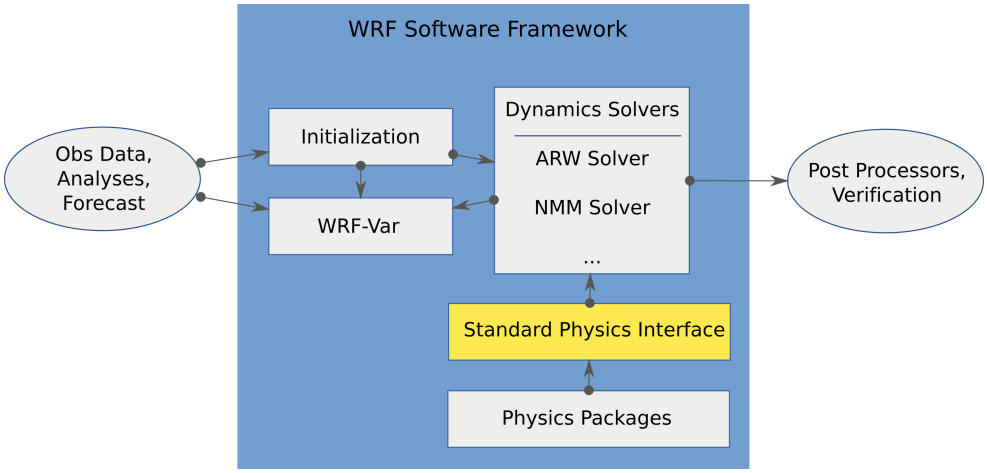

Figure 4: WRF system components. (Adopted from NCAR/TN-468+STR)

be focused over a region of interest by introducing additional grids into the simulation.

The WRF physics options fall into several categories, each containing several options. The physics categories are (1) microphysics, (2) cumulus parameterization, (3) planetary boundary layer (PBL), (4) land-surface model, (5) radiation and (6) diffusion. The physics section is separated from the rest of the dynamics solver by the use of physics drivers. For detailed explanation of each parameterization in WRF see the ARW user guide at `http://www.mmm.ucar.edu/wrf/users/docs/user_guide/contents.html`.

WRF-CHEM is a fully coupled online Weather Research and Forecasting/Chemistry (WRF plus chemistry module) model [*Grell et al.*, 2005]. The air quality component CHEM of the model is fully consistent with the meteorological component; both components use the same transport scheme (mass and scalar preserving), the same grid (horizontal and vertical components), and the same physics schemes for subgrid-scale transport. The components also use the same time step, hence no temporal interpolation is needed. The chemistry package consists of dry deposition ("flux-resistance" method), biogenic emission as in *Simpson et al.* [1995] and *Guenther et al.* [1994], the chemical mechanism from RADM2, a complex photolysis scheme (Madronich scheme coupled with hydrometeors), and a state of the art aerosol module (MADE/SORGAM aerosol parameterization).

All transport of chemical species is done online. For the chemical mechanism used in the model, 39 chemical species are fully prognostic. For the aerosol module, another 34 variables are added, including the total number of aerosol particles within each mode, as well as all primary and secondary species (organic and inorganic) for both Aitken and accumulation mode, and three species for the coarse mode (anthropogenic, marine, and soil-derived aerosols).

The flux of trace gases and particles from the atmosphere to the surface is calculated by multiplying concentrations in the lowest model layer by the spatially and temporally varying deposition velocity, which is proportional to the sum of three characteristic resistances (aerodynamic resistance, sublayer resistance, surface resistance). The surface resistance parameterization developed by *Wesley* [1989] is used. In this parameterization, the surface resistance is derived from the resistances of the surfaces of the soil and the plants. The properties of the plants are determined using land-use data and the season. The surface resistance also depends on the diffusion coefficient, the reactivity, and water solubility of the reactive trace gas. When employing the aerosol parameterization, the deposition velocity, v_{dk}, for the k^{th} moment of a polydisperse aerosol is given by:

$$v_{dk} = (r_a + r_{dk} + r_a r_{dk} v_{Gk})^{-1} + v_{Gk} \,, \tag{4}$$

where r_a is the surface resistance, v_{Gk} is the polydisperse settling velocity, and r_{dk} is the Brownian diffusivity [*Slinn and Slinn*, 1980; *Pleim et al.*, 1984].

The aerosol module is based on the Modal Aerosol Dynamics Model for Europe MADE [*Ackermann et al.*, 1998]. The size distribution of the submicrometer aerosol is represented by two overlapping intervals, called modes, assuming a log-normal distribution within each mode:

$$n(lnd_p) = \frac{N}{\sqrt{2\pi} ln\sigma_g} exp\left[-\frac{1}{2}\frac{(lnd_p - lnd_{pg})^2}{ln^2\sigma_g}\right] , \tag{5}$$

where N is the number concentration, d_p is the particle diameter, d_{pg} is the median diameter, and σ_g is the standard deviation of the distribution. The k^{th} moment of the distribution is

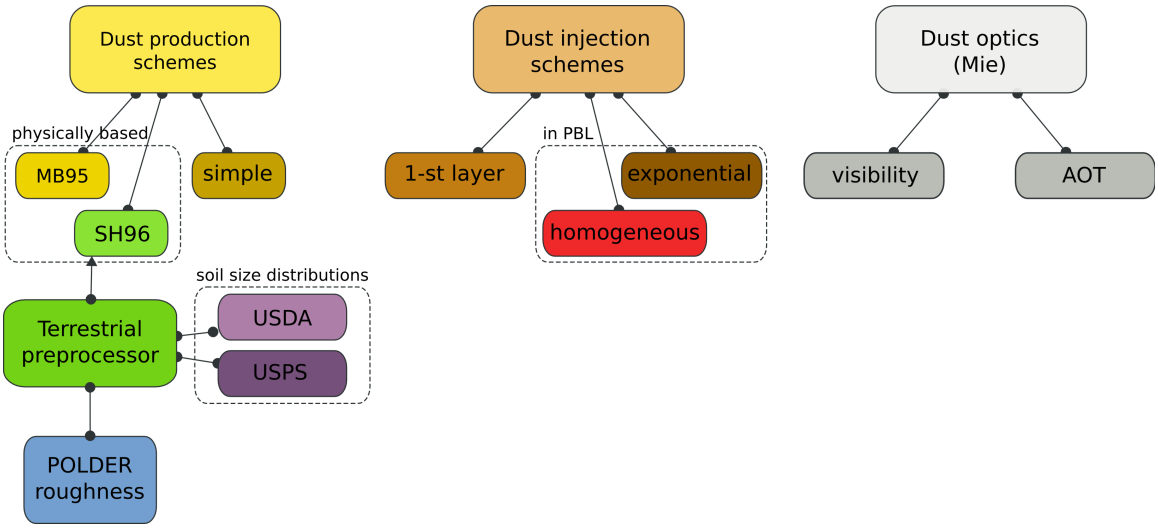

Figure 5: Dust module DuMo components.

defined as:

$$M_k = \int_{-\infty}^{+\infty} d_p^k n(lnd_p) d(lnd_p) \tag{6}$$

with the solution:

$$M_k = N d_{pg}^k exp\left[\frac{k^2}{2} ln^2 \sigma_g\right] \tag{7}$$

The zeroth-moment M_0 is the total number of aerosol particles within the mode suspended in a unit volume of air, the second moment M_2 is proportional to the total particulate surface area within the mode suspended in a unit volume of air, and the third moment M_3 is proportional to the total particulate volume within the mode suspended in a unit volume of air.

2.3.2 Development of the dust module DuMo

The dust module DuMo was specifically designed to provide advanced representation of key dust processes in a regional model. DuMo can be used off-line or can be coupled online with a transport model (e.g., WRF). DuMo contains the following components: a suite of dust emission schemes, a terrestrial preprocessor, multiple dust injection schemes, dry removal and dust optics module (Figure 5).

2.3.2.1 Dust emission schemes

One simple and two physically based dust emission schemes are currently implemented in DuMo (see Appendix A). The vertical dust flux calculated with the simple scheme is directly proportional to the cube of the friction velocity. One of the physically based dust emission schemes consists of the *Alfaro and Gomes* [2001] energy-based vertical flux model and the saltation parameterization of *Marticorena and Bergametti* [1995] (hereafter denoted as MB95). The threshold friction velocities are calculated following the *Iversen and White* [1982] threshold friction velocity equations, and moisture and roughness corrections follow *Fécan et al.* [1999] and *MacKinnon et al.* [2004] parameterizations. The other physically based dust emission scheme follows the work of *Shao et al.* [1996] with more recent improvements (hereafter denoted as Shao96). The threshold friction velocity parameterization follows the *Shao and Lu* [2000] approach, the moisture correction is calculated with *Fécan et al.* [1999] parameterization and the roughness correction is done by using a drag double partitioning scheme [*Shao*, *personal communication*, 2007]. Detailed description and intercomparison of MB95 and Shao96 schemes are available in *Darmenova et al.* [2008].

The input required for dust emission schemes is provided either from WRF simulations or external datasets. A terrestrial preprocessor was developed to provide gridded data for aeolian roughness and undisturbed (dry-sieved) soil particle size distributions. The aeolian roughness for Central and East Asia was derived from the POLDER instrument. Undisturbed soil particle size distributions for Central and East Asia are available from *Laurent et al.* [2006] and *Petrov* [1976]. In addition, USDA texture-based soil distributions are also incorporated in DuMo.

2.3.2.2 Dust injection schemes

1-st (surface) model layer injection scheme

This scheme considers that the emitted dust flux F is injected in the first (surface) model

layer. The injection height is equal to the height of the 1-st (surface) model layer Δz_1. The vertical profile of the emitted dust is:

$$c(z) = \begin{cases} F/\Delta z_1 & z \leq \Delta z_1 \\ 0 & z > \Delta z_1 \end{cases} \tag{8}$$

This scheme inexplicitly assumes that the mixing provided by the PBL scheme is sufficient to model the vertical profile of the atmospheric dust during emission.

Homogeneous injection in the PBL

In this scheme, the emitted dust flux F is injected and homogeneously mixed within the PBL with height H_{PBL}. Therefore, the vertical profile of the emitted dust is:

$$c(z) = \begin{cases} F/H_{PBL} & z \leq H_{PBL} \\ 0 & z > H_{PBL} \end{cases} \tag{9}$$

If one considers a constant mass mixing ratio $q(z) = q_{PBL}$ instead of a constant concentration in the PBL, then

$$F = \int_0^{H_{PBL}} c(z)dz = q_{PBL} \int_0^{H_{PBL}} \rho_{air}(z)dz$$

Therefore, the mass mixing ratio is:

$$q_{PBL} = F/ \int_0^{H_{PBL}} \rho_{air}(z)dz$$

and the concentration profile is:

$$c(z) = \begin{cases} F\rho_{air}(z)/ \int_0^{H_{PBL}} \rho_{air}(z)dz & z \leq H_{PBL} \\ 0 & z > H_{PBL} \end{cases} \tag{10}$$

Exponential injection in the PBL

In this injection scheme, the emitted dust flux F is injected and mixed in the PBL following an exponential profile up to the height of the PBL:

$$c(z) = c_0 \, exp(-z/H_{PBL}).$$

The constant c_0 can be found from the mass conservation principle

$$F = \int_0^{H_{PBL}} c(z)dz = c_0 \int_0^{H_{PBL}} exp(-z/H_{PBL})dz$$

to be equal to $c_0 = \frac{1}{1-e^{-1}} F/H_{PBL}$ and, therefore, the vertical profile of the instantaneous dust emission is:

$$c(z) = \begin{cases} \frac{1}{1-e^{-1}}\ F/H_{PBL}\ exp(-z/H_{PBL}) & z \le H_{PBL} \\ 0 & z > H_{PBL} \end{cases} \tag{11}$$

In a sense, this scheme can be viewed as a hybrid between the 1-st (surface) model layer injection and the homogeneous injection in the PBL.

2.3.2.3 Parameterizations of dry removal processes

Dry removal is the primary sink of dust particles, especially, in the vicinity of dust sources. In contrast to wet removal it works continuously during the lifespan of airborne dust. Modeling the dry removal of mineral aerosol particles requires accurate specification of the gravitational settling (sedimentation) and dry deposition onto the surface.

The gravitational settling velocity is given by Stokes Law:

$$v_s = \frac{\rho_p D_p^2 g C_c}{18\mu} \tag{12}$$

where ρ_p is the density of the particle D_p is the particle diameter, g is the gravitational acceleration, μ is the viscosity of air and C_c is the slip correction factor given by:

$$C_c = 1 + \frac{2\lambda}{D_p}\left(1.257 + 0.4e^{-0.55D_p/\lambda}\right) \tag{13}$$

where λ is the mean free path of air molecules.

The flux of material to the surface is commonly assumed to be proportional to the concentration c of the depositing species at some reference height above the surface:

$$F_d = -v_d c \tag{14}$$

where F_d is the vertical dry deposition flux. The constant of proportionality v_d between the flux and the concentration is known as deposition velocity.

The process of dry deposition of particles is represented by three separate mechanisms: aerodynamic transport through the atmospheric column to a thin layer adjacent to the surface; Brownian transport across the thin layer; uptake at the surface. Each of these mechanisms contributes to the value of the deposition velocity v_d.

The deposition process is commonly interpreted in terms of an electrical resistance analogy, in which the transport of particles to the surface is expressed as three resistances in series. The aerodynamic resistance r_a, the quasi-laminar resistance r_b and the canopy resistance r_c.

$$v_d = \frac{1}{r_a + r_b + r_c} \tag{15}$$

For particles it is usually assumed that they adhere to the surface upon contact so the canopy resistance r_c is equal to zero.

Wesley [1989] developed a methodology for dry deposition calculations that have been widely adopted in regional models, including WRF. The dry deposition velocity is given by:

$$v_d = \frac{1}{r_a + r_b + r_a r_b v_s} + v_s \tag{16}$$

where r_a is a complex function of the atmospheric stability [*Seinfeld and Pandis*, 1998] and the quasi-laminar resistance for particles r_b is:

$$r_b = \frac{1}{u_* \left(Sc^{-2/3} + 10^{-3/St} \right)} \tag{17}$$

where u_* is the friction velocity and Sc and St are the Schmidt and Stokes number, respectively.

2.3.2.4 Zero order sedimentation scheme

The rate of change of the atmospheric dust concentration due to gravitation settling is:

$$\frac{dc}{dt} = -\frac{d}{dz}\left(v_s c\right) \tag{18}$$

where c is either the particle mass or number concentration. In order to solve this equation numerically one can apply a zero order scheme, which assumes that the fraction $v_s \Delta t / \Delta z$

of the total mass/number in a model cell with vertical extend Δz will fall out. The mass conservation principle dictates that the amount of particles falling down from one cell into the next cell bellow are equal, therefore Equation 18 becomes

$$\frac{\Delta c_k}{\Delta t} = \frac{v_{s,k+1}}{\Delta z_{k+1}} c_{k+1} - \frac{v_{s,k}}{\Delta z_k} c_k \tag{19}$$

2.3.2.5 Parameterization of dust particle optics

Dust particles are assumed to be homogeneous spheres. The optical properties are computed with Mie theory with the following input parameters: complex refractive index and the dimensionless size parameter $\chi = 2\pi r/\lambda$ connecting the particle radius r and the wavelength λ of the incident electromagnetic radiation. The description of Mie scattering by an ensemble of particles is done by integrating the given quantity over the size distribution $n(r)$. For example, the volume extinction coefficient is calculated as

$$\beta_e = \int_{r_{min}}^{r_{max}} \sigma_e(r) n(r) dr \tag{20}$$

where σ_e is the extinction cross section of a particle with radius r. Calculating the integral is numerically expensive to be done in real time. However, the calculations can be sped up in case of a lognormal particle size distribution (Equation 5). In this case, a lookup table with the values of the integral can be calculated for a given wavelength, refractive index of the particles, standard deviation and set of discrete values of the mean diameter. Then, the true extinction coefficient for a particular mean diameter and particle concentration per unit volume n can be calculated as the product of the interpolated extinction coefficient and n.

Next, the dust optical thickness (DOT) can be calculated from the modeled number n_k and mass m_k concentrations in the vertical layer k:

$$\tau = \sum_{k=1}^{k=k_{top}} n_k \beta_e(r_k) \Delta z_k \tag{21}$$

where r_k is the mean geometrical radius, $\beta_e(r_k)$ is the (interpolated) volume extinction coefficient and Δz_k is the height of the k-th vertical layer. The mean geometrical radius r_k can

be calculated from n_k, m_k and the known standard deviation σ_g:

$$r_k = \frac{1}{2}\left[\frac{6}{\pi} exp\left(-4.5 log^2 \sigma_g\right) \frac{m_k}{\rho_p n_k}\right]$$

Once the concentration and the extinction coefficient in the first (surface) layer are known one can also calculate the visibility following the Koschmieder's law that relates daytime visibility V and extinction coefficient $\beta_e^1 = n_1 \beta_e(r_1)$ via:

$$V = \frac{3.912}{\beta_e^1} \tag{22}$$

2.3.3 Coupling DuMo with WRF

The newly developed modeling system WRF-DuMo (Figure 6) contains three types of coupled components: (1) a meteorological modeling system for the description of atmospheric states and motions (WRF), (2) dust module DuMo and (3) dust transport-deposition module for simulation of the atmospheric dust evolution. The transport-deposition module includes the following processes: horizontal advection, vertical advection, mass conservation adjustments for advection processes, horizontal diffusion, vertical diffusion, aerosol dynamics, size distributions and aerosol deposition velocity estimation. It is based on a modified WRF-CHEM version 2.1.2. As a proof of a concept, WRF-CHEM (2.1.2), which lacked dust emission, was first linked with the dust emission module implemented in DuMo and several representative cases of dust events were successfully simulated. The next step was to remove the chemistry specific and non-essential for dust modeling parts of WRF-CHEM. Among the advantages of the customized version of the CHEM module were a much smaller code base and a speed up by a factor of ten times. Also, a significant run-time memory reduction was achieved that made it possible to perform a detailed dust modeling at a fine scale. The next released version of WRF (2.2.0) did not include the CHEM module. In order to keep our weather prediction module up to date with the WRF release, the dust aerosol module (customized CHEM) was successfully ported to and coupled with WRF-2.2.0 in a short amount of time. The capabilities of the dust aerosol-transport module

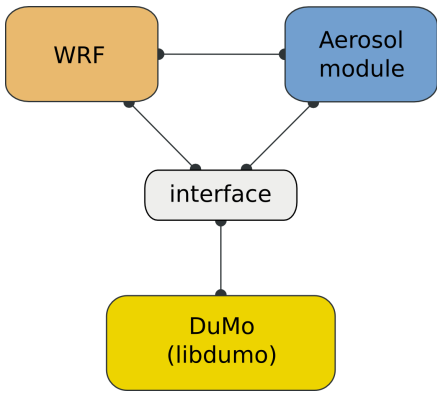

Figure 6: WRF-DuMo modelling system components.

were further extended to include three modal representation of dust aerosols and gravitational sedimentation. Modifications to the WRF model were needed as well, in order to accommodate the new capabilities of the WRF-DuMo system. Currently WRF-DuMo uses its own registry file (Registry.EM_DUMO). Dust vertical flux, mass and number concentrations, and deposition velocity are included by default in the WRD-DuMo output files. Also, a new block 'dumo' was added in the namelist file. It contains all DuMo options that can be controlled by the user. For more details see Appendix B.

2.4 Investigation of the importance of initial dust size distributions and injection heights

In Section 2.2 we identified several pertinent problems in dust modeling, including uncertainties in the initial size distribution and injection mechanism of freshly emitted dust aerosols. This motivated us to explore the differences in the modeled dust fields caused by changes in the prescribed initial dust size distribution (i.e., initial mass median diameter and modal weight) and dust injection.

In this study we modeled two representative dust events, which occurred in the springs of 2001 and 2007 in East Asia. In the spring season, formation of dust storms over Central and East Asia is commonly associated with cyclonic cold fronts [*Warner*, 2004]. This was also the case with the two considered events. The synoptic situation was very similar in

both cases - a powerful cyclone originating over Mongolia and Northwest China caused strong northwesterly winds across the desert regions in China and Mongolia. This resulted in severe dust storms that were subsequently transported over thousands of kilometers.

The 2001 dust storm, which is well known in the community as the "Perfect dust storm", reached as far as the west coast of the USA [*Darmenova et al.*, 2005]. The 2001 dust storm lasted 7 days (5 – 11, April). On 5–6 April, intense dust emission started in the Taklamakan desert, followed by dust mobilization in Chinese and Mongolian Gobi on 7 April. On 8 April, a second cold surge swept trough China, causing another dust storm in the Gobi region. Dust plumes from both storms merged over the Kamchatka Peninsula and were transported across Korea, Japan and the Pacific Ocean.

The storm of 31 March, 2007 was a result of the combined effect of several weather systems. As the storm began on 30 March, 2007, the primary driver was a low pressure cyclone stagnating over eastern Mongolia. A cold front surging out of the Lake Baikal region started moving steadily towards China-Mongolia. On the 31st, as the low-pressure system completely occluded, a cold front blasting out of the Tarim Basin struck the dust front. By 1 April, the cold front from the west had pushed dust over the Korean Peninsula to Japan.

A set of modeling experiments was designed to assess the relative importance of the initial size distribution and injection scheme. For a base run we selected the '1-st layer' injection scheme and initial mass median diameters (MMDs) and weights of 1.5 μm and 8 μm, and 0.3 and 0.7 for the fine and coarse mode, respectively. The MMD values and weights were varied by ±30%. Table 5 summarizes the setup used to perform the modeling experiments. The parameters were independently varied resulting in 3 (MMDs) × 3 (weights) × 3 (injection schemes) or total of 27 modeling experiments for each of the two dust events.

WRF-DuMo was ran at 40×40 km horizontal resolution and with 36 vertical levels. Because of the long time it would take to perform the 27 runs (for each event), we used the

Table 5: Initial size distribution MMDs, weights and injection schemes that are used in the modelling experiments. The geometric standard deviations of the fine and coarse modes are 1.7 and 1.6 respectively. Highlighted are the values used in the base experiment (S2-W2-I1).

MMD [μm]			weight			injection	
name	fine	coarse	name	fine	coarse	name	scheme
S1	1.00	5.33	W1	0.2	0.8	I1	1-st layer
S2	1.50	8.00	W2	0.3	0.7	I2	homogeneous
S3	2.00	10.67	W3	0.4	0.6	I3	exponential

Color and pattern coding

S1	- - - - - -	W1	
S2	————	W2	
S3	----------	W3	

'simple' emission scheme. The constant of proportionality C (see Appendix A, Equation 46) was tuned so that the total emitted dust mass with the simple scheme was equal to the average emitted mass calculated with MB95 and Shao96 schemes. Comparison against the physically based schemes confirmed that the 'simple' scheme produced similar emission patterns and further justified its use.

To investigate the effect of the initial size distribution and injection on dust spatiotemporal distribution, we analyzed commonly used characteristics of dust such as: particle sizes and concentrations at the surface, visibility, total column integrated mass, dust optical thickness (DOT) and vertical distribution of the dust plume. In particular, to investigate the evolution of dust particle sizes within the dust plume, we analyzed the timeseries of the MMDs in four different locations: Lintai (Taklamakan desert), Dalanzadgad (Mongolian Gobi), Beijing and Seoul. Similarly, we analyzed the temporal evolution of DOTs and visibility during the 2001 outbreak at the same locations. The selection of these locations was dictated by the origin and the transport route of the dust plume - it originated from the Taklamakan and Gobi and was transported to the east over Northeast China, Korea and

Japan.

Figure 7 shows the time series of the fine mode MMDs in the first model layer in Lintai and Dalanzadgad. The solid black line represents the median value of the 27 experiments while the black dashed line corresponds to the base experiment. The gray shaded area shows the range of the simulated values from all experiments. The time series of fine mode MMDs on 8 April are shown as separate insets for each injection scheme to facilitate interpretation of the observed differences. This date was selected for several reasons. Firstly, this time frame is in the middle of the simulation when the spin up of the model is not an issue. Secondly, the dust storm was already well developed on 8 April. It is evident that fine mode MMDs slightly increased on 5 April and then around 7–9 April, a time period that coincides with the two separate dust emission episodes during the "Perfect dust storm" that occurred in the Taklamakan Desert. It can be seen than MMDs start to decrease gradually from 9 April to 11 April. In contrast, fine mode MMDs over Dalanzadgad (Figure 7, bottom panel) does not show clearly the two dust emission episodes but many short pulses. This can be explained by the differences in the nature of dust episodes in the Gobi and Taklamakan. Since soil particles in the Taklamakan are finer than those in the Gobi, they are easily mobilized but are rarely transported downwind because of the sheltering effect of the Tian Shian Mountains and the Tibetan Plateau. As a result, dust events in Taklamakan often manifest as a continuous dust haze (floating dust). In contrast, dust emission in the Gobi exhibits sporadic nature and shows a fast response to changes in wind forcing. Dust plumes originating in the Gobi are efficiently transported downwind. It can be also seen that the change in the injection scheme and the initial weight of the size distribution does not affect significantly fine mode MMDs. The lack of response of the fine mode MMDs to the initial weights during active emission periods can be explained by the continuous supply of fresh particles from the underlying source bed.

Figure 8 shows the time series of fine mode MMDs in Beijing and Seoul. In contrast

to the stations in the desert regions, fine mode MMDs increase during the end of the simulation, indicating that fine mode particles were efficiently transported to these locations. Another interesting finding is that fine mode MMDs show higher sensitivity to the prescribed initial weights. In addition, it can be observed that fine mode MMDs in Seoul are more sensitive to initial weights compared to those in Beijing. Since deposition is strongly dependent on particle sizes, it becomes more important further away from dust sources. Dust particles will be removed at different rates depending on the initial weights and particle diameters. Another finding is that fine mode MMDs show higher sensitivity to change in the injection scheme compared to those located in source regions (Figure 7).

Figure 9 shows that the behavior of the coarse mode MMDs in Lintai and Dalanzadgad is very similar to that of the fine mode MMDs. However, we can see that the coarse mode MMDs decrease faster compared to the fine mode because large particles are removed more efficiently. Similarly to fine mode MMDs, coarse mode MMDs show low sensitivity to initial weights and injection schemes and depend mainly on the initial particle sizes.

The time series of coarse mode MMDs in Beijing and Seoul (Figure 10) show high temporal variability compared to the fine mode MMDs. This behaviour, especially in the case of Seoul, is likely caused by the small number of coarse particles. These fluctuations, however, should not affect visibility or dust optical thickness calculations, because of the small number of particles. The coarse mode MMDs in Beijing, similarly to Lintai and Dalanzadgad, depends mainly on the initial particle sizes, while coarse mode MMDs in Seoul shows a complex behavior affected by the initial weights and particle sizes and to a lesser extent by the injection scheme.

The combined effect of the initial sizes (fine and coarse mode) and injection schemes on both dust particle size and concentration in the first model layer can be demonstrated by analyzing the modeled visibility. Figures 11 and 12 show timeseries of visibility in Lintai and Dalanzadgad, and Beijing and Seoul, respectively. The dust episodes are clearly

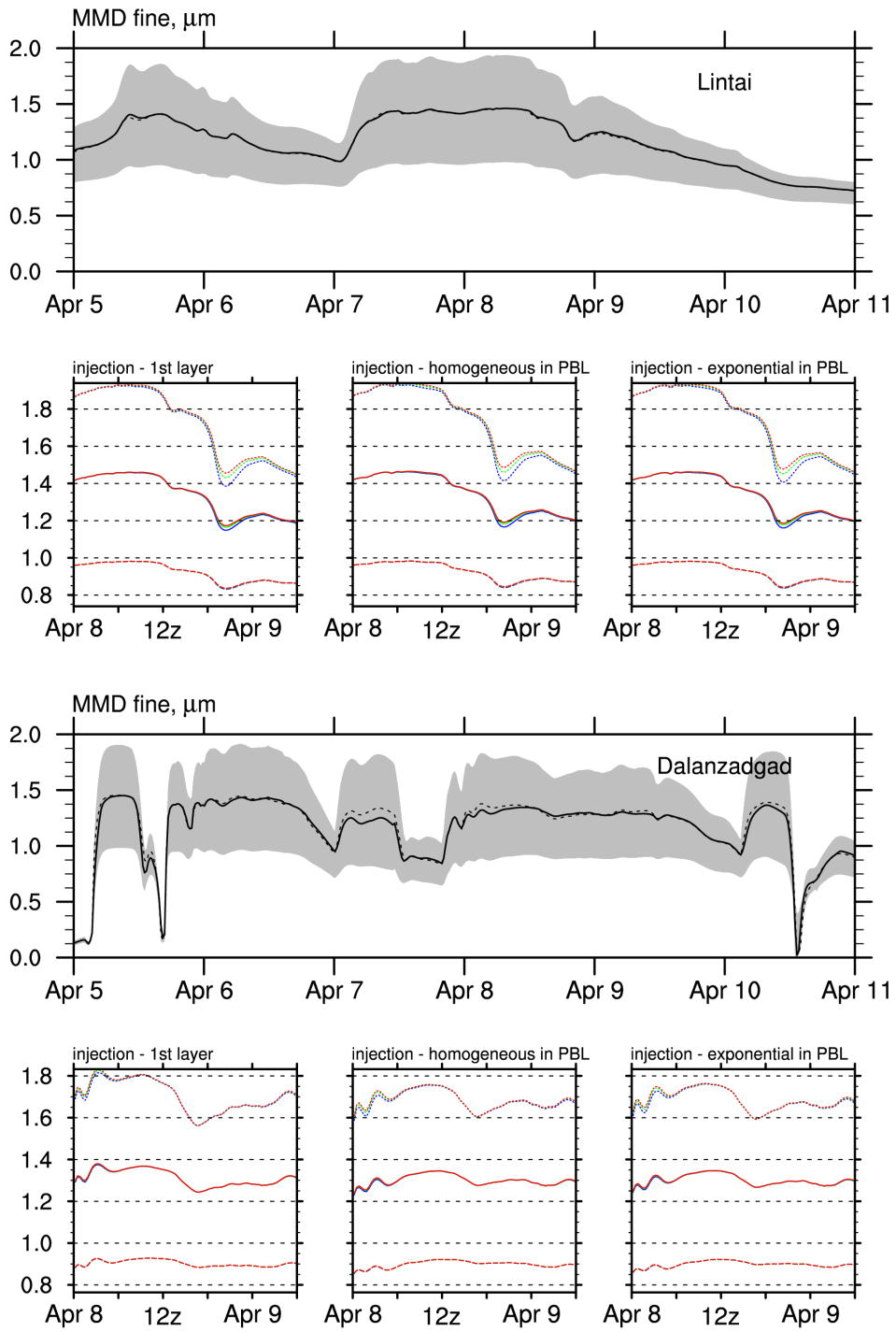

Figure 7: Time series of fine mode MMD for 5–11 April, 2001 in the 1-st (surface) model layer. Lintai (top) and Dalanzadgad (bottom) were selected as representative locations in source regions. The solid black line shows the median value of the 27 modeling experiments. The shaded area shows the modeling experiments spread. The dashed line shows the base-run experiment values. Also shown are the MMDs on 8 April split by injection scheme. The color and pattern coding follows Table 5, i.e. the line corresponding to experiments S3-W1-∗ is --------.

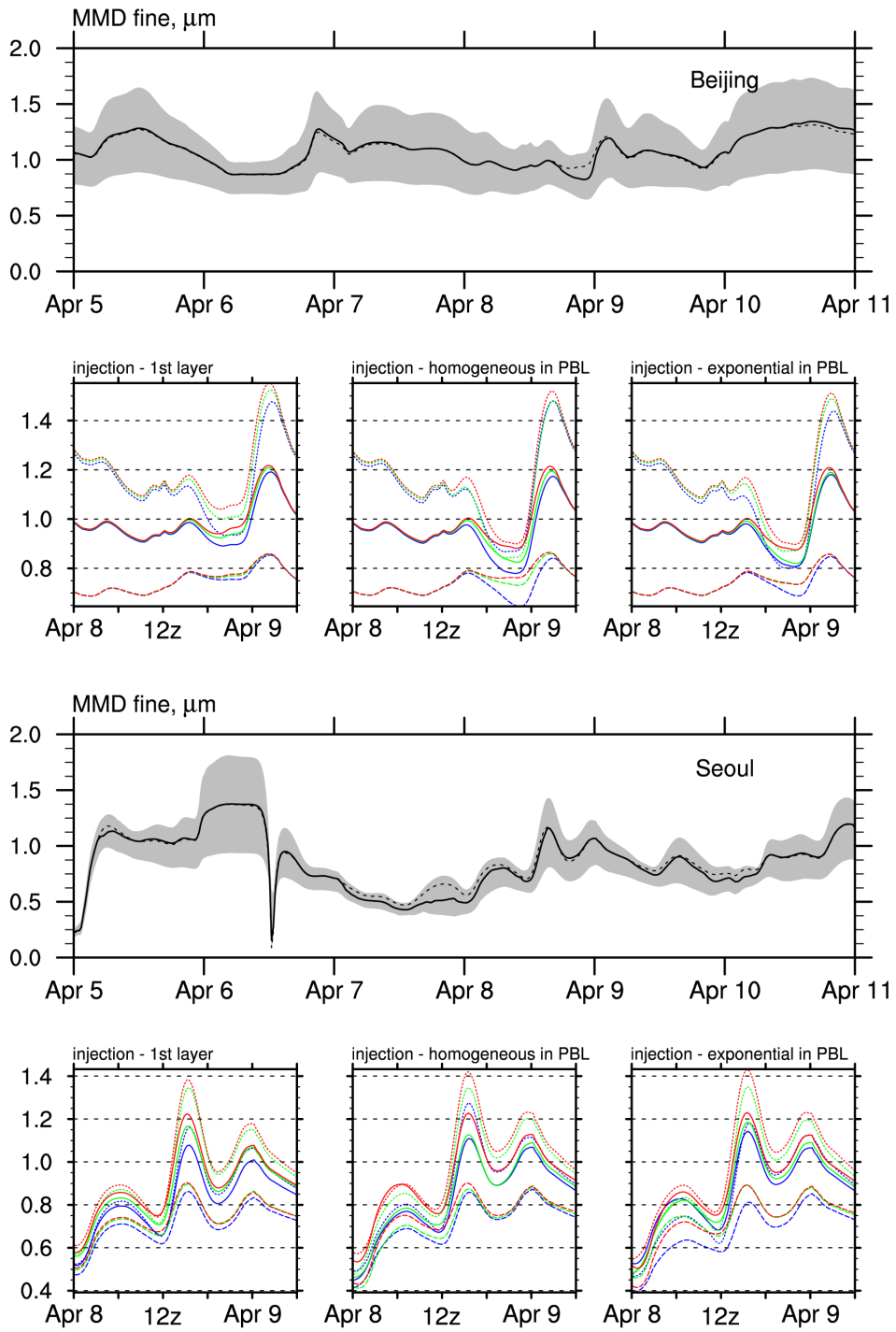

Figure 8: Time series of fine mode MMD for 5–11 April, 2001 in the 1-st (surface) model layer. Beijing (top) and Seoul (bottom) were selected as representative locations for mid-range transport downwind. The solid black line shows the median value of the 27 modeling experiments. The shaded area shows the modeling experiments spread. The dashed line shows the base-run experiment values. Also shown are the MMDs on 8 April split by injection scheme. The color and pattern coding follows Table 5, i.e. the line corresponding to experiments S3-W1-$*$ is - - - - - - - -.

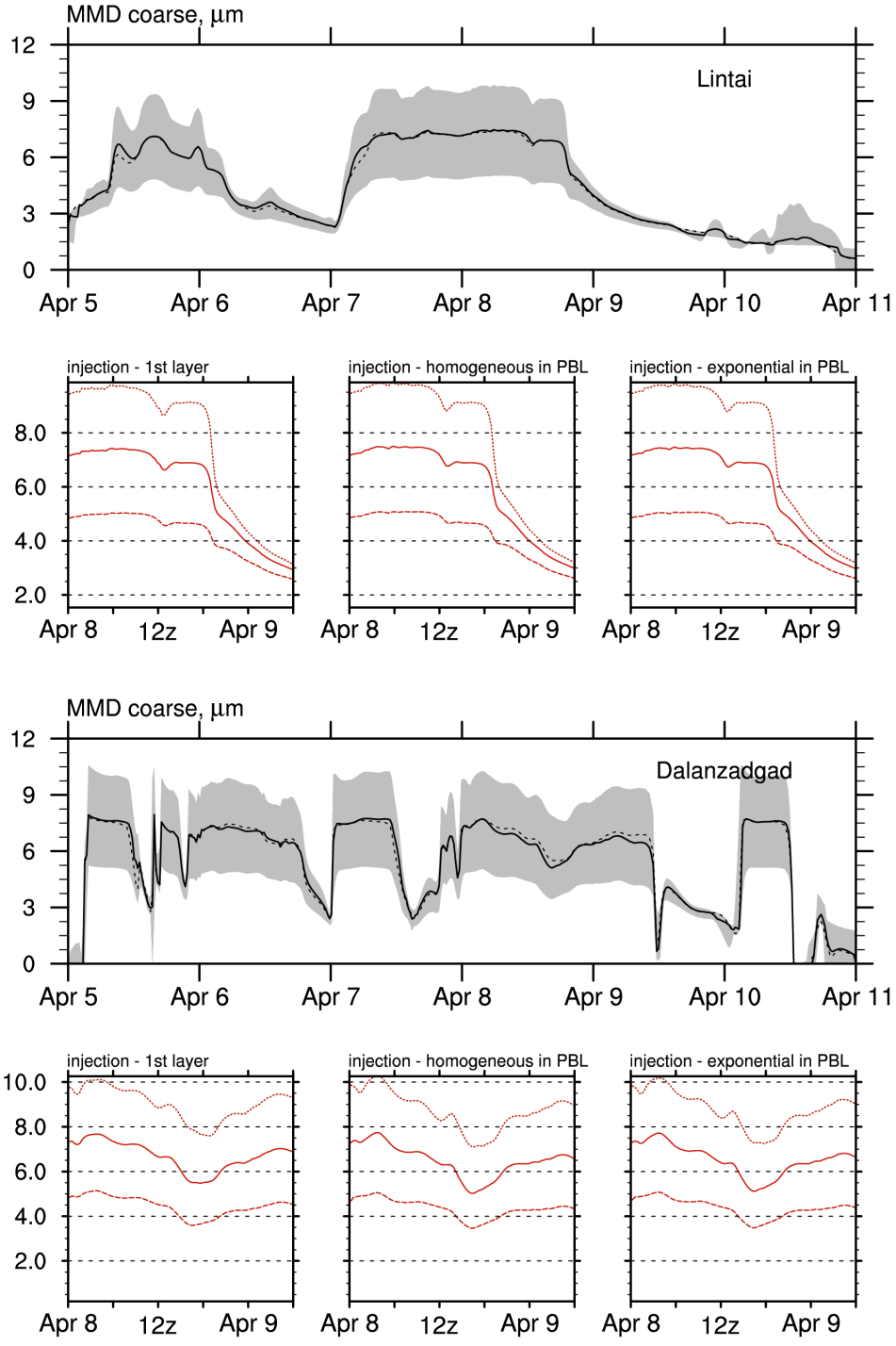

Figure 9: Same as Figure 7, except for coarse mode MMD.

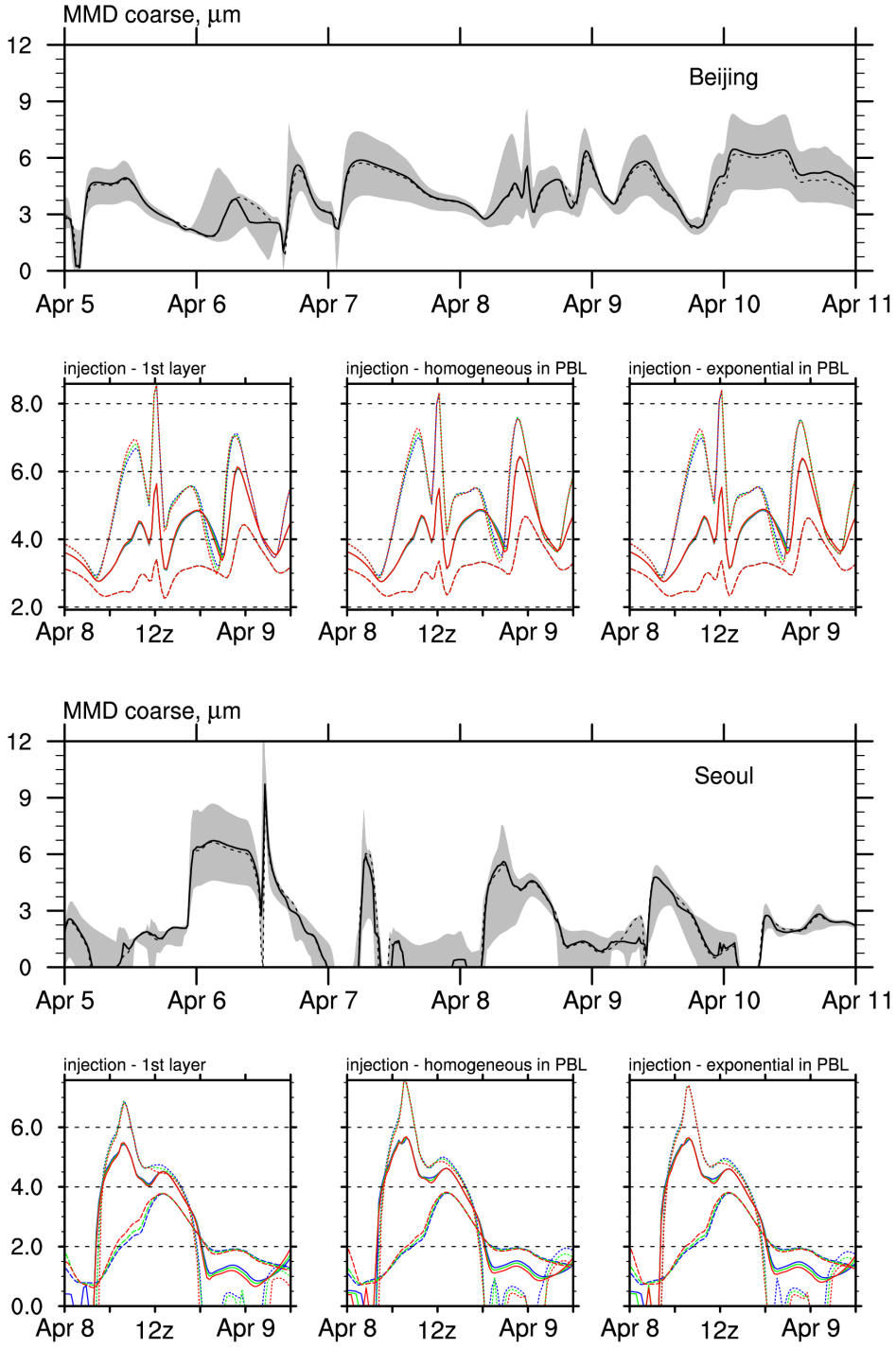

Figure 10: Same as Figure 8, except for coarse mode MMD.

marked with sharp decrease in the visibility. Beijing and Seoul experience different magnitude and timing of decreased visibility due to the specific direction of the dust plume transport. One can see that visibility is affected by both initial sizes and weights, and to a lesser extent by the choice of injection scheme. The highest visibility is modeled by the S3-W1-* experiments, while the lowest is modeled by the S1-W3-* experiments.

Next, we investigate the observed differences in the column integrated properties such as dust optical thickness (DOT). Figure 13 shows the time series of fine mode DOTs in Lintai and Dalanzadgad. Increase in DOTs corresponds to strong emission periods. The S1-W3-* experiments produced the highest values of the fine mode DOT and S3-W1-* experiments produced the lowest, which is consistent with the visibility results. Figure 14 shows the time series of the fine mode DOTs in Beijing and Seoul. It is interesting to observe the time lag of about a day between the maximum of the fine mode DOT in the desert region stations and in the remote stations. Similarly to the short range locations, the maximum DOTs correspond to the S1-W3-* experiments, while the minimum DOTs are produced by the S3-W1-* experiments. Figures 15 and 16 show the coarse mode DOTs at the four locations. In contrast to the fine mode DOTs, one can see that the coarse mode DOTs are clustered depending on the initial sizes. The highest coarse mode DOTs correspond to the S1-W1-* experiments, while the lowest coarse mode DOTs correspond to the S3-W3-* experiments. Figures 17 and 18 show the total DOTs for Lintai, Dalanzadgad, Beijing and Seoul. Total DOT is dominated by the fine mode DOT and behaves in a very similar to it way. Furthermore, for a given initial size distribution, the 'homogeneous' in the PBL injection scheme produces the largest DOTs in all locations, while the '1-st layer' injection scheme produces the lowest DOTs.

The top panels in Figures 19 and 20 show the median dust concentration in the first model layer for all 27 experiments on 8 and 10 April, 2001 (3UTC). The largest dust concentrations for both days were observed over the dust sources. It is apparent from the plots that on 8 April the active dust sources were the Taklamakan Desert, the Chinese and

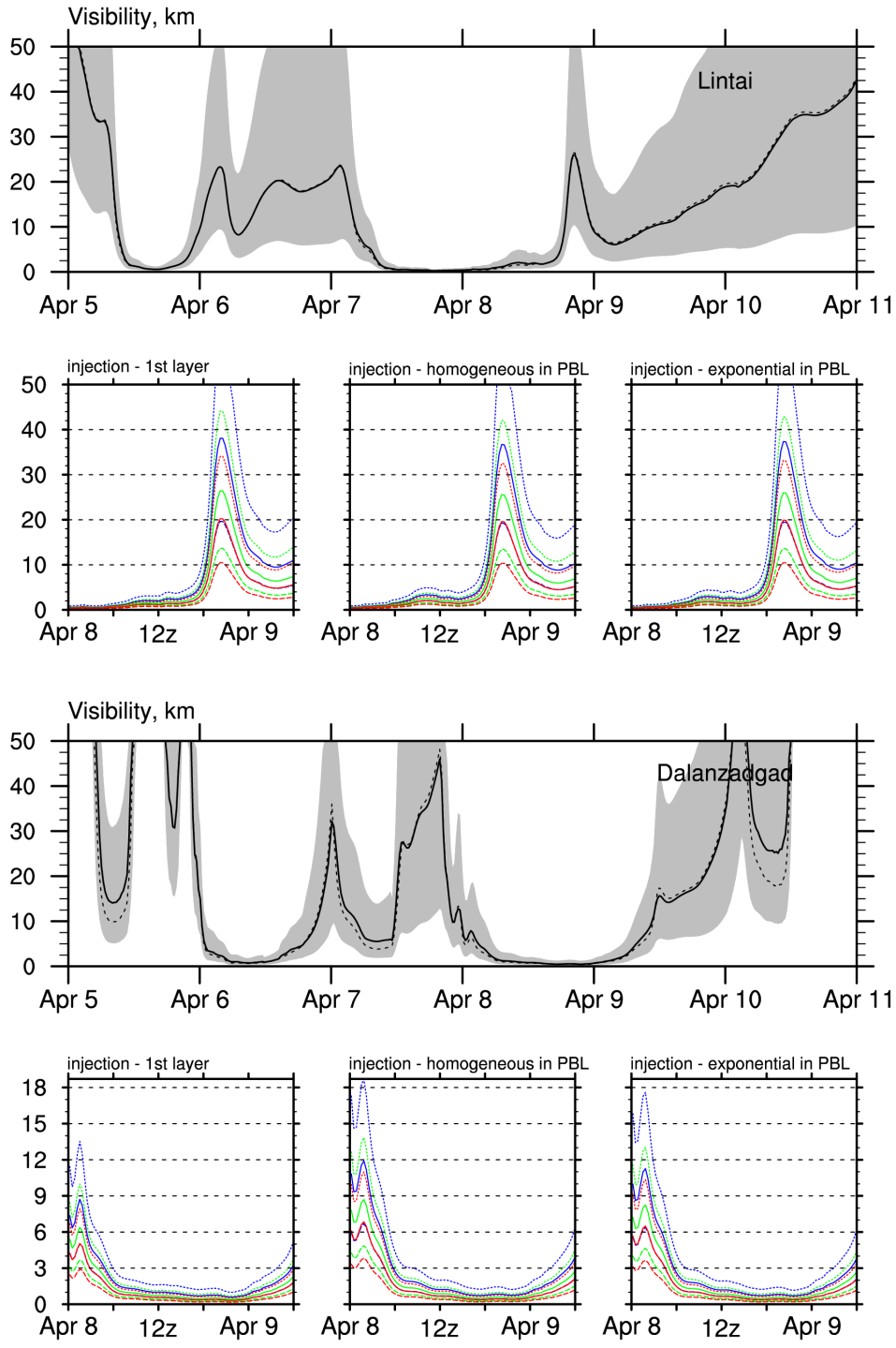

Figure 11: Same as Figure 7, except for visibility.

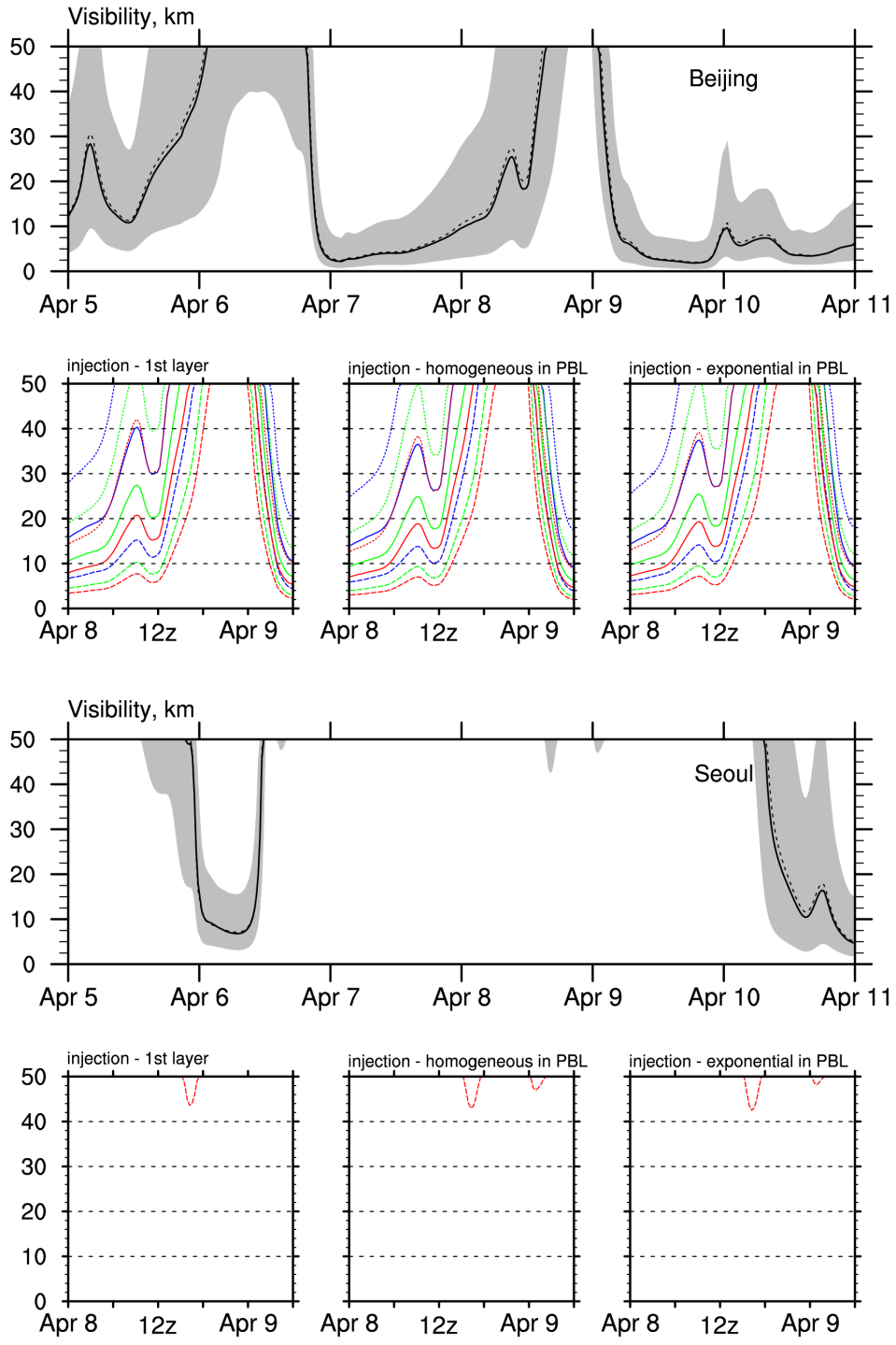

Figure 12: Same as Figure 8, except for visibility.

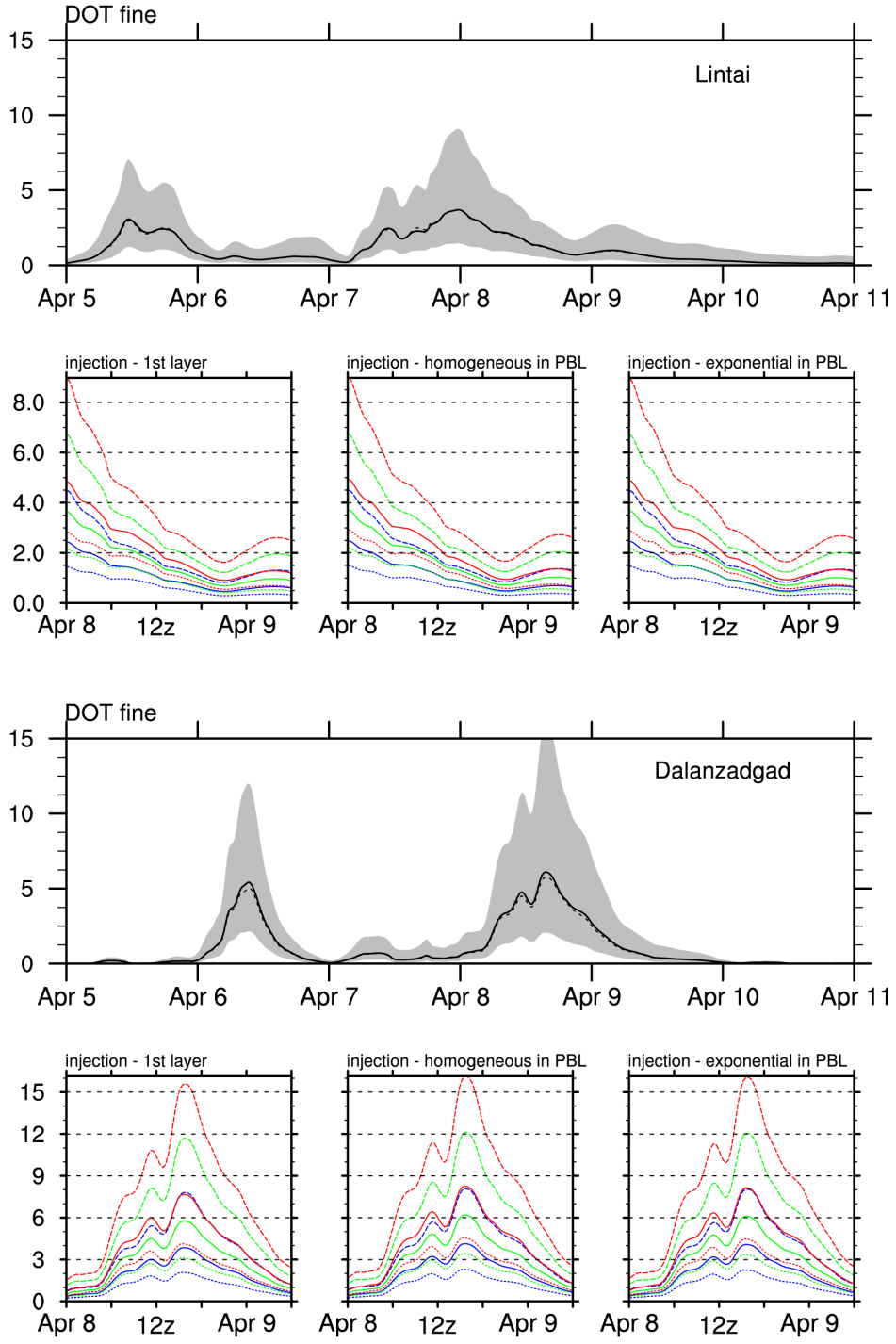

Figure 13: Same as Figure 7, except for fine mode dust optical thickness.

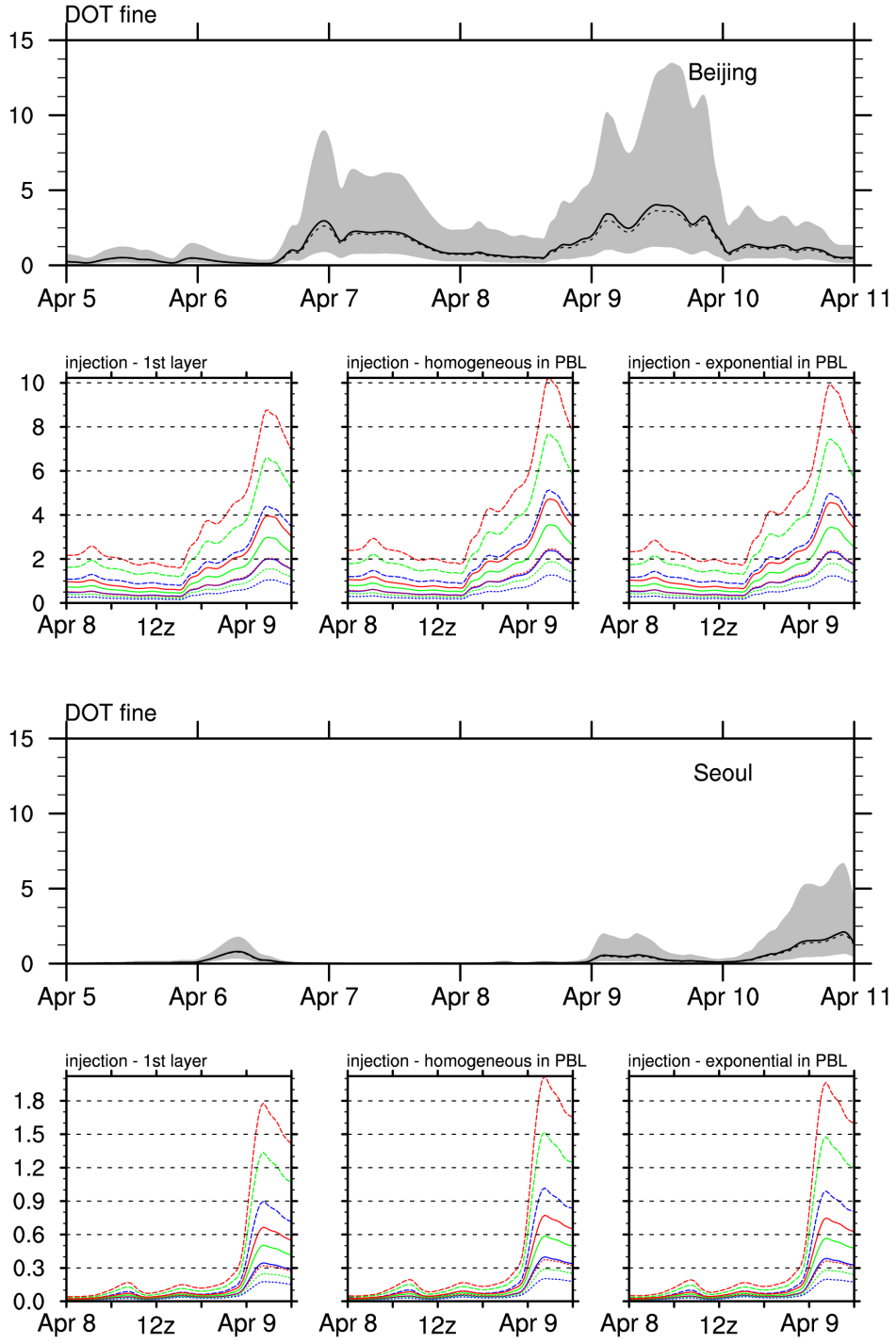

Figure 14: Same as Figure 8, except for fine mode dust optical thickness.

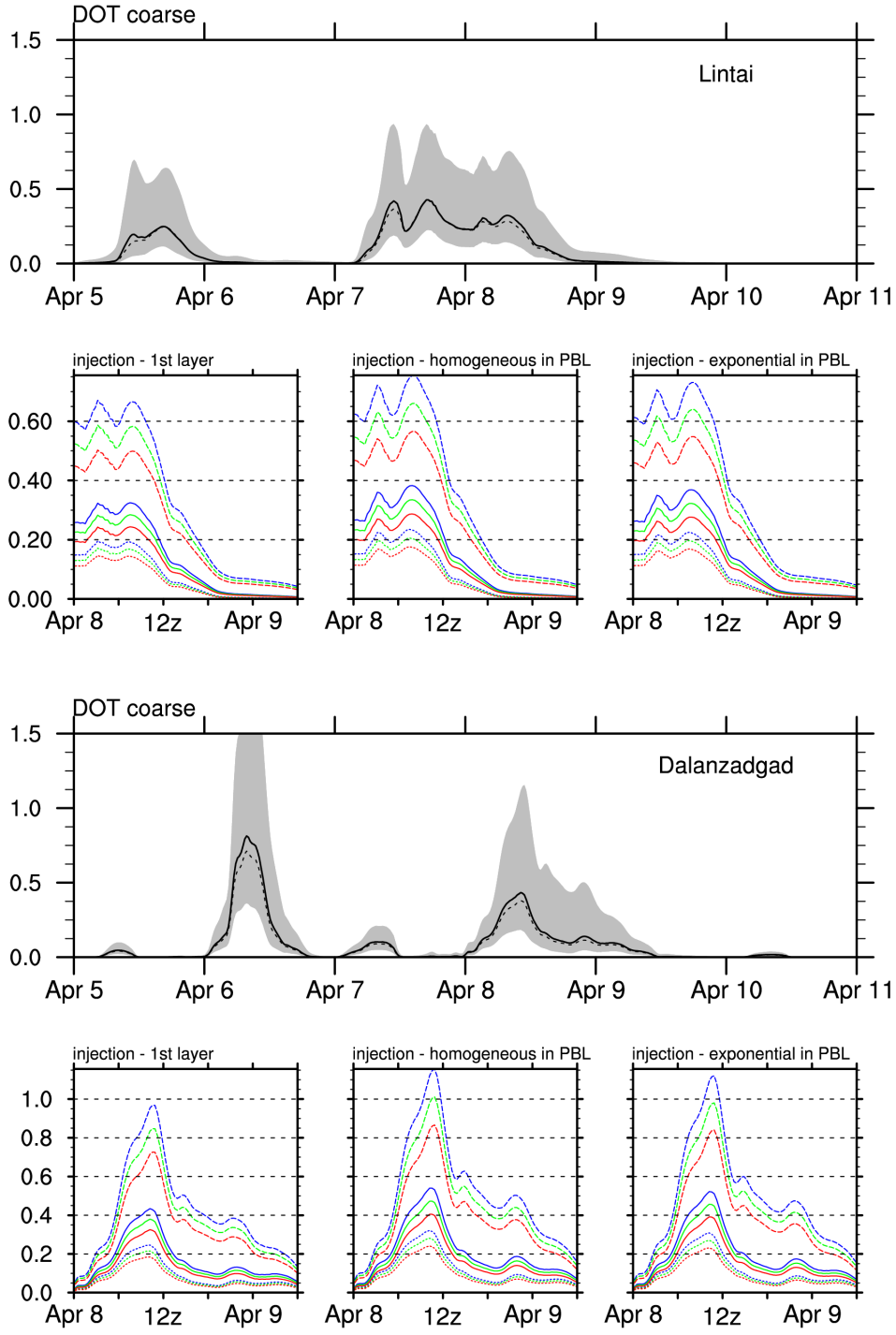

Figure 15: Same as Figure 7, except for coarse mode dust optical thickness.

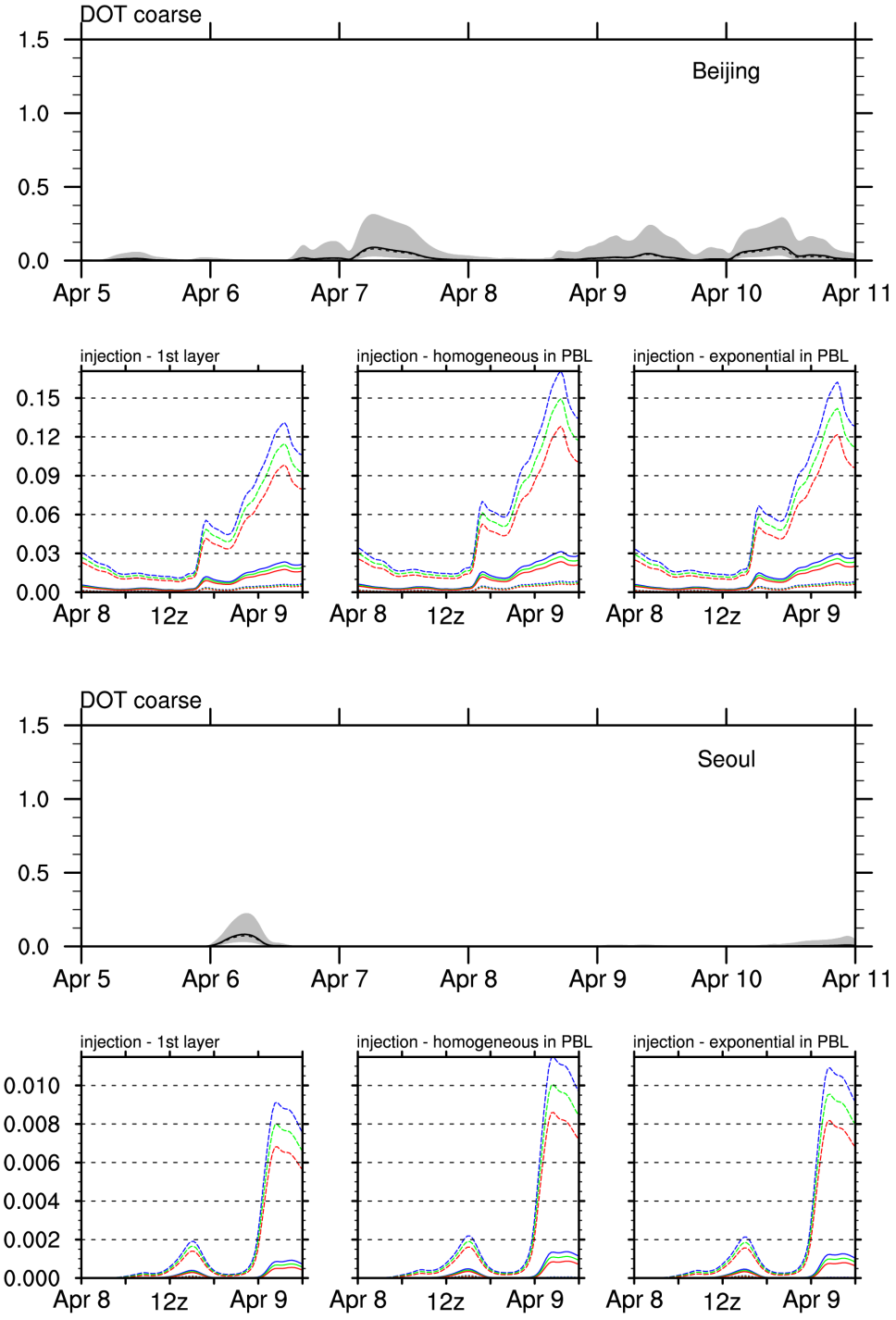

Figure 16: Same as Figure 8, except for coarse mode dust optical thickness.

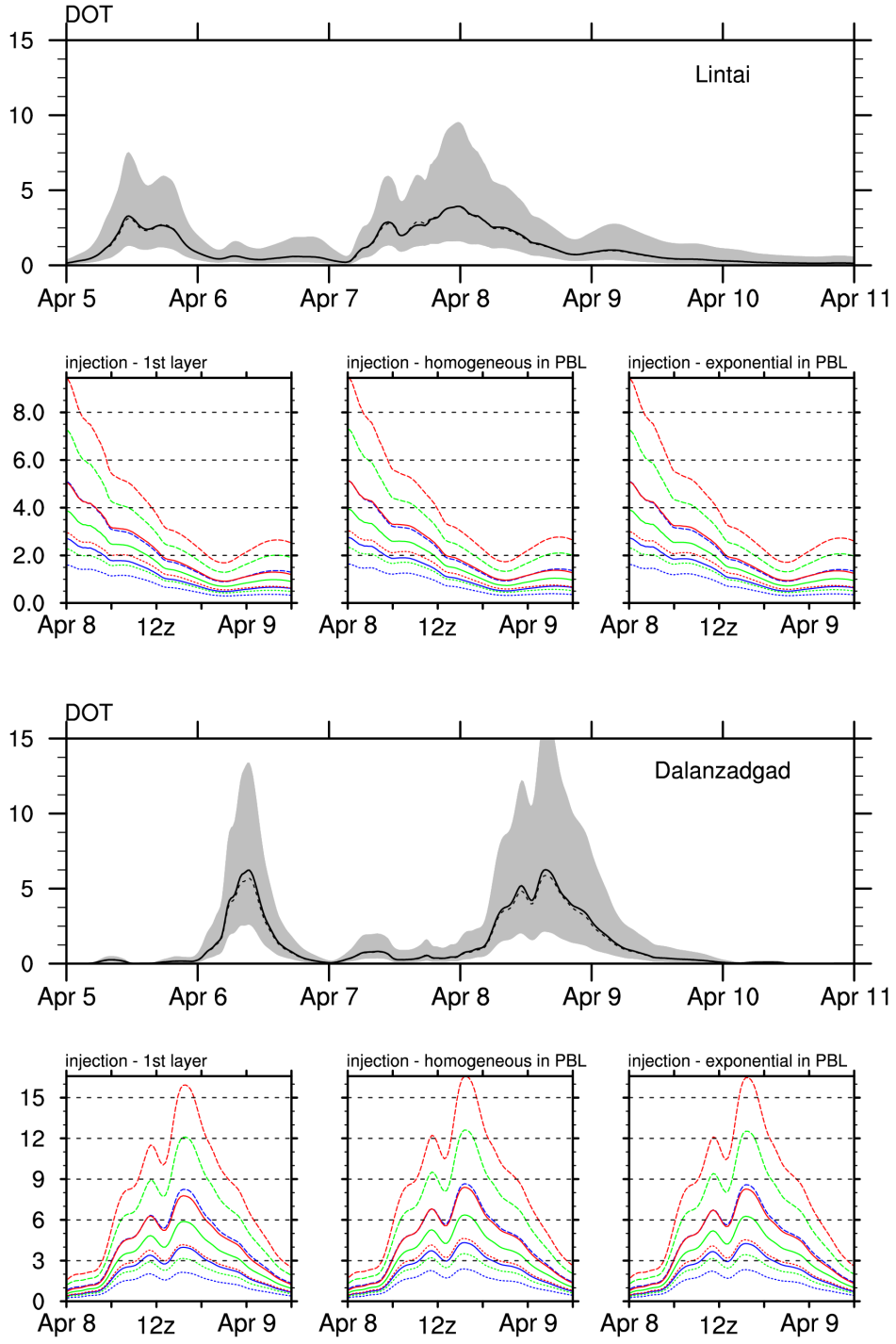

Figure 17: Same as Figure 7, except for total dust optical thickness.

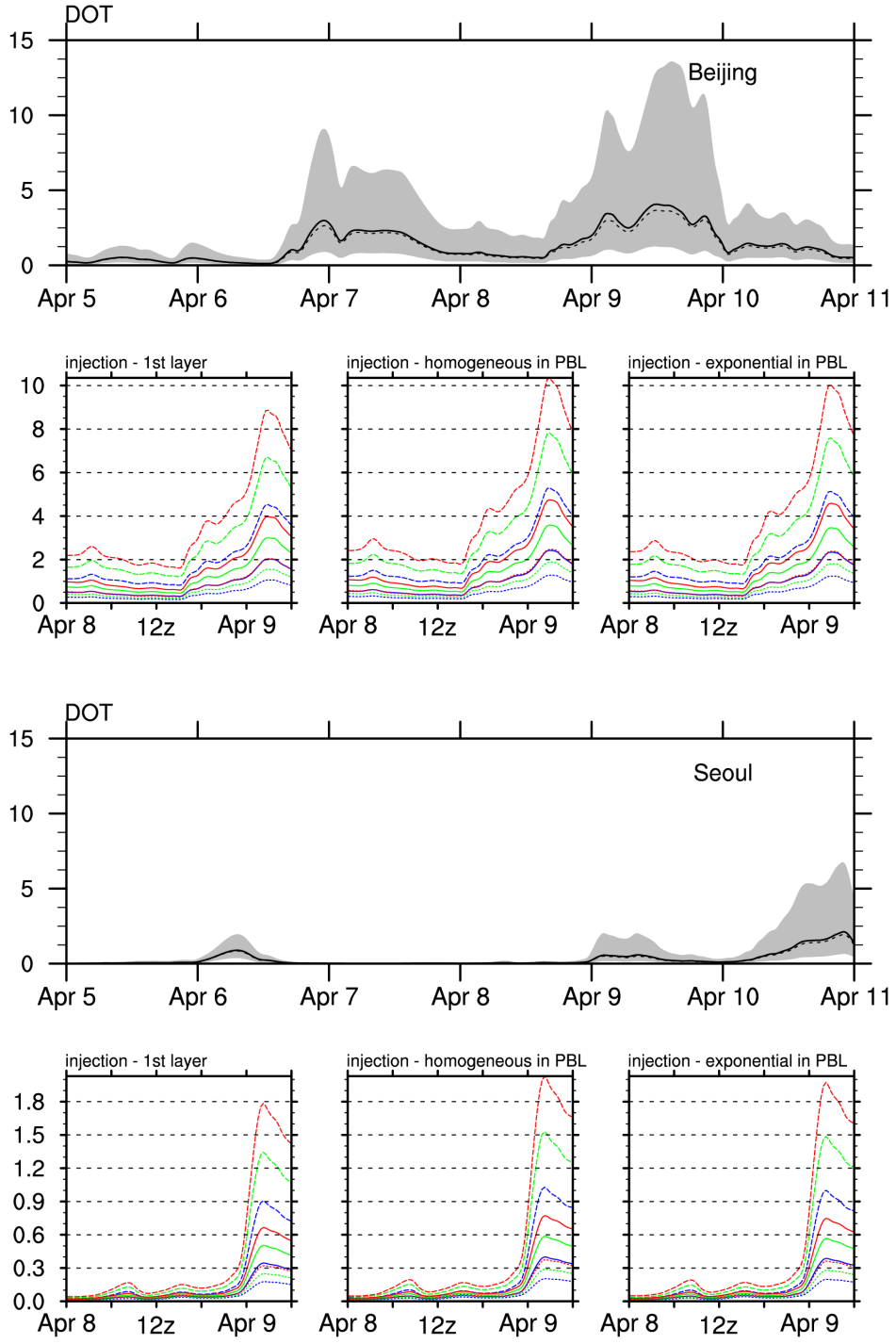

Figure 18: Same as Figure 8, except for total dust optical thickness.

Mongolian Gobi, the agricultural fields in Northeast Asia and the sandy lands around the Balklash Lake. On 10 April, the center of the low-pressure system moved over Northeast Asia resulting in increased dust emission in this region and subsiding activity in the Gobi and Taklamakan. High dust concentrations were also observed over the Tibetial Plateau and South China. This is likely due to the limitations of the simple dust emission scheme, which overestimates erodible areas.

To estimate the variability of the first model layer concentrations, we calculated the standard deviation (STD) from the $N_e = 27$ experiments as:

$$STD(c) = \sqrt{\frac{1}{N_e}\sum_{n=1}^{N_e}(c_n - \bar{c})^2}$$

where $\bar{c}$ is the mean value of all experiments. To measure the scatter from the experiments, we define the scatter ratio as:

$$\epsilon = \frac{STD(c)}{\bar{c}}$$

The scatter ratio ϵ can be interpreted as the uncertainty of the modeled dust fields due to the uncertainties in the initial size distributions and the parameterizations of the injection mechanisms. For this reason, we use interchangeably scatter ratio and 'uncertainty'.

It can be observed from the plots that the standard deviation values (middle panel, Figures 19 and 20) are highest over the active dust sources. However, the largest scatter ratios are observed on the periphery of the transported dust plume. This is most likely due to the propagating in-time differences between the experiments.

To investigate the effect of the initial size distributions and injection schemes on the vertical structure of the dust plume, we analyzed the latitudinal cross section of dust concentrations. Figures 21 and 22 show the results for 8 and 10 April, 2001. We selected the latitude of 40.5°N to ensure that the cross section transects through the major dust emission sources. Figure 21 shows three peaks in the concentration corresponding to the three dust emission hot-spots on 8 April in the Taklamakan, Gobi, and Northeast China. Another interesting feature is that between 2–6 km the concentration appears to be very homogeneous.

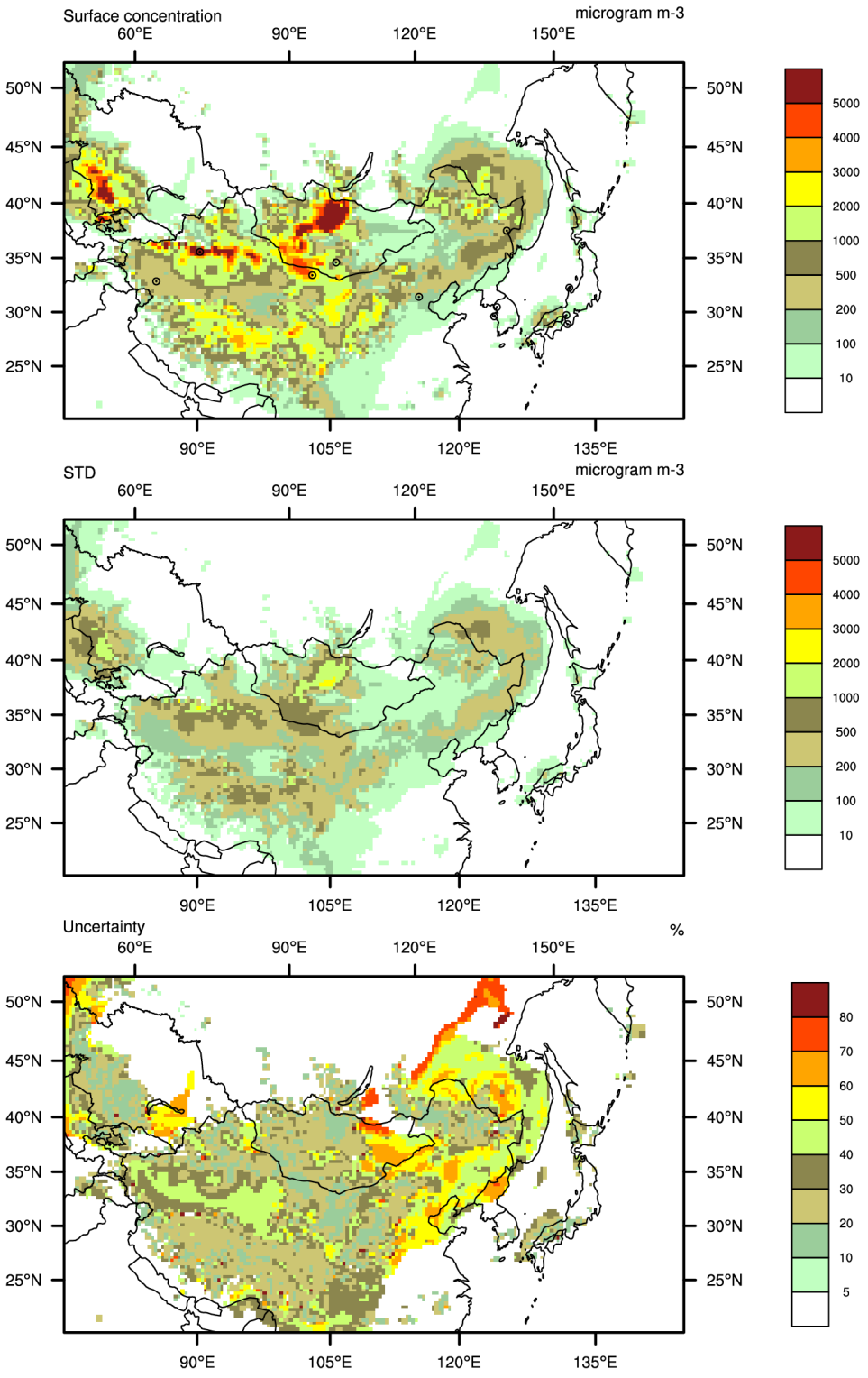

Figure 19: Dust concentration in the first model layer on 8 April 2001, 3UTC. Shown are the median value of the 27 modeling experiments (top), standard deviation (middle) and uncertainty (bottom).

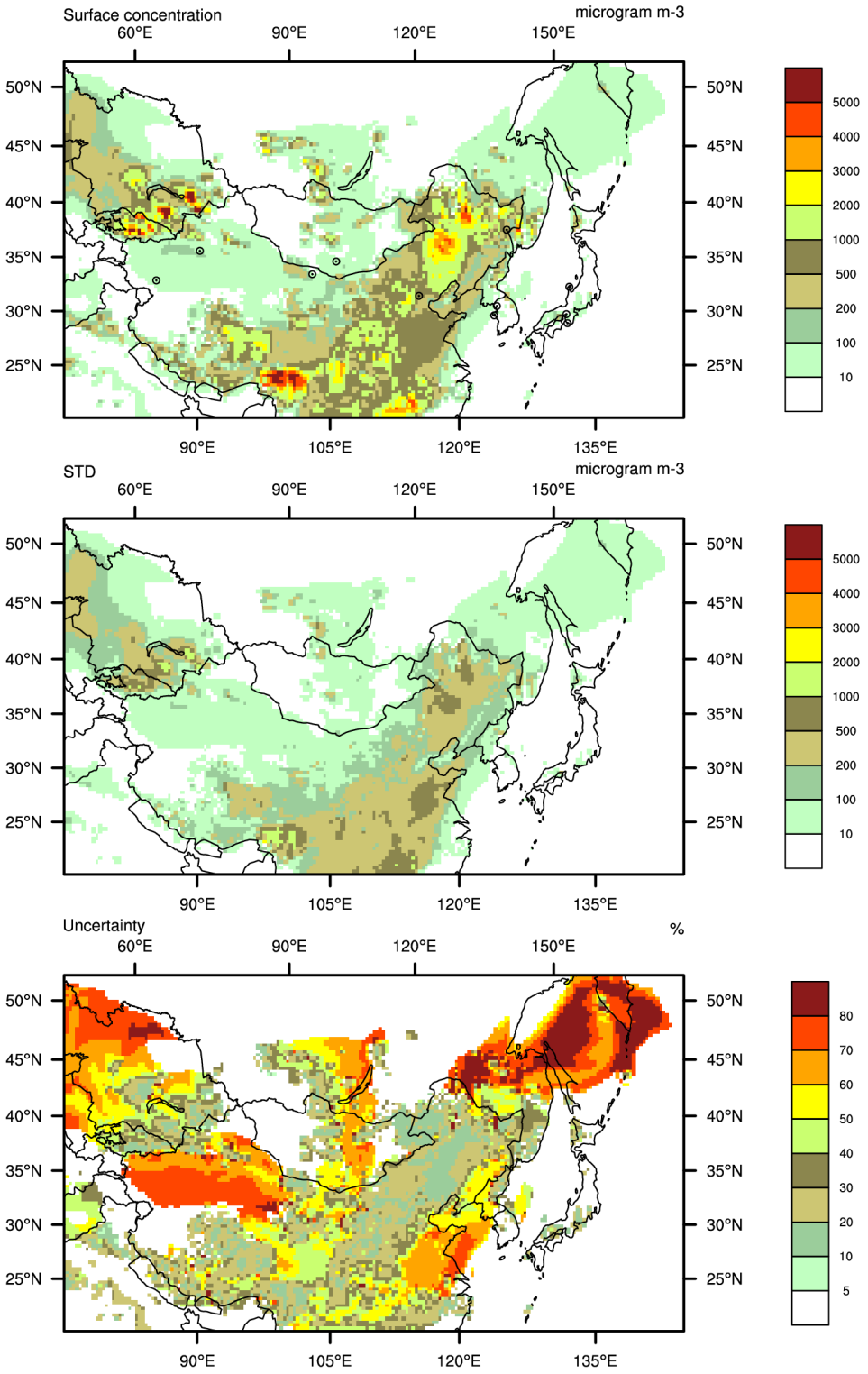

Figure 20: Same as Figure 19, except for 10 April 2001, 3 UTC.

The highest standard deviation values are observed in the lowest parts of the dust plume where the concentrations are the largest. In contrast, the scatter ratios have highest values at the upper portions of the dust plume. Figure 22 shows that on 10 April the dust plume was transported over the Sea of Japan and reached height up to 8 km, which is in agreement with observations from the ACE-Asia experiment [*Gong et al.*, 2003; *Satake et al.*, 2004].

Figures 23 and 24 show the dust optical thickness (DOT), its standard deviation and scatter ratios for 8 and 10 April, 2001 (3UTC). On 8 April large DOTs are observed over the Taklamakan and Gobi. The largest differences between the experiments and the largest scatter ratios are observed over Taklamakan and in the clearly visible cyclone vortex. On 10 April, the dust plume reached Japan, showing a very uniform distribution over the ocean that extends from 25°N to 45°N. One can also see an increase in the modeled DOTs uncertainties from 8 to 10 April, which is an evidence that the experiments diverge from each other as time progresses.

Figure 25 shows the instantaneous dust deposition flux on 8 April, 2001 at 03 UTC. The top, middle and bottom panel represent the median value for the 27 experiments, standard deviation and scatter ratios (uncertainty), respectively. Localized small pockets of increased deposition fluxes can be seen over the entire domain, indicating the sporadic nature of dust events. It is expected that the patchy emission will result in patchy deposition patterns over source regions. Larger differences between the experiments are observed over the Tibetan Plateau and between the border of Chinese and Mongolian Gobi. Figure 26 shows instantaneous deposition fluxes on 10 April, 2001 at 3 UTC which is a time snapshot at the end of the dust storm. Deposition fluxes are increased over Northeast China, Southeast China and the Loess Plateau. There is very weak deposition over the source regions indicating low concentration of dust at the surface, because the dust plume was transported downwind and the sources do not provide freshly emitted dust particles at this time.

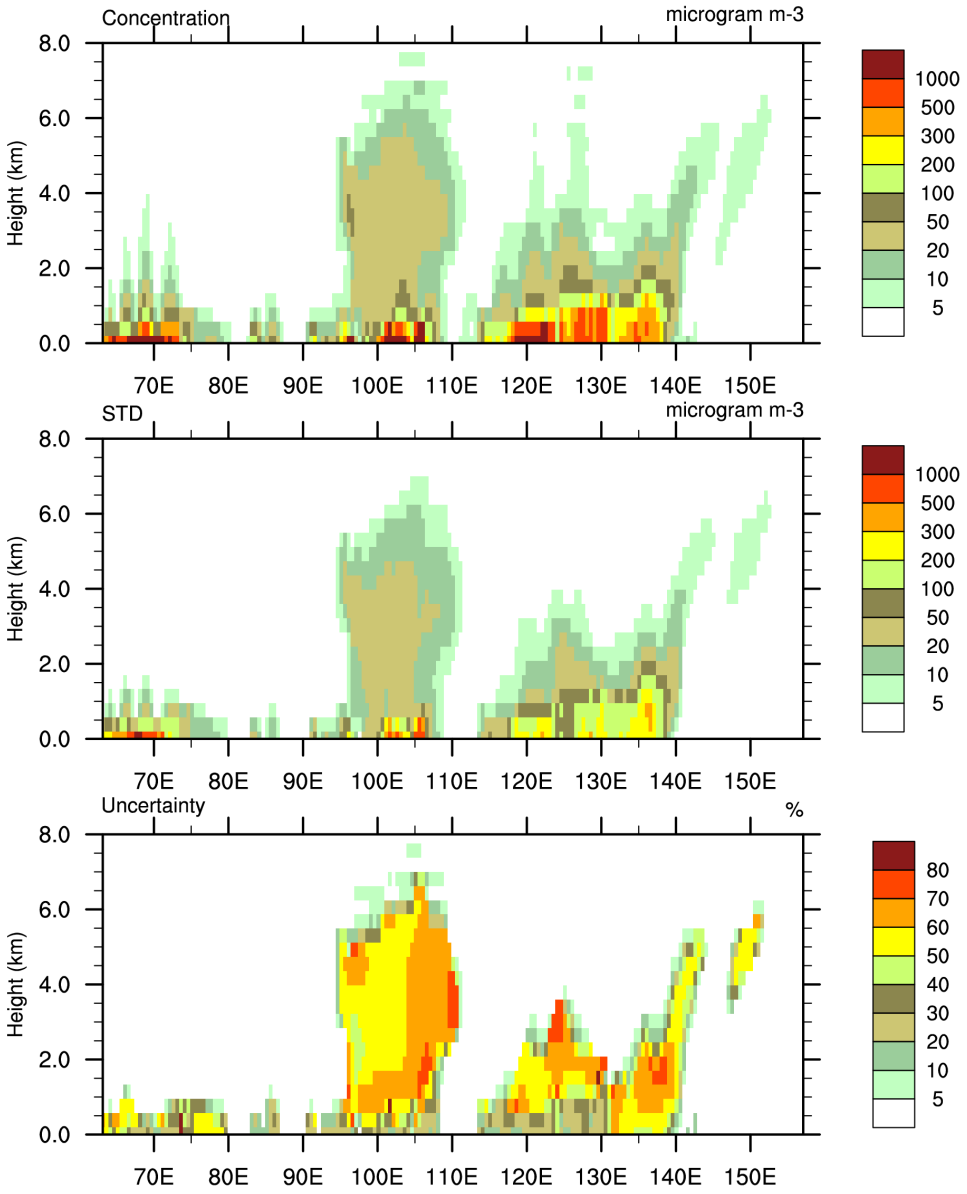

Figure 21: Latitudinal cross section at 40.5°N of dust concentration on 8 April 2001, 3UTC. Shown are the median value of the 27 experiments (top), standard deviation (middle) and uncertainty (bottom).

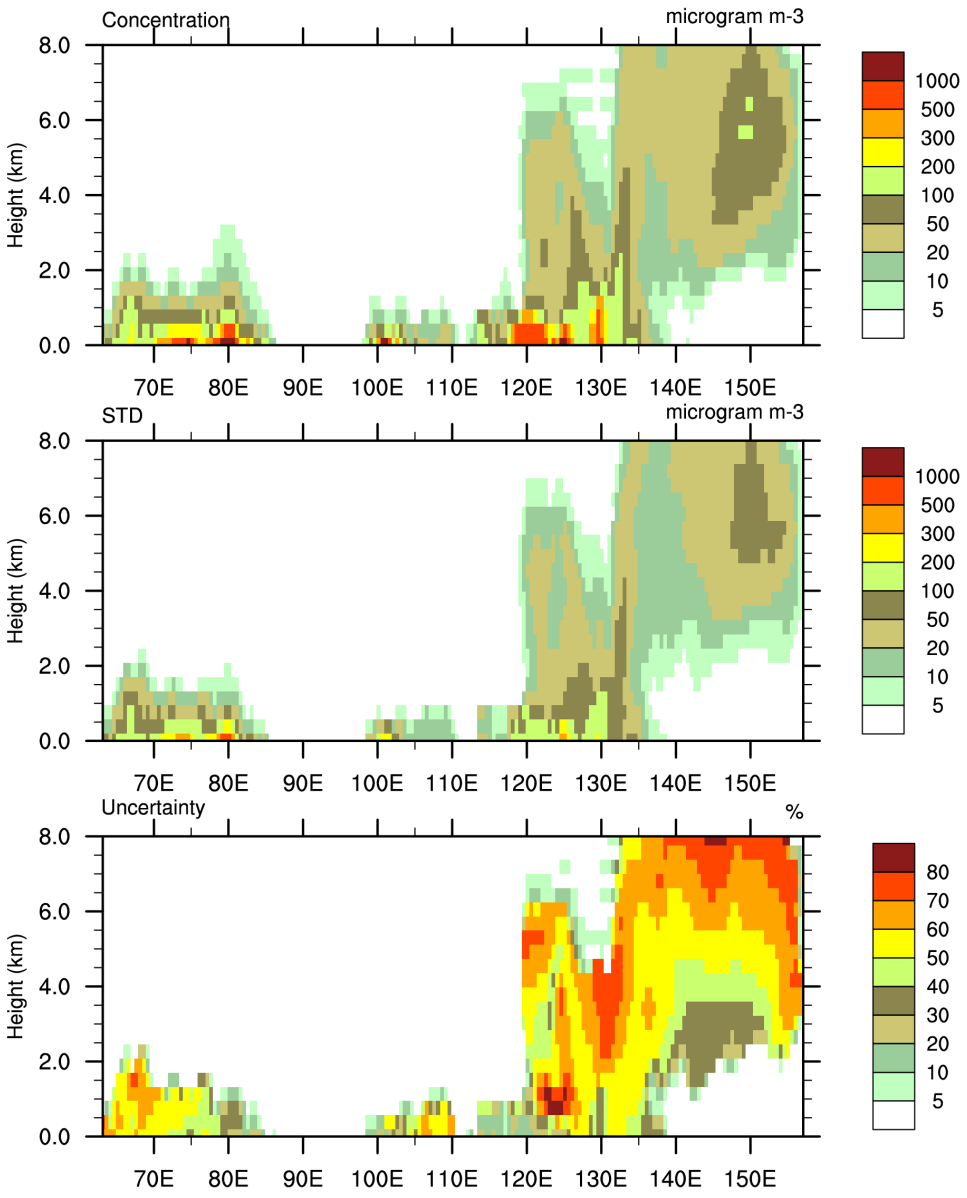

Figure 22: Same as Figure 21, except for 10 April 2001, 3 UTC.

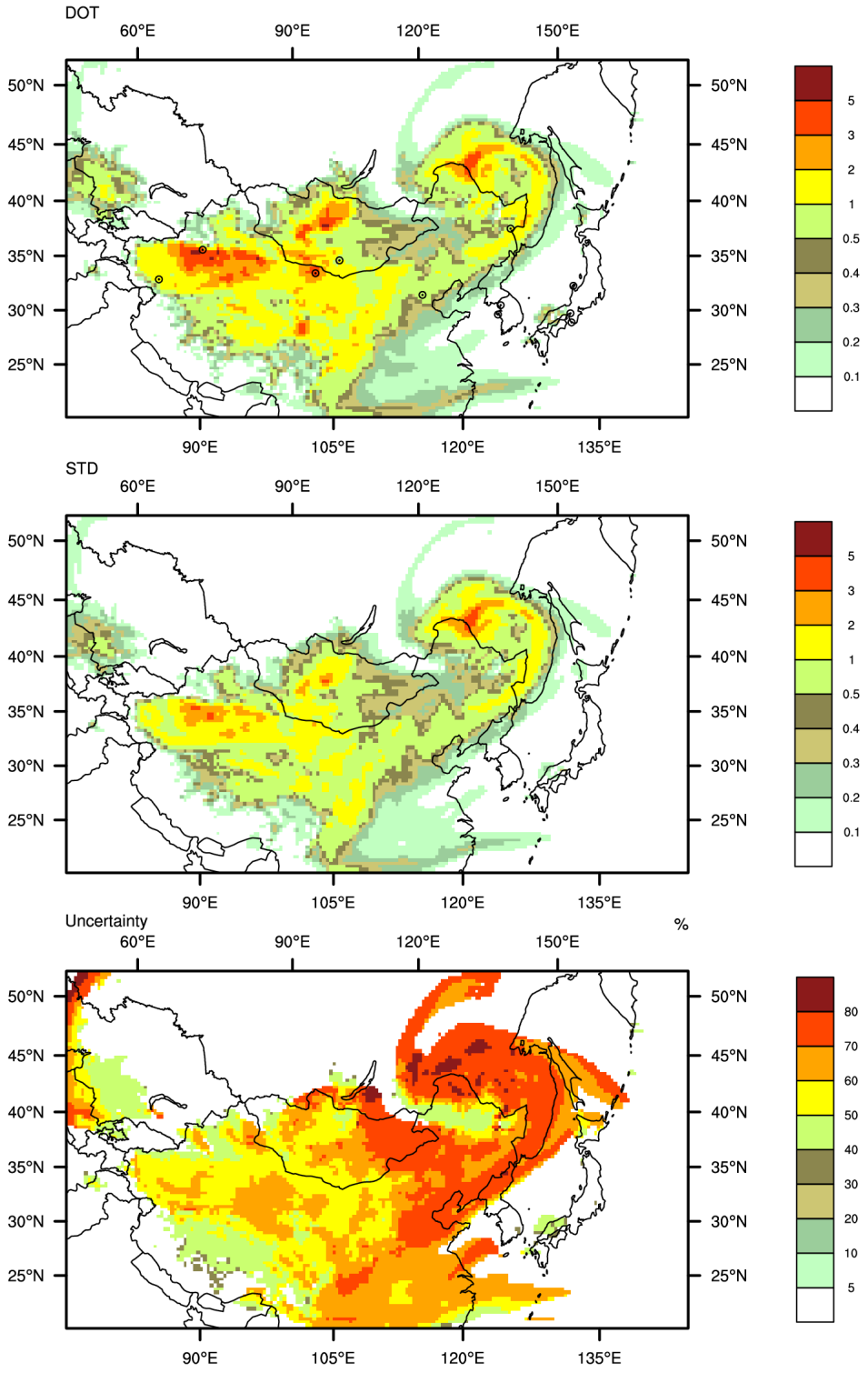

Figure 23: Dust optical thickness on 8 April 2001, 3UTC. Shown are the median value of the 27 modeling experiments (top), standard deviation (middle) and uncertainty (bottom).

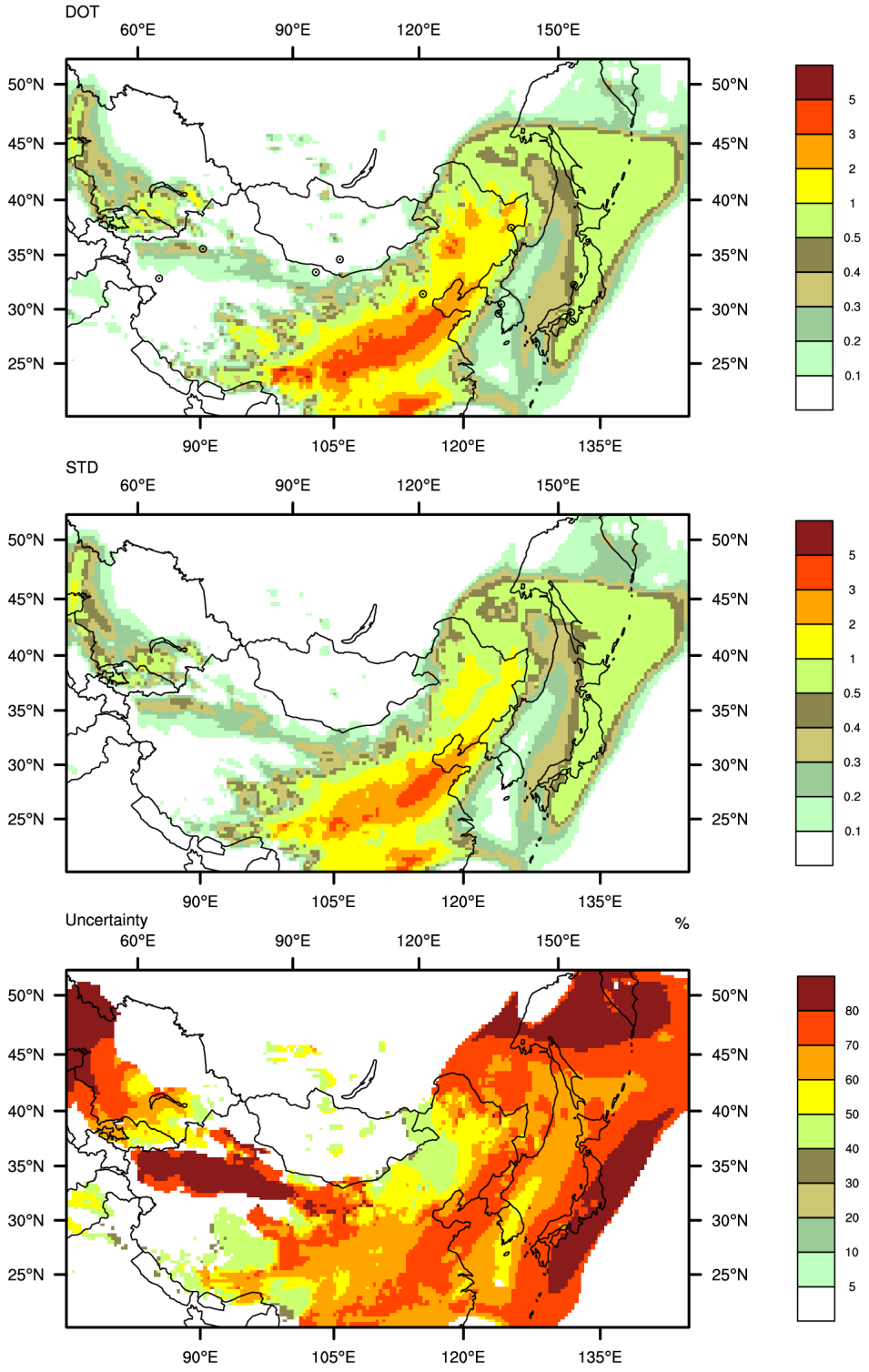

Figure 24: Same as Figure 23, except for 10 April 2001, 3 UTC.

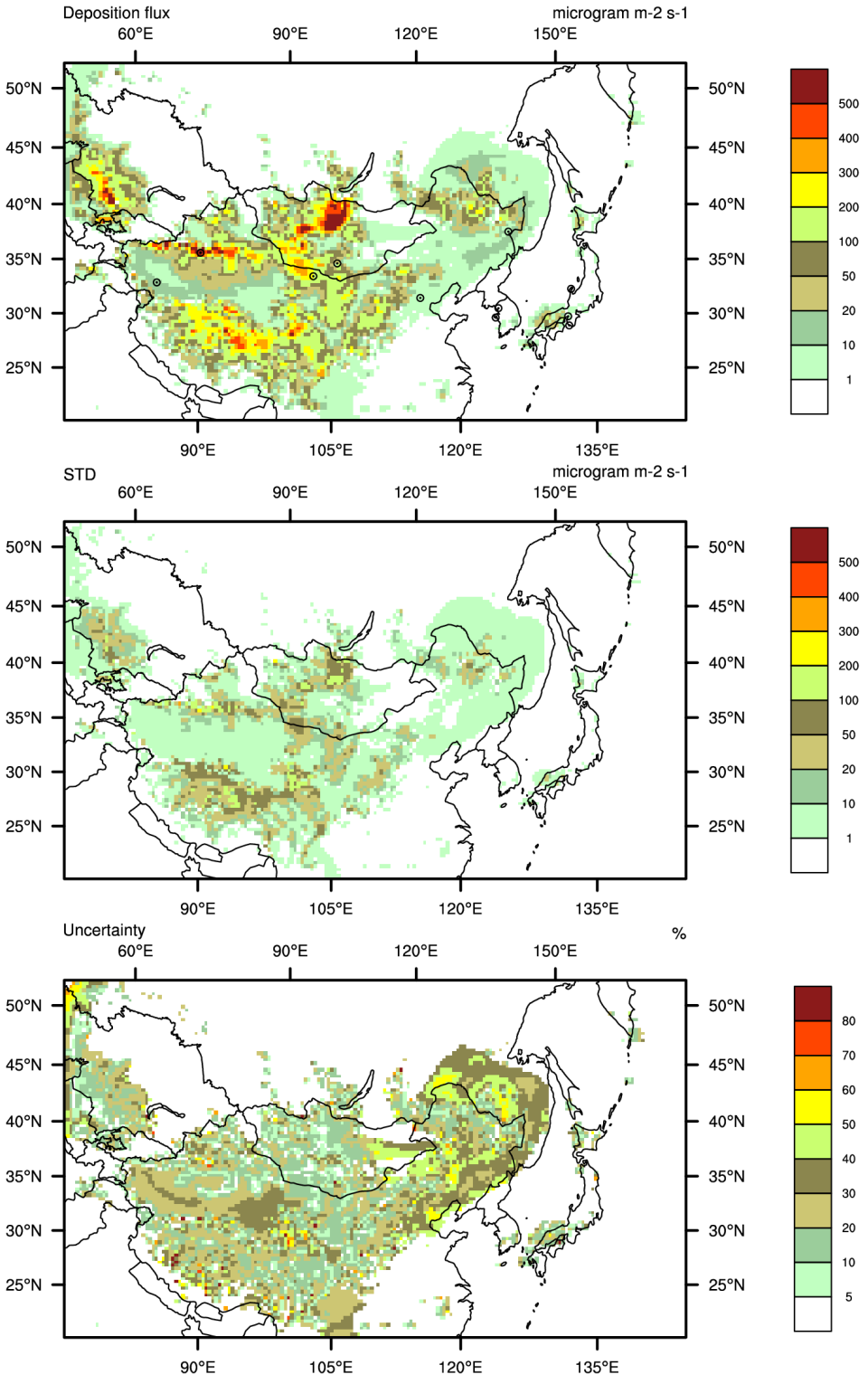

Figure 25: Dust deposition flux on 8 April 2001, 3UTC. Shown are the median value of the 27 modeling experiments (top), standard deviation (middle) and uncertainty (bottom).

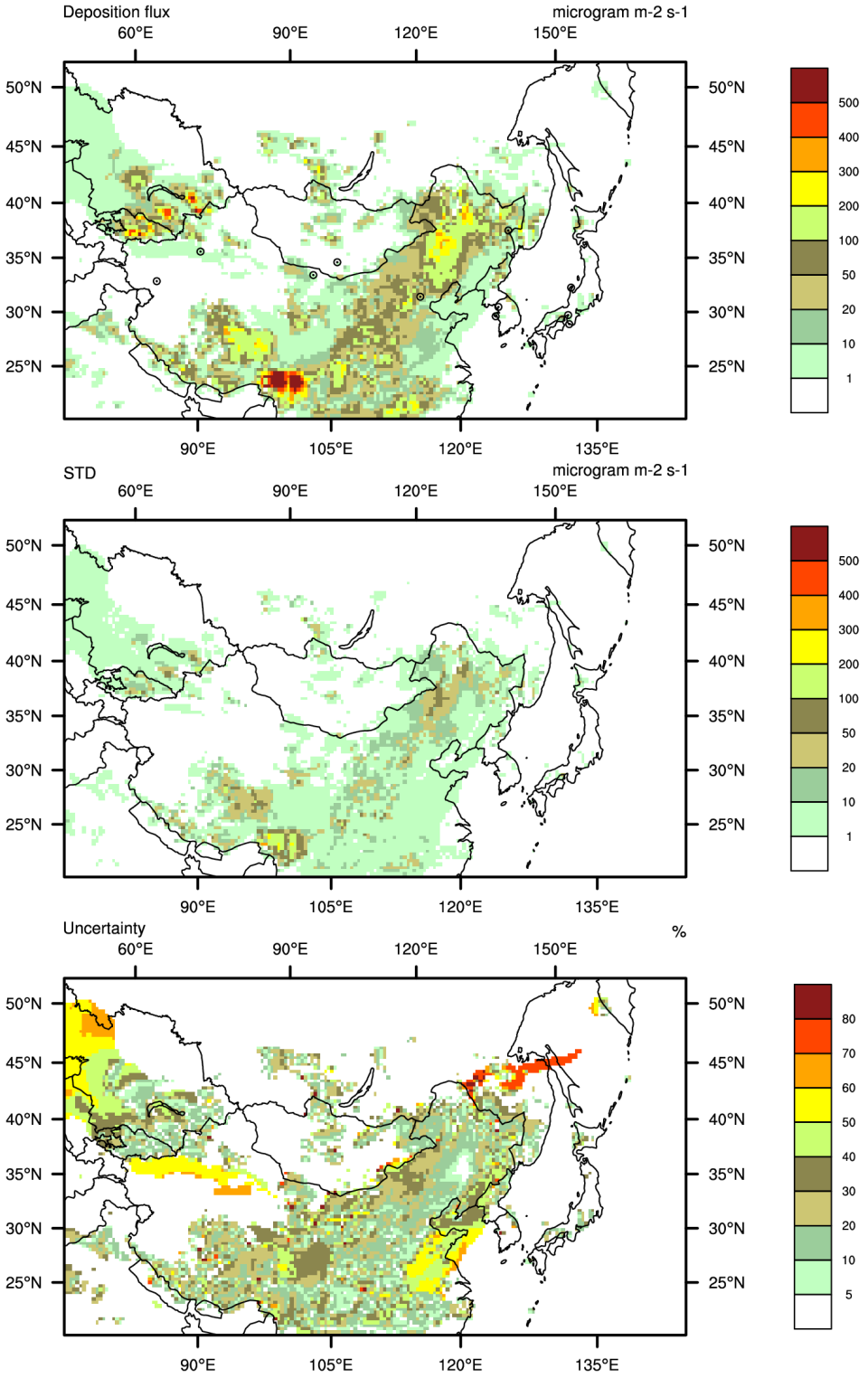

Figure 26: Same as Figure 25, except for 10 April 2001, 3 UTC.

We performed an extensive analysis of the modeled MMD, dust optical thickness, visibility, 3D concentration fields and deposition fluxes during the Spring 2001 dust event which is representative for the region of East Asia. Our sensitivity analysis and detailed intercomparison revealed that the injection schemes affect the modeled dust fields to a lesser degree compared to the initial size distribution. The weak dependence on the injection schemes might be a result of underestimation of the PBL height over the source regions and/or efficient mixing of dust by the WRF PBL scheme. Our results indicate that the 'exponential' in PBL injection scheme might be a reasonable choice between the '1st layer' and the homogeneous in PBL injection schemes. The statistical variables (standard deviation and scatter ratio) derived from our ensemble run facilitated the identification of the modeled dust fields uncertainties due to initial size distributions and injections. We found large uncertainties along the periphery of the advancing dust plume which is likely due to propagating in-time differences between the members of the ensemble. For the first time we were able to demonstrate that the combination of selected initial size distribution and injection can contribute to large variability in the modeled fields. This finding is especially relevant in case of model intercomparison studies and is a possible source of uncertainty that needs to be explored further by the dust modeling community.

2.5 Conclusions

A new state-of-the-art dust regional modeling system WRF-DuMo was developed and used to investigate the effect of initial size distribution and injection height on the spatiotemporal distribution of atmospheric dust aerosols. WRF-DuMo consists of three components: (1) a meteorological modeling system for the description of atmospheric states and motions, (2) terrestrial preprocessor and dust module for emission, injection and optics, and (3) dust transport-deposition module for simulation of the atmospheric dust evolution.

A significant advantage of WRF-DuMo compared to other existing dust regional models is that a suite of simple and physically-based dust emission schemes were incorporated

into the dust module. Having dust emission schemes of different complexity implemented into WRF-DuMo enables to bracket the uncertainties in dust modeled fields and assess the relative importance of involved processes and parameters. In addition, the newly developed terrestrial preprocessor provides a set of aeolian scale land surface input parameters required in the physically based emission schemes in contrast to the commonly used regional scale default land surface characteristics. Also, in contrast to other regional models, WRF-DuMo offers flexibility in setting the initial dust emission size distributions, which can be beneficial for dust modeling in different geographical regions. The initial injection schemes implemented into WRF-DuMo provide a number of representative scenarios for modeling the initial dust injection height. Different injection schemes can also be used under different synoptic conditions causing dust events, i.e., migratory anticyclones versus cyclonic circulations.

The flexible options available in WRF-DuMo enabled us to investigate the effect of initial dust emission size distributions and injection schemes on modeled spatiotemporal dust fields. Our main findings are as follows:

1. Initial size distributions are the main factor that controls the modeled dust particle sizes. The effect of initial sizes is more prominent in and near dust sources, and it decreases during the mid- and long-range transport. Fine mode diameters show very weak response to changes in the initial weights in dust source regions, which can be explained by the fact that the dry removal rate of fine particles is negligible compared to the emission rate when the sources are active. Initial weights start to play a role far downwind from the sources where their effect becomes comparable to that of the initial size. We also found that the effect of the injection scheme on the modeled dust particle diameters is negligible compared to that of the initial sizes and weights.

2. Variability in the first layer concentration is mainly attributed to the initial size distributions and to a lesser extent to the injection schemes. As expected, the first layer

injection scheme produces the largest concentrations in the first layer, which subsequently leads to larger deposition fluxes.

3. Analysis of column integrated quantities and vertical distribution of the concentrations showed that the main controlling factor is the initial dust size distribution. In contrast to the concentration in the first layer, column integrated fields show very weak dependence on the injection scheme.

4. We found that the largest uncertainty in dust concentrations, dust optical thickness, column integrated mass and deposition rates are observed on the periphery of the dust plume. This is most likely due to the propagating in time differences between the experiments.

Our numerical experiments show large variability in the modeled dust fields (for instance, an order of magnitude difference in the simulated DOT) in response to changes of ±30% in the initial MMDs and weights. Based on our extensive modeling experiments, we found that the initial size distributions are of great importance to the modeling of dust fields. Injection schemes influence dust patterns to a lesser extent. Nonetheless, there are some advantages in using the exponential injection scheme, which is a hybrid between the first layer and the homogeneous injection schemes, and often produces results in between the latter two. The strong sensitivity to initial size distribution dictates the need for accurate measurements and modeling of size resolved dust emission fluxes. As a result, we recommend that future dust modeling systems need to develop and include an external data set with initial size distribution of dust particles. In addition, we also recommend the use of ensemble forecast approach in order to estimate the modeled dust fields uncertainties.

CHAPTER III

CHARACTERIZATION OF ATMOSPHERIC MINERAL DUST WITH GROUND- AND SPACE-BORNE MEASUREMENTS

3.1 Introduction

One of the outstanding issues in dust studies is the quantification of spatial and temporal variability of the burden and properties of atmospheric dust at all relevant scales. Regional and global aerosol transport models commonly used for quantification of the dust life cycle produce significant range of uncertainties in quantification of dust fields. Some of the existing uncertainties can be eliminated when numerical models are validated against observational data. While no single measurement is sufficient to fully characterize dust in the atmosphere, integration of various observations will help to better identify the presence of dust in the atmosphere and to characterize dust properties.

The goal of this chapter is to examine the capability of ground-based and satellite observations to detect and characterize dust in the atmosphere, focusing on the regional signature of dust. Section 3.2 discuses ground-based observations that are used to characterize dust and its presence in the atmosphere. Section 3.3 discusses commonly used satellite dust products. In Section 3.4 we discuss existing techniques for dust detection and discrimination from clouds and outline some of their deficiencies. In addition, we use MODIS data to identify the regional thermal-IR radiative signature of mineral dust and to develop a statistical approach for discrimination of mineral aerosols from clouds using spatial variability of satellite visible radiances. Section 3.5 summarizes our main findings.

3.2 Ground based observations

3.2.1 Visibility

Visibility is a measure of the opacity of the atmosphere. Low visibility can be caused by heavy precipitation, fog, snow, smoke and blowing sand. It can be derived either manually or from automated visibility sensors. To determine horizontal visibility, most automated systems use sensors that rely on the extinction of light by atmospheric particles within a small sampling volume. If visibility is uniform and the sampled volume of air is representative of a large area, this method generally produces acceptable results. However, ff those conditions do not prevail the sensor value may significantly differ from the true value. Despite the variety of visibility sensors that have been developed over the years, the majority of the meteorological stations still report manually derived visibility. Manually derived visibility value is obtained using the "prevailing visibility", which is the greatest distance that can be seen throughout at least half the horizon circle. One immediate disadvantage of detecting dust presence trough visibility is the discrete nature of manually derived visibility, which involves visual determination of a distance to a target. Usually visibility is reported in ranges (below 1 km, between 1 and 10 km, and above 10 km).

Visibility data have been commonly used for classification of dust events because they provide a good qualitative assessment of the spatial and temporal distribution of dust outbreaks [*Goudie and Middleton*, 1992; *Sun et al.*, 2001; *Darmenova et al.*, 2005]. To illustrate the use of visibility data, Figure 27 shows the midrange transport route reconstructed for the case of the "Perfect dust storm" originating on 8–11 April 2001. Visibility measurements at 0000 UTC, 0600 UTC, 1200 UTC and 1800 UTC are shown, and regions with visibility less than 1 km are marked by dark gray shading, whereas regions with visibility below 5 km are shown in light gray shading. The evolution and transport of this particular dust plume can be easily observed. The dust storm that started earlier on 7 April was transported to the southeast-east. Another storm in the Taklamakan Desert started to develop around 0600 UTC on the previous day and the plume was transported to the east on

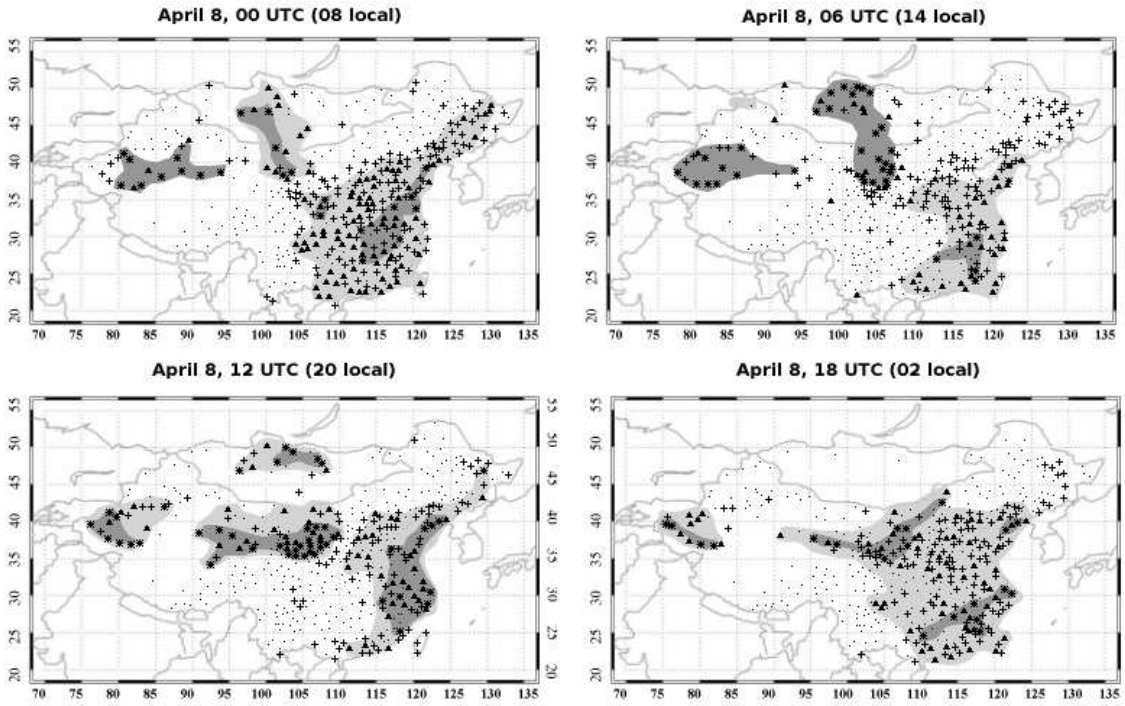

Figure 27: Midrange transport route of a dust storm that originated over the Gobi Desert on 8 April, 2001 based on visibility measurements at 0000 UTC, 0600 UTC, 1200 UTC, and 1800 UTC. Dark gray shading shows visibility less than 1 km, whereas light gray shading shows visibility less than 5 km. (source: *Darmenova et al.* [2005])

8 April.

Furthermore visibility data can be used to identify the duration and intensity of individual dust episodes. Figure 28 shows the time series from five stations located in the Taklamakan area. The horizontal arrows show the dust events identified over the entire Taklamakan region, while the curves represent the visibility evolution with time. The figure illustrates that the duration of dust events recorded at a single station differs significantly from the averaged duration (horizontal arrows) based on the readings from all stations in the Taklamakan.

A disadvantage of the visibility measurements is the fact that low visibility may be caused not only by dust events, but also due to urban pollution episodes, haze/fog and biomass burning. In general, dust source regions are located far away from big cities and

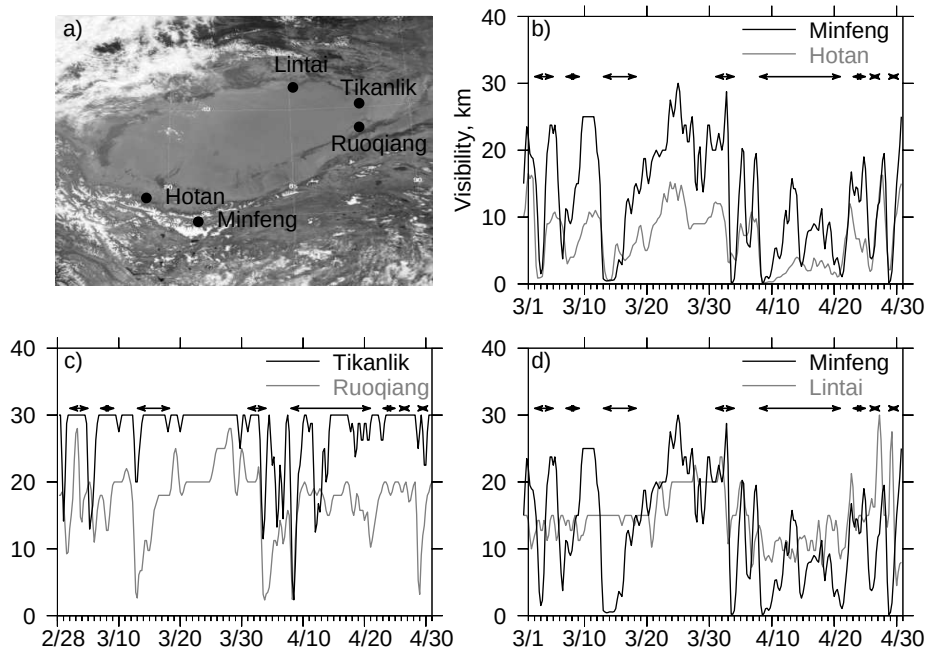

Figure 28: Visibility time series for five Chinese stations located in the Taklamakan desert. The arrows show the dust events identified over the entire Taklamakan region. (source: *Darmenova et al.* [2005])

dust storm plumes can rarely be confused with urban pollution. To avoid misclassification of dust events some studies use additional data on dust weather type (when reported) and precipitation/relative humidity records. The latter provide information for low visibility due to rain and fog.

In addition to visibility, meteorological parameters such as wind speed, precipitation and temperature have been widely used for analysis of the spatiotemporal distribution of dust. Usually a combination of temperature anomalies, wind speeds, dust weather type and cyclone frequency is being adopted for calculation of the so called "dust index" [*Qian et al.*, 2001]. Dust index is a qualitative characteristics that gives idea about the preferential distribution of dust storms in the source regions.

3.2.2 Particular matter concentration

Particular Matter (PM) measurements can provide an insight about transport routes, mineralogy and aging of soil-derived particles. Close to dust sources PM consist mainly of dust

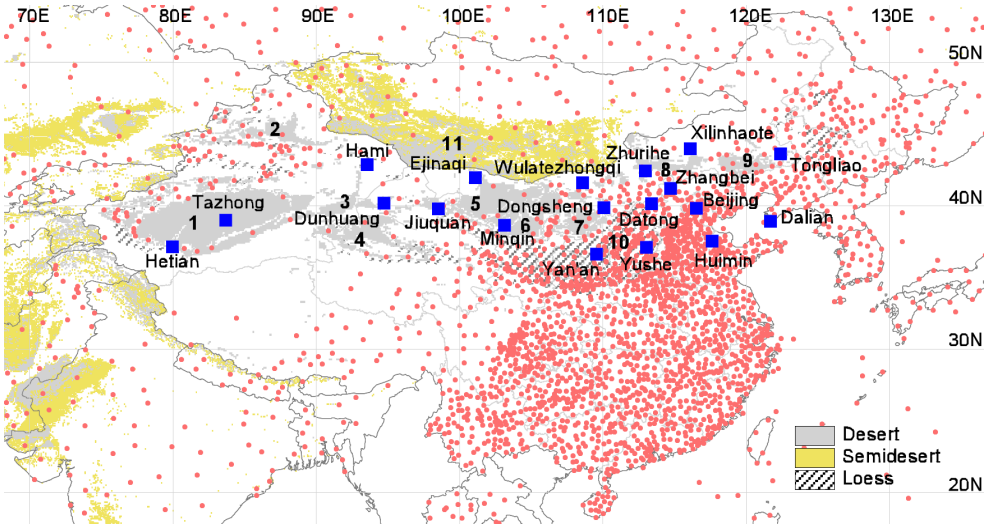

Figure 29: The distribution map of the PM_{10} stations used for observation of sand and dust storms by the China Meteorological Administration. The red dots are weather stations while the blue squares are sand and dust storms observation stations. (source: *Wang et al.* [2008])

particles, however downwind PM may consists of a complex mixture of different types of primary and secondary aerosol particles. Particles of 10 μm or less in diameter (PM_{10}) and particles less than 2.5 μm in diameter ($PM_{2.5}$) measured during dust events have been used for validation and comparison with model predicted dust concentrations [*Liu et al.*, 2003; *Gong and Zhang*, 2008; *Hu et al.*, 2008]. Figure 29 shows the geographical distribution of the stations used for the observation of dust storms in China. Nineteen stations with PM_{10} observations are located in dust sources and downwind regions in northern China. The PM_{10} mass concentrations are recorded continuously and averaged over 5 min periods in each station. *Wang et al.* [2008] found a good correlation between PM_{10} and visibility especially during dust episodes in the source regions.

3.2.3 Ground-based remote sensing

Sun photometer measurements of the direct solar radiation are commonly used to retrieve the aerosol optical thickness (AOT). For example, the NASA AERONET photometer

Figure 30: Distribution map of AERONET stations in East Asia.

robotic network reports fine mode and coarse mode spectral AOT from 532 stations worldwide. However, only few of these stations are located in or near dust source regions. In East Asia, out of 63 stations only 9 are located in the vicinity of major deserts (see Figure 30). AOT can be measured with sun photometers only for cloud-free sky conditions. Since most of the dust events are associated with significant cloud cover along frontal systems, the detection of dust plumes can be obstructed by the presence of clouds.

Figure 31 shows the AERONET AOT measured at Dalanzadgad and Beijing during 5–11 April 2001. The measurements are very intermittent and comparison with modeled AOT (see Figures 17 and 18) can be challenging. However, the measured AOT in Beijing exceeds 3 on 8 April and 2 on 10 April indicating elevated presence of particulate matter.

Lidars have been successfully used for tracing mid- and long-range transport of dust. Two major ground-based lidar networks exist - The Japanese National Institute for Environmental Studies (NIES) lidar network (13 lidar systems) and the European Lidar Network (EARLINET) consisting of 24 active lidar stations located in 12 countries. The instruments are continuous polarization Mie-scattering lidar systems and the aerosol extinction

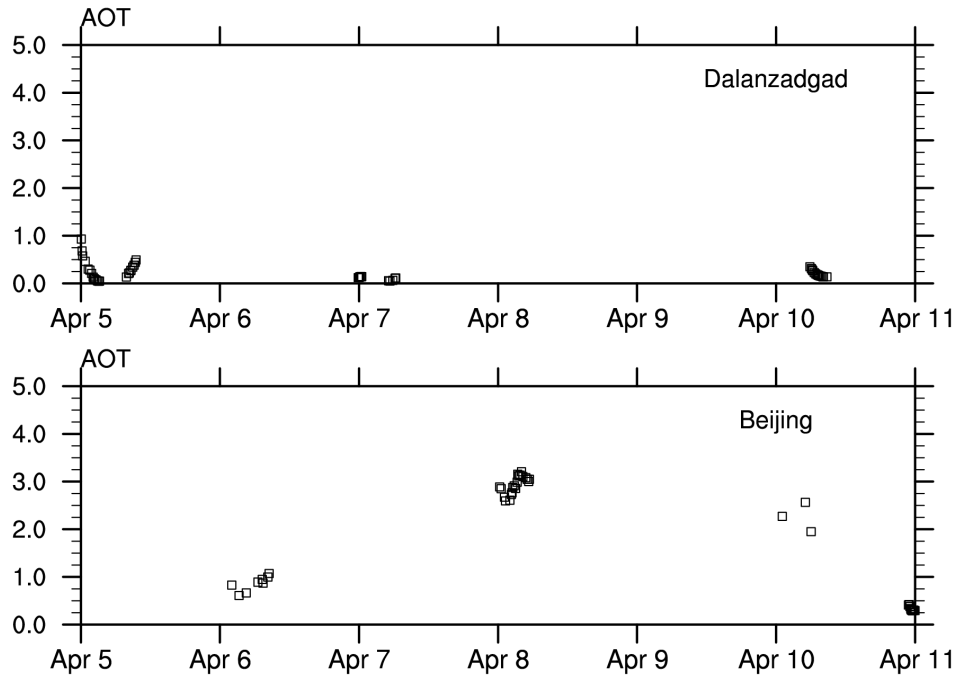

Figure 31: Timeseries of AERONET AOT (500 nm) measured at Dalanzadgad (top panel) and Beijing (bottom panel) during 5–11 April 2001.

coefficient is split to dust (nonspherical aerosol) and nondust (spherical aerosols such as air pollution) fractions based on the aerosol depolarization ratio. An example of dust signal at Suwon, South Korea on 31 March – 2 April, 2007 is shown in Figure 32. The increase in the measured depolarization ratio during that period is due to the nonsphericity of the dust particles.

All the above-described ground-based observations are performed at single locations once or several times per day. An obvious limitation of ground-based data is the limited spatial coverage (non existent over oceans) and temporal sampling. Since dust events are relatively short living phenomena it is critical to be able to observe/detect them at higher frequency.

3.3 Examination of satellite observations

During the last decade, remote sensing was proven to be a valuable tool for characterization of dust sources and dust transport [*Husar et al.*, 2001; *Prospero et al.*, 2002]. A

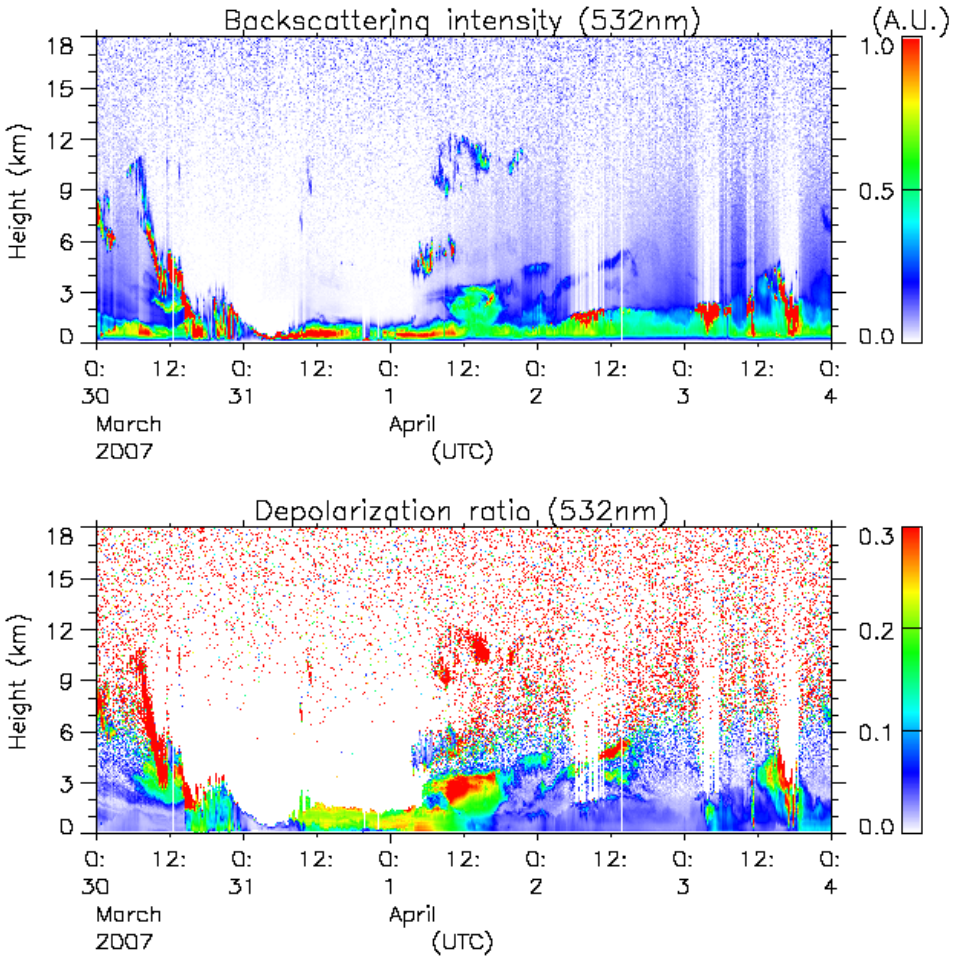

Figure 32: Lidar observations at Suwon (South Korea) during 30 March – 4 April, 2007. Time-height indications of backscattering intensity (top) and depolarization ratio (bottom). (source: Lidar Center of Kyung Hee University, Suwon, South Korea; http://www-lidar.nies.go.jp/Suwon/index.html)

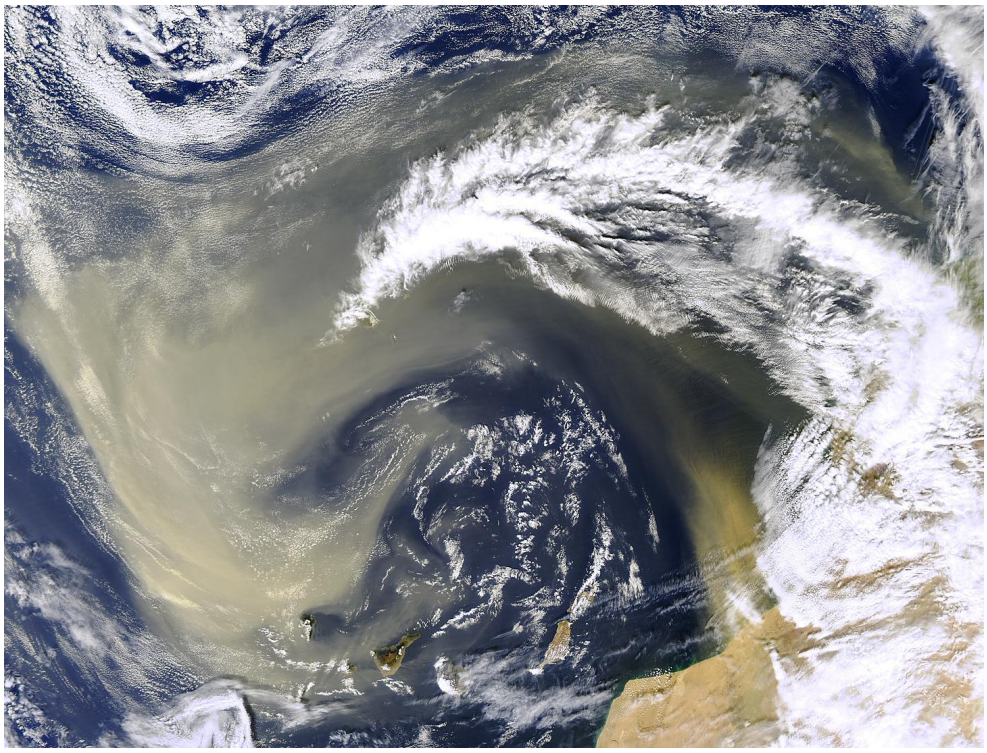

Figure 33: Dust over the Canary Islands (April 2004) as seen from MODIS.

number of geostationary and polar orbiting satellites are currently operational and provide observations that can be used to track dust outbreaks on regional and global scales.

Satellite retrieved AOT has been used extensively in dust studies. The most commonly used AOT datasets include retrievals from AVHRR, MODIS, MISR, TOMS/ OMI and SeaWiFs. A significant advantage of satellite retrieved AOT is the global coverage, which offers valuable information about the spatiotemporal patterns of aerosol, especially over oceans where routine surface measurements are not performed. A common problem with AOT products is that the retrievals are affected by clouds and land surface reflectivity. Depending on the orbit specifics, single location can be tracked continuously every 15 min in the case of geostationary satellites or once or twice a day in the case of Sun-synchronous near-polar orbiting satellites.

If mineral dust is subjected to mid or long range transport it can be observed not only over land but over the oceans as well (Figure 33). Therefore two scenarios for dust detection

need to be considered - over land and over large water bodies. Detection over the oceans is relatively easier compared to the detection over land because of the dark and homogeneous properties of the ocean surface. Over land one needs to account for the highly variable and reflective properties of the surface which to this day remains a formidable problem.

Prior to MODIS becoming operational, satellite measurements were limited to reflectance measurements in one (GOES, METEOSAT) or two (AVHRR) channels. Furthermore, there was no real attempt to retrieve aerosol content over land on a global scale. Algorithms had been developed for use only over dark vegetation. The blue channel on MODIS, not present on AVHRR, offers the possibility to extend the derivation of optical thickness over land to bright surfaces.

In order to separate the total column AOT by aerosol type, MODIS aerosol algorithm assumes that aerosols can be separated into three quasi-independent classes: maritime sea salt, dust, and anthropogenic. To classify aerosol type, the ratio of fine mode AOT to the total AOT at 555 nm, called the fine mode fraction (FMF), is used. Both fine-mode and coarse-mode AOT over the ocean are retrieved from MODIS radiances using a combination of fine-mode and coarse-mode aerosol models with the relative amounts of fine-mode to coarse-mode aerosols adjusted until a solution is found, which minimizes the error in the observed radiance. Fine aerosol particles, such as those produced from anthropogenic sources, predominantly have higher FMF values, while naturally occurring dust and sea salt aerosols with larger particles have predominantly smaller FMF values. The aerosol algorithm requires prior cloud screening.

Another satellite product that is commonly used to detect the presence of dust is the UV absorbing aerosol index, which is a measure of how much the wavelength dependence of backscattered UV radiation from an atmosphere containing aerosols (Mie scattering, Rayleigh scattering, and absorption) differs from that of a pure molecular atmosphere (pure Rayleigh scattering). For instance, the TOMS/OMI AI is retrieved using two channels centered at 0.331 μm and 0.360 μm. These channels are sensitive to aerosols but less sensitive

to absorption by gases. A significant advantage in the retrievals of the aerosol index is the lower surface albedo in the UV. However, the TOMS/OMI AI can be used only as a qualitative tool.

Several other dust indexes were proposed. Legrand et al. [1994] defined an IR difference dust index (IDDI) based on the METEOSAT satellite measurements of IR radiances in the 0.5–12.5 μm wavelength band. Hao and Xu, [2007] proposed a thermal-IR dust index derived from the brightness temperature of MODIS bands 20, 30, 31, and 32.

While AOT and AI are useful for identifying the spatiotemporal patterns of dust, they quantify the dust columnar loadings only. Active remote sensing (e.g., ground-based and space-borne lidars) can provide additional information about the vertical structure of dust plumes [Iwasaka et al., 2006; Winker et al., 2008]. Lidar backscattering coefficient is used for detection of dust since nonspherical dust particles have unique scattering signature. An example of a space-borne lidar is the CALIPSO instrument, which in addition to the backscattering ratios provides also AOD and vertical feature mask product.

Compared to ground-based measurements, satellite observations are better suited for detecting and tracing dust plumes. The aerosol products inferred from satellite data are available at different spatial and temporal scales - ranging from instantaneous observations over the swath to daily and monthly globally averaged quantities. They are also available at wide range of spectral frequencies in UV, visible and IR, thus being able to capture different aspects of dust properties. Satellite products, however, have a myriad of limitations that makes their sole use for dust characterization challenging. Despite the recent progress of dust detection algorithms over land, aerosol products are still prone to quality issues over bright desert surfaces. Cloud contamination is another critical factor that impedes the performance of satellite aerosol products. This is especially relevant for the Central and East Asian dust sources due to generally high cloud coverage in mid latitudes. In addition, polar orbiting satellite revisit the same location within 24–48 hours which is not sufficient given the intermittent nature of dust storms.

Merging surface measurements and satellite data can help to identify the temporal and spatial scales on which the intercomparison between the models and observations would be most efficient. Moreover, observational datasets can complement model simulations to lay out an integrated framework that overcomes the intrinsic limitations of individual datasets.

3.4 Improving detection of dust from passive remote sensing

Accurate detection of the dust signal from satellite observations is the first critical step in characterizing the properties of dust and its transport in the atmosphere. The current detection algorithms employ brightness temperature observations and/or visible radiances. In this section, we evaluate the exiting dust detection techniques (see Table 6) and provide an improved approach for dust detection, focusing on identifying the regional IR signature of dust and characterization of dust-cloud mixed scenes.

Several techniques have been proposed for detecting mineral dust (and volcanic ash) using thermal-infrared observations [*Prata*, 1989; *Ackerman*, 1997; *Legrand et al.*, 2001; *Prata and Grant*, 2001]. The detection techniques are based on brightness temperature differences (BTD) either in two or three channels. The former is called bispectral split-window technique and the latter is trispectral approach. Although the split-window techniques that use observations near the 11 and 12 μm bands have been primarily applied to volcanic aerosols, they have also been used for the detection of dust. For instance, *Dunion and Velden* [2004] relied on this technique to investigate how atmospheric dust affects Atlantic tropical cyclone activity. *Ackerman* [1997] argued that a combination of three IR channels near the 8, 11, and 12 μm bands, i.e. a trispectral approach, is likely to provide more robust dust detection. Using AVHRR and HIRS/2 satellite observations of dust outbreaks over the Arabian Peninsula and adjacent Arabian Sea in July 1985, *Ackerman* [1997] demonstrated that analyzing brightness temperature differences between the 8 and 11 μm channels against BTD between the 11 and 12 μm channels enables to discriminate

dust from clear sky over both oceans and lands. The Ackerman study implied that a universal threshold in the BTD values could be used to detect dust over diverse geographical regions. However, mounting evidence suggests that the properties of dust strongly vary between dust sources. In particular, the mineralogical composition, which is a key factor controlling the IR radiative properties of dust, exhibits strong regional differences [*Claquin et al.*, 1999; *Caquineau et al.*, 2002]. Considering several representative mineral mixtures, a modeling study by *Sokolik* [2002] showed that differences in the composition, especially differences in the amount of clays and quartz, have a large impact on the spectral brightness temperatures.

Given the lack of dust composition data as well as the number of critical assumptions involved in the IR radiative transfer modeling, finding observational evidence of the regional radiative signature of atmospheric dust would be of great importance. This served as a motivation to investigate the thermal-IR radiative signature of atmospheric dust originating from the main world's dust production regions and explore the implications to the dust detection over oceans with the techniques based on brightness temperature differences by using data from the Moderate Resolution Imaging Spectroradiometer (MODIS) on the Terra satellite over oceans.

MODIS cloud-aerosol mask exploits the higher spatial homogeneity of the aerosol plumes compared to those of clouds, plus some additional tests in IR to improve the performance in the case of well developed clouds [*Martins et al.*, 2002]. As a measurement of the homogeneity, standard deviation (STD) of 3×3 1 km pixel reflectances at 555 nm is used. The algorithm does not distinguish different types of aerosols, and as a consequence the same fixed STD threshold is applied to discriminate any aerosol type from clouds.

This motivated us to perform a statistical analysis of a large number of dusty, cloudy and mixed dust-cloud pixels that was performed by using 4-years worth of data from the MODIS visible channels. We analyzed visible radiances by calculating the standard deviation of the 3×3 pixels and the probability distribution function (PDF) of STD. In addition,

Table 6: Existing dust detection techniques - approaches and limitations. None of the existing techniques takes into account the regional specifics of dust.

Study	Instrument	Technique	Dust treatment	Limitations
Ackerman [1997]				Fixed BT threshold Generic dust
	AVHRR	BT differenses; trispectral approach	Yes	
Dunion and Velden [2004]				
	GOES	BT differences	Yes	
Evan et al. [2006b]				
	AVHRR	BT differences	Yes	
Miller [2003]				
	MODIS	Combination of VIS and IR	Yes	
Martins et al. [2002]				Same fixed threshold for all aerosols
	MODIS	Spatial variability of VIS radiances	No	

we tested a local inhomogeneity parameter (LIP) as an alternative to STD. Based on this analysis we tested two statistical methods for discrimination of dust from clouds utilizing the probability distribution functions of STD or LIP. Both methods provide continuous and simultaneous evaluation of a given pixel to be classified as cloud, dust, or mixed dust-cloud types. The performance of these two methods was evaluated against the cloud/aerosol mask based on the fixed STD threshold.

3.4.1 Data and methods

The key to our study was unambiguous selection of dust plumes in order to provide a "truth" in testing the BTD techniques, as well as to study the radiative signature. We were not able to use MODIS aerosol products because of a number of known limitations in the case of dust, especially under heavy dust loads (*MODIS Atmosphere-Known problems* [`http://modis-atmos.gsfc.nasa.gov/MOD04_L2/qa.html`]; *Remer et al.* [2005]; *Darmenova et al.* [2005]). Therefore, our approach was based on a manual scene classification using

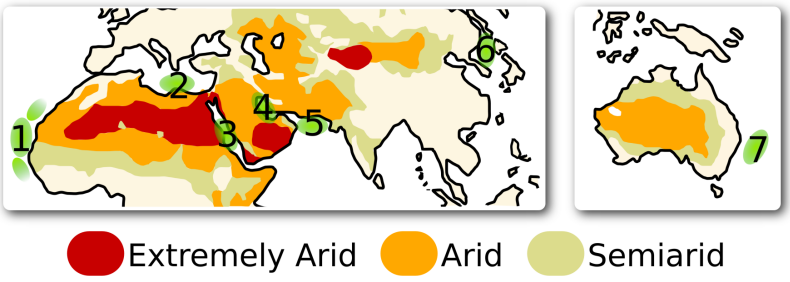

Figure 34: Schematic representation of the geographical regions analyzed in this Chapter.

true color MODIS images. From the 180,000 images accumulated over the entire globe for the period 24 February, 2000 – 30 April, 2004, about 600 images showed dust over oceans. Each image represents a true color composite of a single Level 1B daytime 5-min granule of MODIS data. Figure 34 shows schematically the seven geographical regions considered in this study. For each region, a number of representative cases were chosen for which we obtained the Level 1B data containing calibrated and geolocated at-aperture radiances in 36 spectral bands at 1×1 km resolution. Our final selection consisted of 49 images with unambiguous presence of dust. For each true color image, the pixels were manually classified as "clear", "partly cloudy", "cloudy", "mixed dust and cloud", "dust" and "heavy dust". These categories were represented by 31859, 17345, 24768, 23975, 34961 and 54369 pixels, respectively, totaling 187277 pixels. The large volume of sampled data and the extended length of the time period covered warranted statistical significance of our results.

Figure 34 indicates that the selected regions cover dust outbreaks originating from all main dust sources of the world. In the case of North Africa, we identified three different regions representative of westward, northward, and eastward transport. Dust observed in region 1 is likely to originate from the sources located in Mauritania, Morocco, Algeria, and Bodele Depression, whereas regions 2 and 3 are representative for dust from the Libyan and Nubian deserts, respectively. These sources were described recently by *Prospero et al.* [2002]. A number of studies have pointed out that several distinct sources can contribute

to westward transport (our region 1) [*Chiapello et al.*, 1997]. To address this issue, we sorted dust outbreaks with similar westward transport into three latitudinal groups based on their location off the west coast of North Africa: 8°–16°N, 16°–24°N, and 24°–28°N. Dust plumes in the first group most likely originate from Algeria and Bodele Depression, while dust plumes in 16°–24°N and 24°–28°N latitudinal bands originate from Algeria and Mauritania, respectively [*Chiapello et al.*, 1997; *Prospero et al.*, 2002]. Selecting cases with similar transport routes of dust also helps to minimize differences introduced by varying atmospheric conditions. Regions 4 and 5 represent dust outbreaks originating from the Iranian and Thar deserts, whereas region 6 represents dust plumes that likely originated from the Gobi and Taklamakan regions [*Darmenova et al.*, 2005]. Region 7 represents dust from the Australian deserts. We were able to identify only three cases for this source, and all of them were associated with eastward transport. We were not able to identify significant dust outbreaks originating from the American sources, such as Patagonia and Baja. It is likely that dust plumes from those deserts were not transported over the ocean or were too weak for detection by satellite imagery.

3.4.2 Identifying the regional thermal-IR radiative signature of mineral dust with MODIS

Here we used data from MODIS 29, 31, and 32 channels with central wavelengths of 8.55, 11.03, and 12.02 μm, respectively. Brightness temperatures (BT) for each channel were calculated from the Level 1B radiances by inverting the Planck function in the wavelength domain. Then the BTD between channels 29 and 31 ($BT_8 - BT_{11}$) and channels 31 and 32 ($BT_{11} - BT_{12}$) were computed and analyzed on a case-by-case basis.

First, we examined regional differences of the BTD in the context of the split-window method. As an example, Figure 35 compares two cases of dust outbreaks in region 2 (top panel) and 6 (bottom panel). Shown are the true color images as well as the calculated $BT_{11} - BT_{12}$ and $BT_8 - BT_{11}$ fields. The former is commonly used in the split-window method. In the case of clear sky conditions over oceans, $BT_8 - BT_{11}$ are negative, while

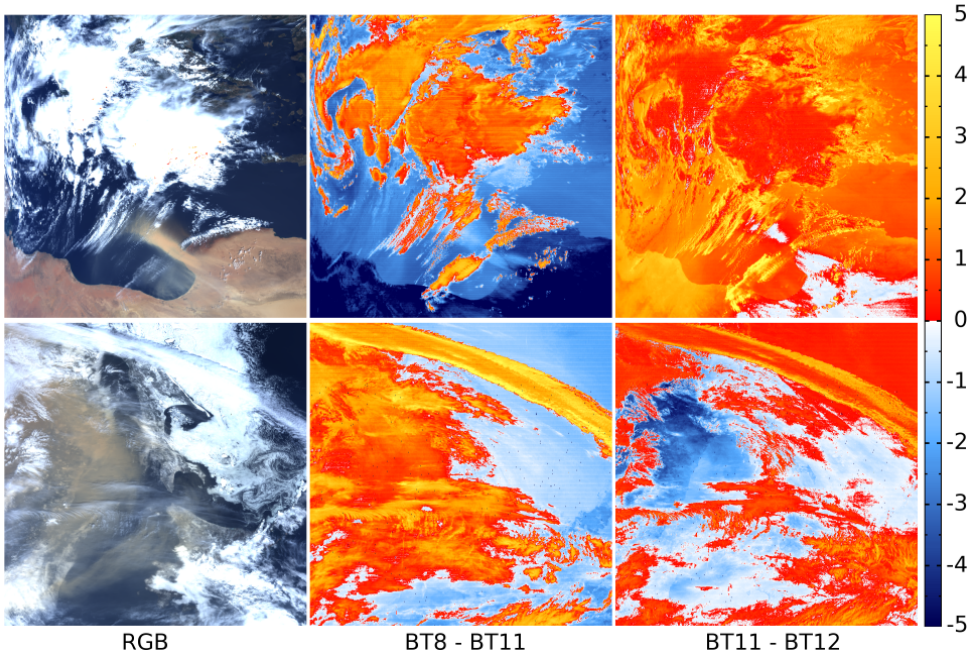

Figure 35: Example of two dust outbreaks in regions 2 (top panel) and 6 (bottom panel). Shown are the true color image, $BT_8 - BT_{11}$ and $BT_{11} - BT_{12}$ differences (in K).

$BT_{11} - BT_{12}$ have positive values in both regions. This behavior of BTD has been already pointed out by previous studies [e.g., *Ackerman et al.*, 1998] and explained by spectral differences in water vapor absorption. Because MODIS 29, 31 and 32 channels lie in the thermal-IR window, absorption by other atmospheric gases is negligibly small. Over the Mediterranean Sea (region 2), $BT_{11} - BT_{12}$ are negative in the presence of dust, while for clear sky and cloudy areas $BT_{11} - BT_{12}$ are positive. Similarly, negative $BT_{11} - BT_{12}$ are caused by Asian dust over the Yellow Sea (region 6). However, negative $BT_{11} - BT_{12}$ are also caused by some clouds in region 6. Over the Mediterranean Sea, $BT_8 - BT_{11}$ for dust are negative and smaller than those for clouds but larger than $BT_8 - BT_{11}$ for clear sky. In contrast, over the Yellow Sea, $BT_8 - BT_{11}$ are positive for dust and for some cloudy areas.

To further address the regional dust radiative signature, a subset of pixels representing different scenes was selected and analyzed. Figure 36 shows the trispectral diagrams for the pixels classified as “heavy dust”, “cloudy” and “clear”. Each data point represents the mean BTD while the error bars show the standard deviation of the mean calculated for the

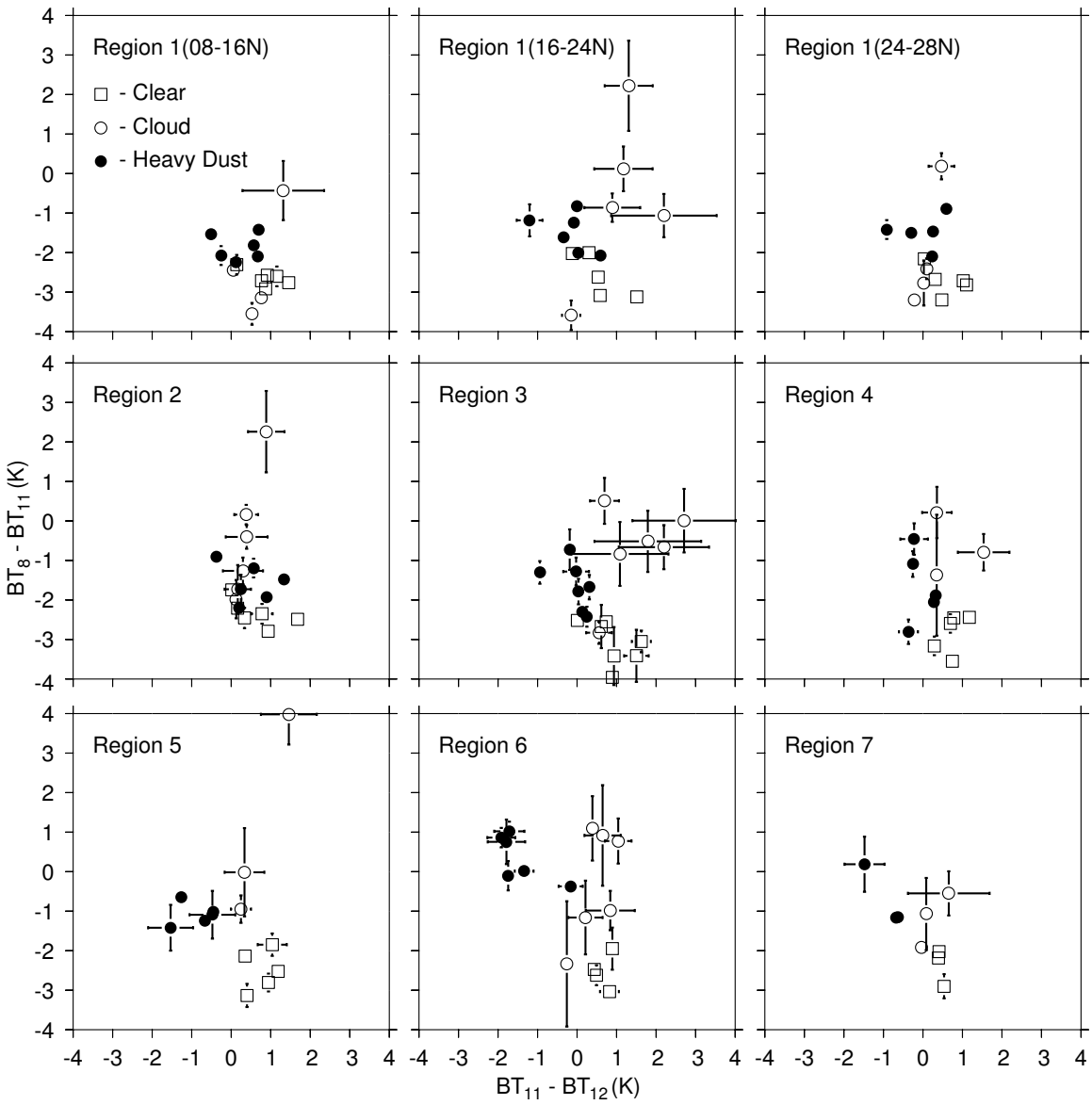

Figure 36: Trispectral diagrams of brightness temperature differences for each region.

selected subset of pixels. Notice that the "clear" data have very similar BTD values and show low variability (i.e., small standard deviation regardless of the geographical region). This implies that the factors controlling BTD variability for clear skies (such as amounts of water vapor, different temperature profiles, variations in the ocean emissivity and temperature, and possibly some sea salt aerosols and/or some thin cirrus missed in the process of classification) cannot be responsible for the large differences observed in "heavy dust" cases between the regions, pointing out that dust itself is a key controlling factor. Nevertheless, the BTD ranges for clear skies apparently differ from those observed in the presence of heavy dust. However, examining Figure 36, one can conclude that discriminating dust from clear sky or clouds may be possible for a single granule by adjusting the BTD threshold, but this is not true in the general case. Regions 1, 2, and 4 pose a particular challenge for discrimination of dust from clouds because of the overlap of "heavy dust" and "cloudy" data points. Although similar overlap is evident for $BT_8 - BT_{11}$ for other regions, there is a good separation in $BT_{11} - BT_{12}$. For example, discrimination between "heavy dust" and "cloudy" pixels would be possible for regions 3, 5, 6, and 7 if one applies $BT_{11} - BT_{12}$ thresholds of 0.5, −0.2, −1.0, and −0.4 K, respectively.

Figure 37 summarizes the mean BTD and standard deviations calculated for "heavy dust" cases along with clear sky cases. The dust BTD values show specific features depending on the particular region. Some of the regions appear to group on the trispectral diagram. Regions 1(16°–24°N), 1(24°–28°N), 3, and 4 form one group with $BT_{11} - BT_{12}$ and $BT_8 - BT_{11}$ values of about −0.1 K and −1.7 K, respectively. Regions 7 and 5 form another group with $BT_{11} - BT_{12}$ of −1.0 K and $BT_8 - BT_{11}$ of −1.1 K. Regions 1(8°–16°N), 2, and 6 differ from the others, showing several distinct features such as positive $BT_{11} - BT_{12}$ in regions 1(8°–16°N) and 2, and positive $BT_8 - BT_{11}$ in region 6. The question arises: Can we isolate the factors that control the infrared signature of atmospheric dust? Differences in the satellite viewing geometry may play a role. However, in our analysis dust pixels were

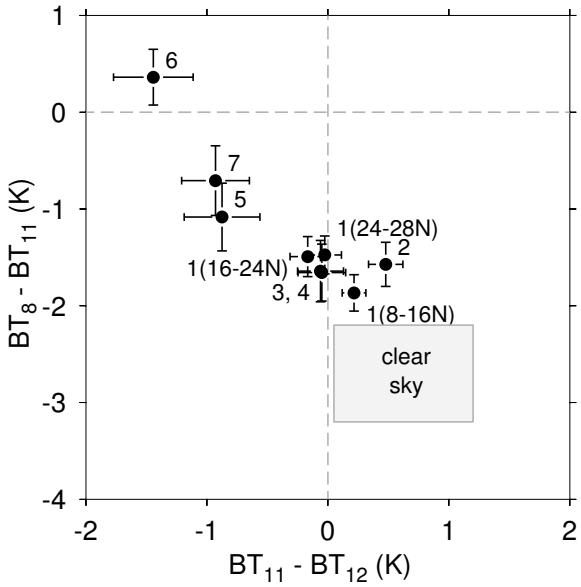

Figure 37: Combined trispectral diagram of brightness temperature differences for "heavy dust" pixels for all considered regions.

sampled at random locations within the granules. Thus for a large enough number of granules the geometry effect might increase the data scatter but should not change the mean. This was also confirmed by analyzing plots similar to the ones shown in Figure 36, but for different cosine of the viewing angle ranging from about 0.6 to 1 in a discrete interval of 0.1. As expected, a shift in data points was observed with changes of the viewing angle, however various regional differences between the BTD points remained.

Furthermore, previous studies showed that the brightness temperature differences are relatively insensitive to changes in the size distribution compared to changes in the mineralogical composition [*Sokolik*, 2002]. Therefore, we conclude that the different regional mineralogical composition of dust, which controls its radiative properties in the IR spectrum, is likely the main reason for the observed differences in the regional dust signature as was suggested by previous modeling studies [*Sokolik et al.*, 1998; *Sokolik*, 2002]. It seems that, by accounting for the angular geometry, one can constrain the regional dust composition based on the results shown in Figure 37. Unfortunately, an additional complexity arises from the fact that dust exhibits a complex multi-layered vertical distribution during

mid- and long-range transport in the atmosphere. Dust properties can differ from layer to layer and thus can hamper the interpretation of the regional BTD in terms of differences in the dust mineralogical composition. Collocated MODIS and CALIPSO observations can provide valuable data to further explore the nature of the dust regional radiative signature.

3.4.3 A statistical approach for discrimination of mineral aerosols from clouds using spatial variability of satellite visible radiances

3.4.3.1 Calculation of the standard deviation and local inhomogeneity parameter

Several different parameters were used in past studies to quantify the spatial variability of satellite reflectances observed in the presence of aerosols or clouds. One common approach is to use the standard deviation of reflectances calculated for a group of adjacent 3×3 pixels [e.g., *Martins et al.*, 2002]. In this case STD is computed as

$$STD = \sqrt{\langle R^2 \rangle - \langle R \rangle^2}, \tag{23}$$

where R is the satellite reflectance of a single pixel and $\langle\ \rangle$ denotes spatial averaging. Usually the averaging is performed over a group of 3×3 pixels. The STD is then assigned to the central pixel. One disadvantage of this approach is that the STD depends on the reflectance values themselves, which in turn depend on the solar and satellite geometry. To overcome this problem, one can introduce another parameter, called local inhomogeneity parameter (LIP), as

$$LIP = 1 - \frac{\exp \langle \ln R \rangle}{\langle R \rangle}. \tag{24}$$

Originally, LIP was defined as a function of the optical thickness of clouds [*Alexandrov et al.*, 2004]. Here we modify this definition by describing LIP in terms of satellite reflectances. The LIP values range from 0 for homogeneous to 1 for highly inhomogeneous data sets. For all considered cases, we also calculated the probability density function (PDF) and the cumulative distribution function (CDF) of STD and LIP.

Initial inspection of STDs and LIPs revealed highly right (positively) skewed distributions in all data sets. Therefore, the data were subjected to a power transformation that

produced approximately normal distributions. An exponential transformation was applied to the STD data, while a logarithmic transformation was used in the LIP data. After the power transformation, hereafter denoted as $\mathbb{T}$, the PDFs for each category were calculated as follows:

$$PDF(\varepsilon_i^{\mathbb{T}}) = \frac{1}{\delta\varepsilon^{\mathbb{T}}}\frac{N_i^{\mathbb{T}}}{N}, \tag{25}$$

where $\varepsilon_i^{\mathbb{T}}$ is the center and $N_i^{\mathbb{T}}$ is the number of data in the ith bin, N is the total number of points of the given category, and $\delta\varepsilon^{\mathbb{T}}$ is the bin width. The bin width was calculated using the Freedman-Diaconis rule [*Wilks*, 2005, p. 34]:

$$\delta\varepsilon^{\mathbb{T}} = \frac{c\ IQR^{\mathbb{T}}}{N^{1/3}}, \tag{26}$$

where $IQR^{\mathbb{T}}$ is the interquartile range and c is a parameter for which we assigned values between 2.2 and 2.5.

Then the power transformations were inverted, and PDFs of the original data sets were calculated from the transformed PDFs using the following relationship:

$$PDF(\varepsilon_i) = PDF(\varepsilon_i^{\mathbb{T}})\frac{d\mathbb{T}(\varepsilon)}{d\varepsilon}\Big|_{\varepsilon=\varepsilon_i}, \tag{27}$$

In turn, the CDF was calculated from the corresponding PDF as

$$CDF(\varepsilon_i) = Pr\{\varepsilon \le \varepsilon_i\} = \sum_{j\le i} PDF(\varepsilon_j)\delta\varepsilon_j, \tag{28}$$

where $\varepsilon_i = \mathbb{T}^{-1}\left(\varepsilon_i^{\mathbb{T}}\right)$ is the position of the ith bin with width

$$\delta\varepsilon_i = \mathbb{T}^{-1}\left((i+1)\delta\varepsilon^{\mathbb{T}}\right) - \mathbb{T}^{-1}\left(i\delta\varepsilon^{\mathbb{T}}\right),$$

and $\mathbb{T}^{-1}$ denotes the inversed transformation function.

3.4.3.2 Probabilistic dust-cloud mask

Figure 38 shows the PDF and CDF computed for the considered categories when STD is used as a measure of spatial variability. The PDF of dust reaches its maximum for smaller STD values compared to those of heavy dust. Dust category PDF is considerably larger

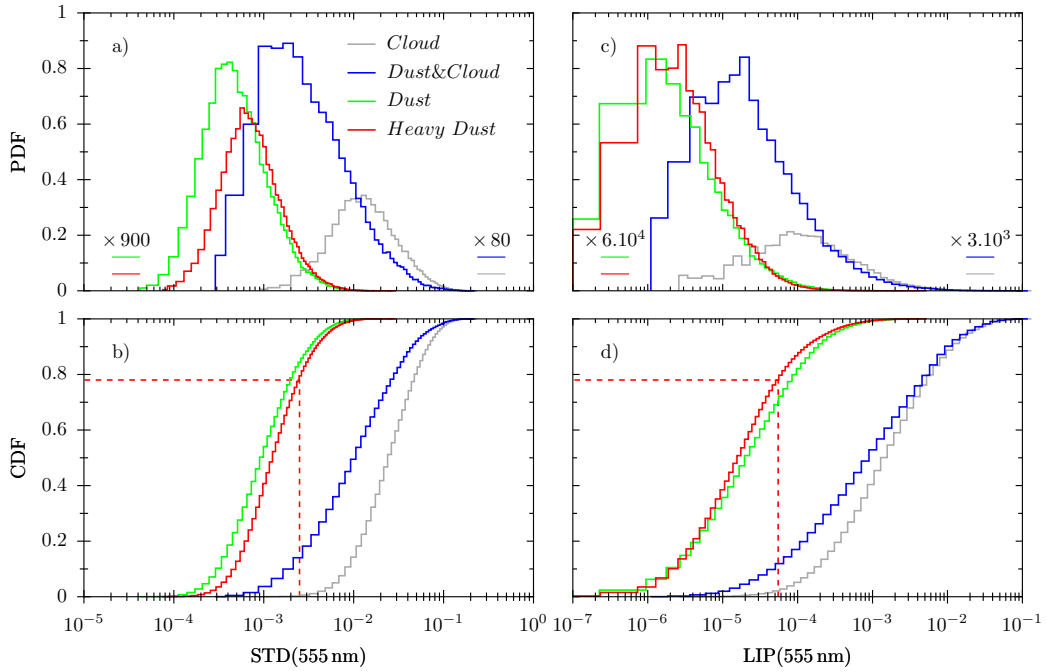

Figure 38: PDFs and CDFs computed for considered categories: cloud, dust-cloud mixed, dust, and heavy dust. The dashed red line shows the operational fix STD threshold value used in MODIS.

than heavy dust PDF for STD smaller than 7×10^{-4}, beyond that point both curves have similar values. The differences on the left wing of the histograms can be attributed to the pixels with smaller dust reflectances. At its maximum, PDF of dust has a value of about 0.8, which is larger than that of heavy dust (about 0.6).

Comparing our results to Figure 2 from *Martins et al.* [2002], which shows a histogram for aerosol and cloudy pixels, it is apparent that significant percentage (about 55%) of dust and heavy dust pixels have STD larger than the *Martins et al.* [2002] best separation threshold. In contrast, cloudy pixels on both figures have almost the same STD distributions. Furthermore, the MODIS aerosol/cloud mask algorithm uses the same threshold value for all aerosol types and therefore one can expect that dust and heavy dust pixels could be misclassified as cloudy pixels. Indeed, the CDF of heavy dust pixels shows that the MODIS operational threshold (depicted as a red dashed line in Figure 38) corresponds to about 80% probability for a dusty pixel to be classified correctly. This implies that about 20%

of the dust pixels are likely to be misclassified as cloudy. Another limitation of the fixed STD threshold approach is that it gives only two possible classifications: aerosol or cloudy pixels, missing the occurrence of mixed pixels. Figure 38(a) clearly demonstrates that the PDF of mixed dust-cloud pixels is quite different from the PDFs of dusty or cloudy pixels, and that it overlaps with the latter two. Notice that applying the MODIS STD threshold leads to about 15% probability of dust-cloud mixed pixels to be classified as dust, while the cloud misclassification is negligible. In contrast to the dust case, PDFs of both cloudy and mixed dust-cloud pixels have much longer wings. This allows for a good discrimination from dust pixels at larger STDs. However, the PDF and CDF curves have similar values for STD larger than 0.1, making the discrimination between cloudy and mixed dust-cloud categories practically impossible.

Similar analysis was carried out using the LIP data. The LIP PDFs and CDFs are shown in Figure 38(c, d). Although it is not possible to directly compare STD and LIP histograms, one can notice very similar relative positions of the different categories. Compared to the STD case, one noticeable difference is that dust and heavy dust categories have similar LIP histograms. This is because of the weaker dependence of LIP on the absolute values of the reflectances. LIP, however, does not offer any other significant improvements over STD. It is likely that the 3D effects in clouds strengthen the STD-based detection and therefore increase the distance between the cloud category and dust.

To increase the percentage of correctly identified dusty pixels, one can select a threshold value that corresponds to a higher percentile. However, the disadvantage of this approach is the increased number of cloudy and mixed dust-cloud pixels that will be misclassified as dust (see Figure 38). We are left with two options. The first one is to use a fixed threshold value and accept the likely misclassification of some dust pixels. In this way a deterministic aerosol-cloud mask can be constructed. However, we observed that including the mixed dust-cloud category in the discrimination does not allow for good separation of

the category mean relative to the data scatter. As a consequence, the deterministic aerosol-cloud mask cannot provide information about mixed or collocated dust-cloud pixels. An alternative option is to preserve the information about the data distribution in the form of their PDFs. The advantage of this approach is that it allows finding the probability of the retrieved pixels to be identified as one of the categories included in the manual classification (and in the statistical analysis). In addition, the classification probability can be interpreted as a confidence level of the correctly classified pixel.

The probabilistic discrimination (or classification of the pixels) can be achieved through the following expression [Bayes theorem, *Wilks*, 2005, p.542]:

$$Pr\{c;\varepsilon\} = \frac{w_c PDF_c(\varepsilon)}{\sum_{t=\{c\}} w_t PDF_t(\varepsilon)}. \tag{29}$$

Equation 29 gives the probability ε of a pixel with spatial variability to be classified as belonging to the category c. Here $PDF_t(\varepsilon)$ is the prior PDF calculated for a given category t, and w_t is the frequency with which that category is represented.

To simplify the analysis we merged dust and heavy dust pixels into one category, which from here on we referred to as dust. Figure 39(a) shows the classification probabilities for the three categories when STD is used as a measure of the spatial homogeneity. Most of the pixels with small STD values will be classified as dust. However, for values of STD between 0.005 and 0.007, the classification probability is distributed almost equally between dust and mixed dust-cloud categories. A further increase in STD leads to a sharp decrease in the probability of a pixel to be classified as dusty, and the mixed dust-cloud probability reaches its maximum value of 45%. The cloud category starts to dominate when STD becomes larger that 0.02 and the probability for the pixel to be cloudy increases from 50% to about 80%. At the same time, the probability of the pixel to be mixed dust-cloud steadily decreases to about 30%, while the probability of the pixel to be dust is practically zero.

In a similar fashion, we calculated the classification probabilities based on LIP PDFs. The results are shown in Figure 39(b). For small LIP values the classification probability

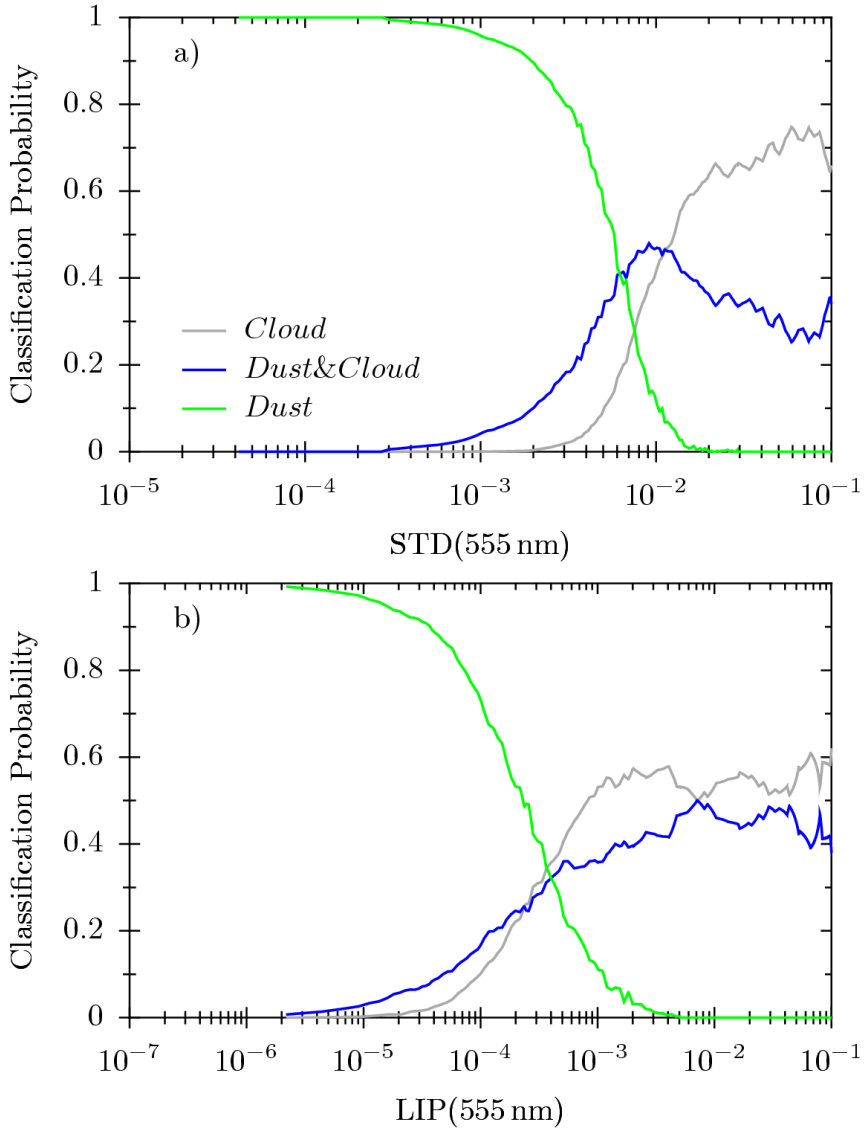

Figure 39: Classification probabilities of a pixel to be dust, cloud or mixed dust-cloud calculated by using STD and LIP as a measure of the variability.

is dominated by the dust category. For a LIP value of about 2×10^{-4}, it is almost equally distributed between the dust, mixed dust-cloud, and cloud categories. A further increase of LIP decreases the probability of a pixel to be classified as dusty but increases the probability for mixed and cloudy pixels. An apparant difference compared to the STD case is the rather poor separation between mixed and cloudy pixels. Despite its theoretical advantages, we see no compelling reasons to prefer LIP to STD.

In order to assess the performance of the probabilistic STD approach, we calculated its classification skill. The skill can be expressed by a (cross classification) matrix with indexes corresponding to the categories and with elements $CCM(c \mapsto t)$, which are equal to the probability of a category c to be classified as a category t:

$$CCM(c \mapsto t) = \int_{\Omega_\varepsilon} PDF_c(\varepsilon) Pr\{t; \varepsilon\} d\varepsilon. \tag{30}$$

Here $PDF_c(\varepsilon)$ is calculated following Equation 27, and the classification probability $Pr\{t; \varepsilon\}$ is calculated following Equation 29. The integration is performed over the entire range of the inhomogeneity parameter Ω_ε. The diagonal elements of this square matrix are equal to the probability of each category to be classified correctly. These probabilities can be viewed as the best classification skill that one can achieve based on a particular learning set. In the ideal case when there is no overlapping between the PDFs, there is no misclassification and the matrix becomes an identity matrix. In practice, one would like to maximize the diagonal elements and minimize the non-diagonal elements in order to achieve the best possible classification. If the categories are represented by equal number of pixels, the classification matrix becomes symmetric. However, in the general case, any two elements that are symmetric about the main diagonal are related trough the ratio of the corresponding frequencies:

$$CCM(c \mapsto t) = \frac{w_t}{w_c} CCM(c \mapsto t). \tag{31}$$

Naturally, the sum of the elements in a given row is one

$$\sum_i CCM(c \mapsto t_i) = 1,$$

Table 7: Comparison of the classification skills of the probabilistic STD and the fixed threshold STD approaches. Only dusty and cloudy data are considered.

	Observed category classified as			
	Dust		Cloud	
Observed	Probabilistic	Fixed threshold	Probabilistic	Fixed threshold
Dust	97.3	81.0	2.7	19.0
Cloud	9.6	0.3	90.4	99.7

however, as can be seen from Equation 31, this is not the case for the sum of the elements in a given column

$$\sum_i CCM(c_i \mapsto t) \neq 1.$$

Table 7 shows the detection skill if only dust and cloud categories are considered. One can notice that the probabilistic mask performs better in classifying dust pixels, and, as expected, the fixed threshold approach works better in classifying clouds. However, if mixed dust-cloud category is included in the analysis (Table 8), there is a 7% drop in the detection skill of dust, mainly due to dust and cloud misclassification. The detection skill of clouds suffers due to the same reason, but still remains good at about 60%. Notice that the mixed dust-cloud pixels classification skills are almost evenly distributed between the three categories. The low detection skill of the mixed dust-cloud category demonstrates the limitation of the spatial variability approach when it is applied to mixed dust and cloud scenes.

3.5 Conclusions

In this chapter we identified the advantages and the limitations of ground based and satellite data to characterize atmospheric dust fields on a variety of spatial and temporal scales. In addition, we pointed out some of the deficiencies in the current dust detection techniques in visible and thermal-IR part of the spectra.

Table 8: Classification skills of the probabilistic STD approach.

	Classified		
Observed	Dust	Cloud	Dust and Cloud
Dust	89.9	1.7	8.5
Cloud	6.0	58.3	35.7
Dust and Cloud	31.6	36.9	31.5

Table 9: Same as Table 7, except for LIP.

	Observed category classified as			
	Dust		Cloud	
Observed	Probabilistic	Fixed threshold	Probabilistic	Fixed threshold
Dust	93.2	NA	6.8	NA
Cloud	24.6	NA	76.4	NA

Table 10: Same as Table 8, except for LIP.

	Classified		
Observed	Dust	Cloud	Dust and Cloud
Dust	86.8	5.1	8.1
Cloud	18.2	45.3	36.5
Dust and Cloud	29.5	38.0	32.5

We utilized MODIS data to investigate the thermal-IR radiative signature of atmospheric dust and point out implications to dust detection. Forty-nine dust scenes were analyzed for seven different regions over the oceans during the 2000–2004 time period.

Our analysis demonstrated that automated discrimination between cloudy and dusty pixels based on the split-window or the trispectral approach with a fixed global BTD threshold is not reliable. For some of the regions it is still possible to use $BT_{11} - BT_{12}$ difference as a simple, regionally-dependent single value threshold test for dust detection. An interesting finding that confirms the presence of the regional radiative signature of dust is that clear sky pixels tend to group in a tight cluster on the trispectral diagram while the dusty data show significant scatter. In the presence of dust, BTD values for some of the regions tend to group, while others have some distinct features. For instance, regardless of the viewing angle, regions 1 (8°–16°N) and 2 tend to have positive $BT_{11} - BT_{12}$, whereas region 6 has positive $BT_8 - BT_{11}$. Dust from East Asia shows distinct signature in the thermal-IR, which further reinforces our opinion that dust retrieval algorithms and regional models should be tailored towards the regional specifics of dust.

Based on our analysis, we conclude that the regional radiative signature of dust observed in the MODIS data is likely caused by the differences in the mineralogical composition controlled by the diverse dust sources. Thus, one has to consider the origin of atmospheric dust in order to utilize the BT difference techniques in their full potential. In turn, the regional IR signature may be helpful in identifying the origin of dust plumes from remote sensing observations. A combination of passive IR remote sensing and the space lidar CALIPSO has a good potential to provide an additional constraint on dust regional properties.

The need to carefully examine the characteristics of atmospheric dust, i.e., spatial variability, is evident from the fact that 20% of the dusty pixels can be lost or likely misclassified as cloudy if one relies on the fixed threshold STD cloud-aerosol mask. We expanded

the dust-cloud discrimination tools by adding a simple one channel algorithm that is guaranteed to perform at least as good as the fixed threshold STD approach. The methodology developed here was tested with two spatial variability parameters: STD and LIP. Despite its theoretical advantages, LIP does not show any significant improvements in the discrimination of dust from clouds. One possibility that can explain the better performance of STD over LIP is that the former is more sensitive to three-dimensional radiative effects in clouds, which actually help in the discrimination.

The approach based on PDFs can help the development of new and improved dust detection methods and retrievals, especially in the case of mixed dust and cloud pixels. In addition to the extended discrimination capabilities, it provides information about the classification skill. This is a key advantage over the fixed STD approach because it enables determining the confidence level of the data to be of a certain type, and can be used to evaluate the quality of the retrievals.

CHAPTER IV

CHARACTERIZATION OF 3D DUST DISTRIBUTIONS BY INTEGRATING OBSERVATIONS AND MODELING DATA

4.1 Introduction

In this chapter, we outline a framework for integration of modeling and observations to fully characterize the 3D dust fields on a regional level. In Section 4.2 we discuss methodological issues relevant to regional modeling of dust and integration with observations by reviewing past studies. Section 4.3 describes the WRF-DuMo model setup, and investigates the role of soil moisture on the modeled dust optical thickness (DOT) in an attempt to tune up the model. Section 4.4 explores the effect of dust emission schemes on the modeled DOT and visibility. Section 4.5 compares the modeled visibility and dust optical thickness calculated with different parameterizations of dust emission with the MODIS and CALIPSO aerosol optical thickness (AOT). Section 4.6 outlines the basis for the development of an integrated observational and modeling dust framework. We introduce an ensemble model dust index (MDI), which gives the probability for dust to be present that is determined from the modeled dust optical thickness and visibility. Section 4.7 concludes the chapter.

4.2 Methodological aspects of integration of models with observations

Quantitative characterization of the 3D dust fields from observations alone is a formidable task because of various inherent limitations (see Chapter 3). Modeling, on the other hand, offers a great flexibility in terms of output data and its spatial and temporal resolution and coverage. The complexity of the processes involved in the dust lifecycle, our capability to model them as well as the quality of the input data used to drive the model suggests that

this flexibility comes at the price of an increased uncertainty in the modeled fields. The synergy between modeling and observations is desirable in order to combine the strength of modeling, lessen the limitations of observations, and minimize the difference between them.

Because no single existing data set fully describes all aspects of the dust cycle, validation of modeled dust distributions commonly include comparisons with different types of observational data. For example, *Cakmur et al.* [2006] used aerosol optical thickness from AERONET, AVHRR and TOMS, surface concentrations, deposition and size distribution data to constrain the magnitude of the global dust cycle by minimizing the squared difference between the modeled (GISS AGCM) dust distribution and observations. *Yumimoto et al.* [2007] and *Uno et al.* [2008] went a step further and developed the four-dimensional variational data assimilation system RAMS/CFORS-4DVAR (RC4) that was used to optimize the model dust emission by assimilating data from the NIES LIDAR network. The above studies used different formulations of the simple dust emission scheme (Chapter 2). Using a simple dust emission scheme greatly simplifies the minimization problem, because the only free parameter that needs to be considered is the emission constant C. Although the emission constant controls the magnitude of the emitted dust mass, no attempts have been made to assimilate vertical dust flux measurements due to the lack of in situ measurements. As a consequence, the minimization between the models and the data reflects the optimum dust concentration in the atmosphere rather than the emitted dust mass. This raises a question on whether or not the available data are sufficient to constrain the dust emission. One can argue that ultimately the emission controls the atmospheric dust concentrations, if the transport and sinks processes are accurately modeled; therefore, minimizing the differences between the simulation and the observations will indeed produce the optimum dust emission. However, large uncertainties are currently present in the modeled initial emission particle sizes, also in the dry and wet removal processes, so it is unlikely that dust models can guarantee the above assertion.

Performing minimization between the observations and the physically-based dust emission schemes turns out to be an even more complicated and challenging task. The physically-based dust emission parameterizations (e.g., MB95 and Shao96), which were implemented in WRF-DuMo (see Chapter 2), depend on a number of internal and external parameters. The internal parameters are variables or coefficients within the parameterization that cannot be derived analytically and are determined experimentally (i.e., best fit to dust emission data). They can vary within a certain range depending on the land surface or meteorological conditions. For example, the constant Γ in the Shao96 threshold friction velocity can vary between $(1.64 - 5) \times 10^{-4}\ kgs^{-2}$, and the selection of the dust particle cut-off diameter in the Shao96 vertical flux depends on the magnitude of the surface wind velocity (see Appendix A).

The external parameters that are required to drive the emission schemes include wind friction velocity, soil moisture, surface roughness, among others. In WRF-DuMo, external parameters are provided either from the model calculations or from external datasets. Since the physically based dust emission schemes are developed to operate on aeolian scales (millimeters to centimeters), which are much smaller than the grid size of a regional model (kilometers), it is very challenging to provide the input parameters on the same scales. Thus, biases in model predicted dust fluxes could come from the scale discrepancies between the dust emission parameterization and the external parameters. In addition, MB95 and Shao96 schemes respond quite differently to the same input parameters (e.g., soil moisture) that may lead to even bigger differences between dust fluxes predicted with both schemes.

The schemes can be reasonably well validated at certain locations, where surface and meteorological variables can be measured with high accuracy and on scales suitable for dust emission. Once the schemes are incorporated in a mesoscale model, the spatial scale inconsistency can be addressed either by introducing subgrid variations in the input variables or tuning their values before feeding them into the dust emission schemes. Modeled

soil moisture, for instance, is one such parameter, which needs careful assessment before it is ingested by the dust emission schemes. Soil moisture is a critical variable in a sense that it can completely shut off dust emission. This variable is predicted by WRF only at four vertical layers (the topmost layer being 10 cm), while the dust emission schemes require soil moisture within the top 1–2 cm of the soil. Thus, using model predicted soil moisture can affect the magnitude of the threshold friction velocity and significantly alter the emission patterns.

Careful tuning of the model and removal of the existing biases can help to decrease the parameter space dimensionality and simplify the optimization procedure. However, the lack of direct measurements of dust emission often requires the use of other variables instead of vertical dust fluxes that can serve as proxies for the intensity of dust emission. An example is the AOT retrieved from a satellite, based on a mixture of aerosols with assumed globally representative size distributions, and the AOT calculated from the modeled dust size-segregated mass distribution in the atmosphere. Therefore, differences between the model output and observations still can be present even after minimization was performed. In general, one can proceed in two ways: either use the model output alone assuming that the minimization results in realistic representation of the simulated fields; or merge the model output with the observations by finding a way of integrating the continuous spatiotemporal fields from the model simulations and the robustness of the observational data.

Integration of dust models, observations from ground-based stations and remote sensing data potentially can greatly benefit both models and observations. For example, remote sensing offers a good spatial coverage and provides observational data, in the form of AOT or information about the vertical distribution of the atmospheric dust that can be assimilated in the dust model. On the other hand the dust model, especially if used as a forecasting tool, can aid the real time remote sensing retrievals by providing independent information where dust aerosols are likely to be present and, therefore, can potentially improve the aerosol

retrievals. It is important to stress that the integrated approach can actually address two issues: (1) improve our knowledge about the location, extend and vertical structure of dust plumes, and (2) improve our ability to quantify 3D spatial dust fields by merging models and observations to fill the spatiotemporal gaps/limitations of individual datasets.

While the first point seems to provide somewhat limited information about dust presence in the atmosphere, it is the most basic information needed to study dust. Consider, for example, studying the effects of dust on clouds. We know that simultaneous satellite retrievals of cloud and aerosol properties are possible in very limited number of cases; however, the problem itself requires such information, which can be obtained by merging the cloud observations with the modeled dust fields. Another example is the aerosol-cloud mask, which determines what retrieval algorithm will be applied for clouds and for aerosols. In some cases (see Chapter 3), dust can be misclassified as a cloud and affect the aerosol retrieval. Therefore, any additional information about the dust presence can help to lessen the problem. The second point is rather obvious. For example, the AOT retrieved from satellites has been widely used as a proxy for the presence of dust. However, AOT does not provide information about the vertical distribution of dust, which is needed for studying the radiative effect of dust, as well as other dust-induced impacts. Merging retrieved AOT and modeled 3D dust distribution can alleviate this problem.

4.3 Soil moisture tuning in WRF-DuMo

As shown in Chapter 2, the modeling of dust cycle requires reliable characterization of dust emission, mixing, transport and deposition. The performance of such a complex modeling system depends on the realism of parameterizations used to simulate individual dust processes, the combination of their internal parameters, as well as the external variables, which drive the parameterizations. Internal parameters are derived for a specific set of surface and meteorological conditions, while external parameters are obviously model dependent. Having implemented two physically based dust emission schemes each with its

own parameterizations and input parameters, it is clear that some difference between the modeled dust loadings is to be expected. Differences in dust emission fluxes between the two schemes further propagate in the model predicted 3D concentration fields and dust optical thicknesses. In this chapter the internal parameters of the schemes were selected such that the discrepancy between the simulated vertical fluxes was minimized. This suggests that the expected "true" vertical fluxes are bracketed by MB95 and Shao96 vertical fluxes, which may not be necessarily true. Since modeled vertical fluxes cannot be directly validated, we chose the internal parameters that produce more realistic atmospheric dust fields in terms of dust optical thickness.

The external variables that drive the schemes are not suited for aeolian scales, but rather for regional scales. This is especially true for modeled winds and modeled soil moisture content. It comes as no surprise that these two variables are the ones that are most commonly tuned in regional models. For instance, *Heinold et al.* [2007] and *Laurent et al.* [2006] did not use the model predicted friction velocity u_*, but logarithmically derived u_* to match the difference in the scales between surface roughness z_0 used in the regional model and dust emission schemes. Furthermore, *Heinold et al.* increased the wind speeds by a factor of 0.66 to produce vertical fluxes that match dust optical thickness from TOMS and MODIS.

Similarly, soil moisture is another critical parameter that strongly influences the amount of emitted dust. Regional models usually predict soil moisture in several layers (3 to 6) with the thickness of the first layer varying between 5 and 30 cm. Moisture corrections in dust emission schemes require soil moisture in the top 1–2 cm soil layer. In regional models, the land surface schemes rely on the soil texture based on disturbed soils in contrast to dust emission schemes, which require undisturbed soil size distributions. For instance, the clay fraction in WRF is based on the USDA soil texture and vary between 3% and 60%, while clay fractions of undisturbed soils used in MB95 and Shao96 dust production schemes do not exceed 12% [*Darmenova et al.*, 2008]. This produces bias in the *Fécan et al.* [1999]

moisture correction used in the MB95 and Shao96 threshold friction velocities, since it has a dependence on both gravimetric moisture and clay fraction. *Darmenova et al.* [2008] showed that the typical range of soil moistures in arid and semiarid regions is from 0.01 to 0.16 m^3/m^3 in the topmost 1–2 cm, while the WRF Noah land surface model produces values between 0.1 and 0.45 m^3/m^3 in the top 10 cm. It is expected that the moisture in the 10 cm soil column will be greater than the moisture in the topmost 1–2 cm column, however comparison with in situ measurements for Gobi surfaces performed in the top 10 cm soil layer showed that the WRF Noah scheme still tends to overpredict soil moisture in desert regions. *Gong et al.* [2003] compared soil moisture measured in Chinese deserts with modeled soil moisture and found that the NARCM model overpredicts the soil moisture by a factor of two. In contrast, *Park et al.* [2007] used a simplified bulk moisture model in the same model and found that their land surface model greatly underpredicts soil moisture, thus they decided to tune the soil moisture in their dust emission module by increasing it by a factor of 2.345.

This motivated us to investigate the importance of modeled soil moisture on simulated dust 3D fields with both MB95 and Shao96 dust emission schemes, while keeping the initial dust aerosol size distribution and the rest of the model options the same during the experiments. WRF-DuMo runs were performed at 10×10 km horizontal resolution, 37 vertical layers, exponential in PBL injection scheme, and initial dust size distribution same as in our base run described in Chapter 2 (Table 5). We simulated the Spring 2007 dust event, discussed in details in Chapter 2. The CALIPSO AOT and MODIS-Aqua AOT derived with the "Deep Blue" aerosol retrieval algorithm are available for this time period that makes it possible to compare the model predicted 3D dust fields against these two data sets.

4.3.1 The effect of soil moisture on modeled dust optical thickness

The large discrepancy between observed and modeled soil moisture motivated us to perform two sets of runs - with uniformly decreased soil moisture over the entire domain by a factor of 0.1 and 0.5 (hereafter denoted as $0.1w$ and $0.5w$).

Figure 40 shows the modeled DOT calculated with the MB95 scheme for the two soil moisture experiments on March 30, 2007, 3:20 UTC. Similarly, Figure 41 shows the DOT calculated with the Shao96 scheme with moisture $0.1w$ and $0.5w$. In both cases one can see the strong dependence of DOTs on the soil moisture – increasing the soil moisture suppresses dust emission and decreases the modeled DOT. Figure 41 clearly shows that in the case of the Shao96 scheme larger areas are affected due to changes by of the soil moisture. Despite the large DOT produced by both schemes, it is apparent that the DOT patterns over land are similar. Largest DOTs are observed over the Gobi Desert, followed by the Taklamakan and Gurban Tungut deserts. Reducing the soil moisture by a factor of 0.5 decreases DOT over Northeast China, but DOTs over the Gobi still remain high in both schemes.

Figures 42 and 43 show DOTs modeled with the MB95 and Shao96 schemes, respectively, on 1 April, 2007, 3:20 UTC for the two sets of moisture. On this date, the dust storm over the Gobi died out, so the modeled DOTs are a result of a mid-range dust transport. It can be seen that on 1 April the dust plume is transported over the East Sea and Sea of Japan. The Shao96 scheme with $0.1w$ produces DOT values of 10 and higher off the coast of Japan, while over the same region the DOT calculated with $0.5w$ are between 3 and 5. In the case of $0.5w$, the MB95 scheme is the one with the largest DOT over the same area.

Limited data over the dust sources makes it difficult to figure out which scheme performs better in depicting the active dust sources. With the acceptance of the new Deep Blue retrieval algorithm of the MODIS-Aqua aerosol product (MYD04_L2), AOT data over land has been significantly improved, especially over bright arid regions. Comparison between the modeled DOT (Figures 40, 41, 42 and 43) and the composites of MODIS-Aqua AOT

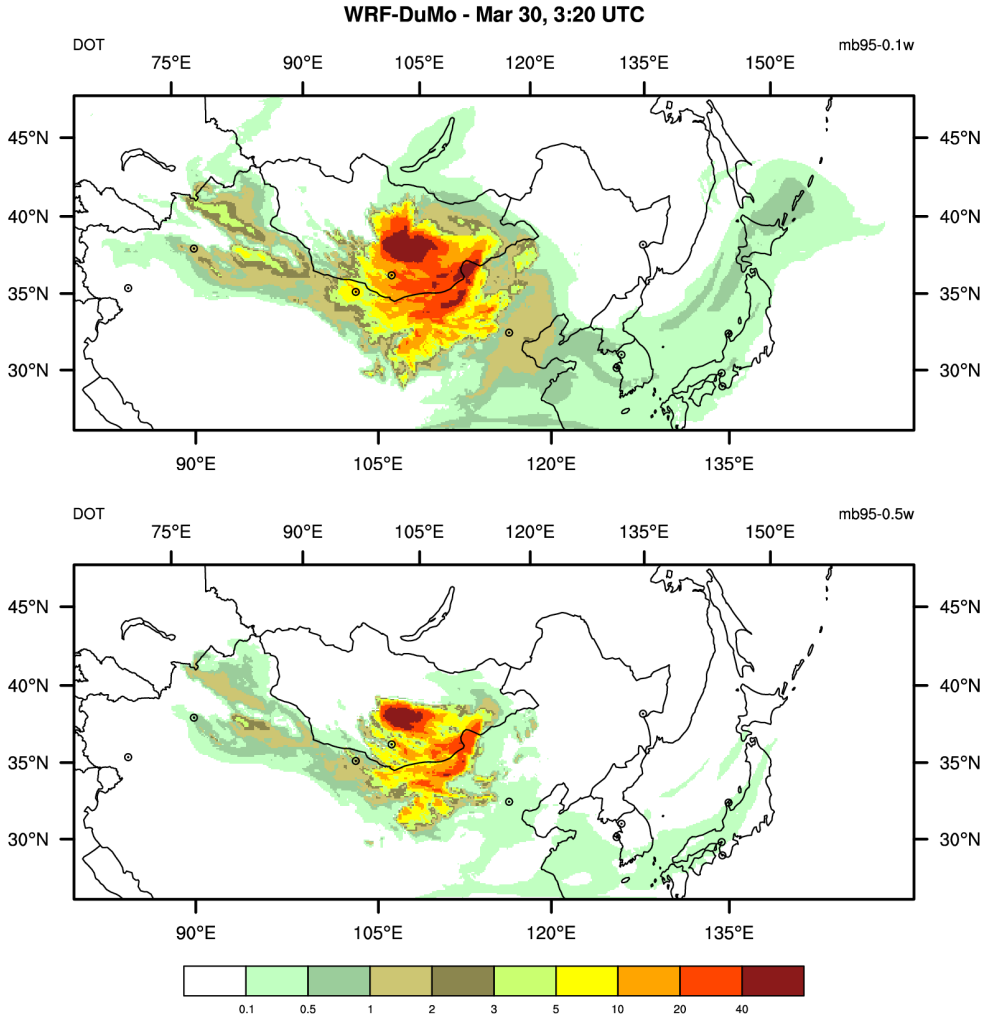

Figure 40: Dust optical thickness on March 30, 2007 3:20 UTC calculated with the MB95 scheme with $0.1w$ (top) and $0.5w$ (bottom).

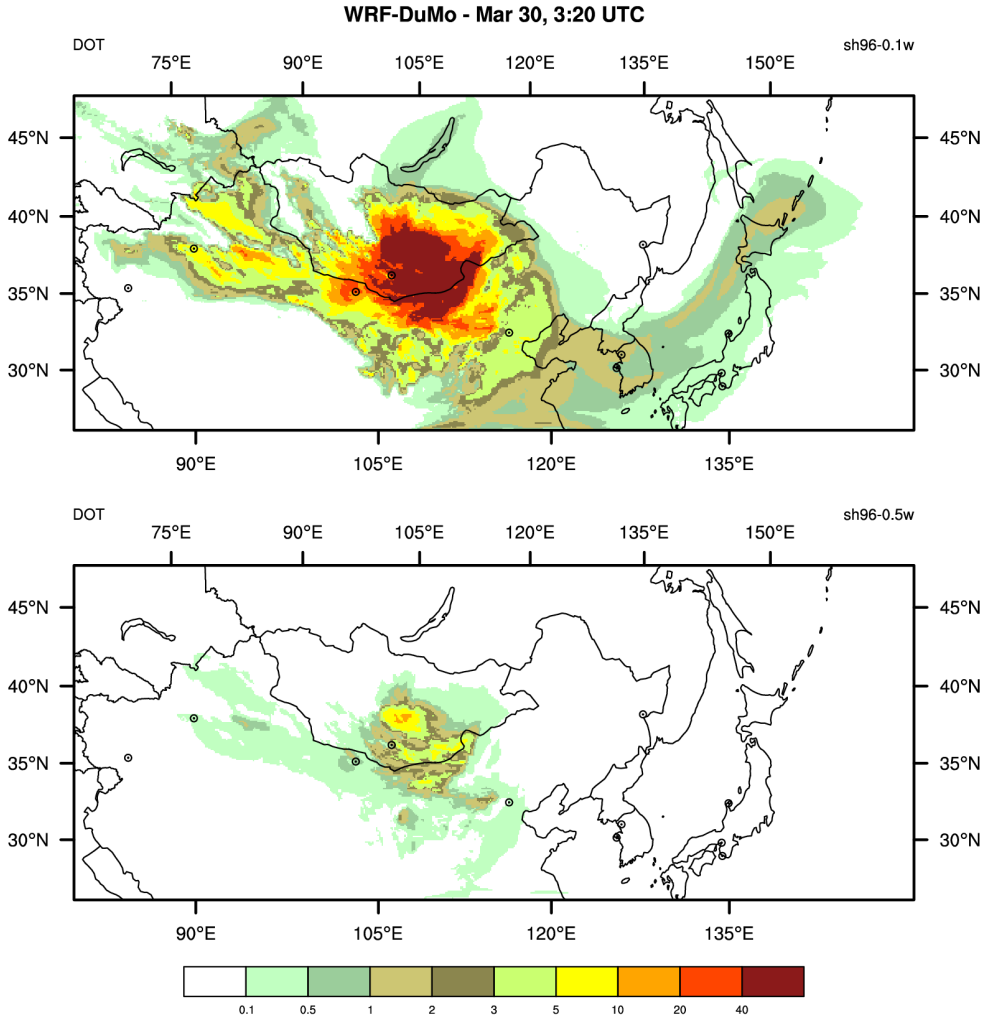

Figure 41: Dust optical thickness on March 30, 2007 3:20 UTC calculated with Shao96 scheme with $0.1w$ (top) and $0.5w$ (bottom).

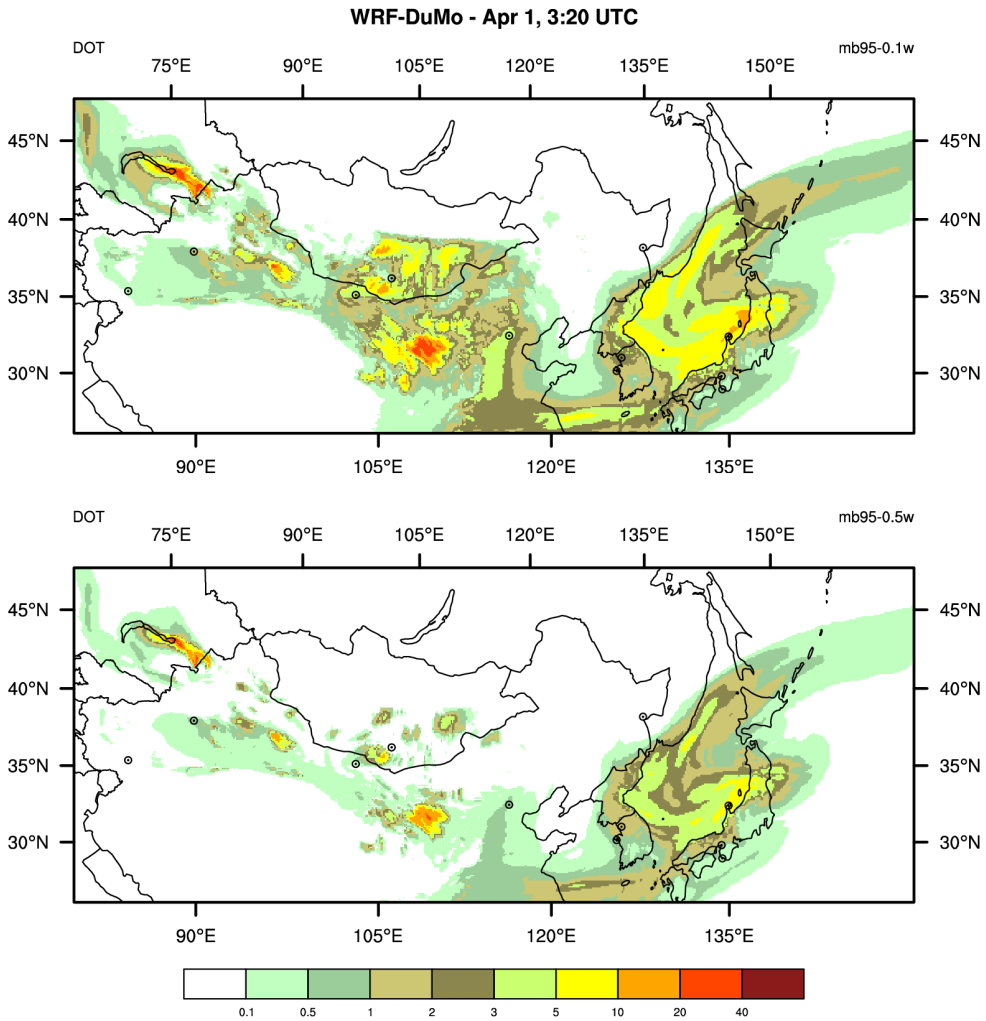

Figure 42: Same as 40, except for April 1, 2007 3:20 UTC.

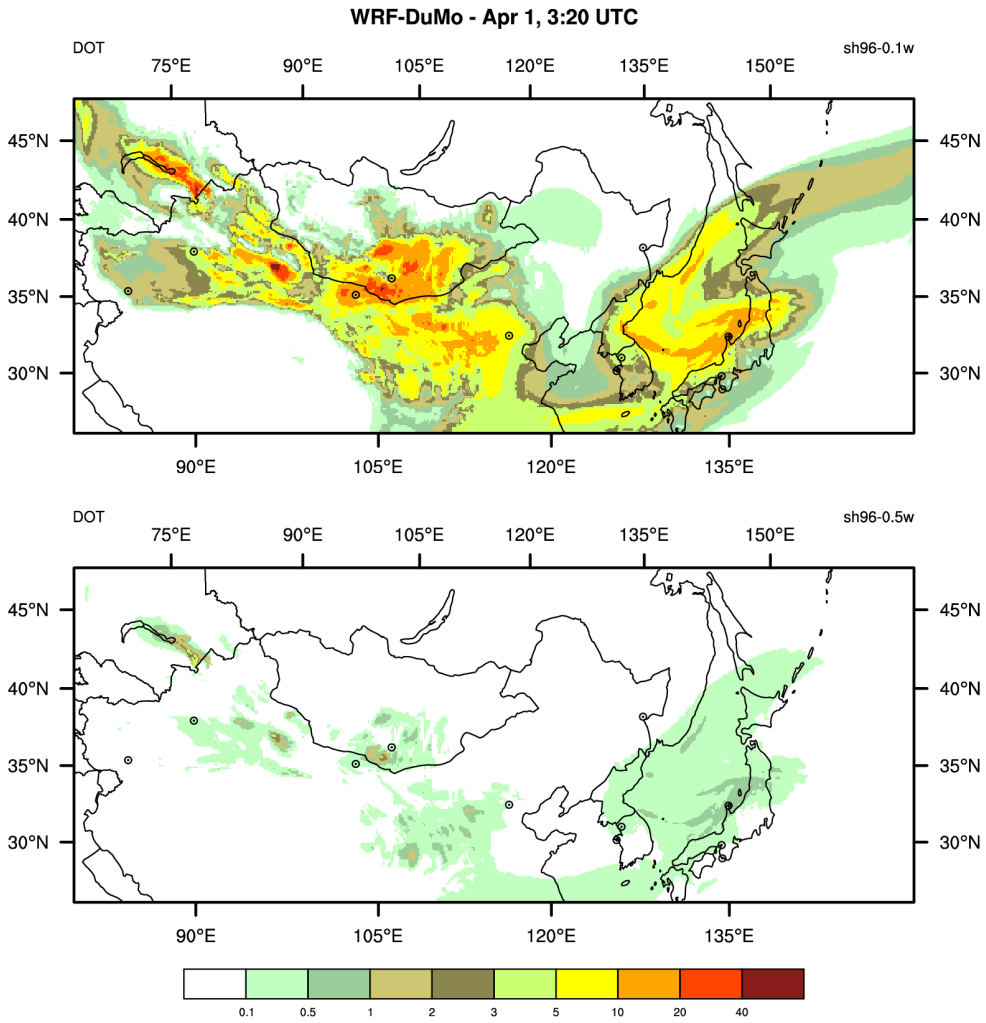

Figure 43: Same as 41, except for April 1, 2007 3:20 UTC.

on 30 March and 2 April (Figure 55) suggest that both schemes significantly overestimate the emission if $0.1w$ is used, and therefore we proceed with our analysis using the results derived with $0.5w$.

4.4 The effect of dust production schemes on dust optical thickness and visibility

Uncertainty in the dust emission is recognized as one of the major factors resulting in the significant discrepancies in the modeled dust fields [*Uno et al.*, 2006]. WRF-DuMo includes three dust production schemes, which gives us the opportunity to investigate how the dust emission schemes affect the modeled DOT and visibility, within the same modeling framework. Differences in the dust emissions exhibit a complex spatiotemporal pattern, due to the different sensitivity of each dust production scheme to meteorological and land surface parameters [*Darmenova et al.*, 2008]. It can be expected that over dust sources the DOT and visibility patterns will be similar to the dust emission patterns produced by the individual emission scheme. However, downwind of dust sources, the DOT and visibility patterns will be affected by horizontal and vertical mixing, and dry removal, which will likely smooth out the initial differences between the emission schemes.

In addition to MB95 and Shao96 experiments, we also performed simulation with the simple dust production scheme (allowing for dust emission to occur only from the predefined sources in the terrestrial preprocessor). The emission constant $C = 3.6{\times}10^{-13} gcm^{-5}s^2$ was selected such that the total emitted mass calculated with the simple scheme matched the average mass of MB95 and Shao96 experiments for the duration of the simulation.

4.4.1 Correlation analysis of modeled dust optical thickness

Significant differences in the DOT calculated with MB95, Shao96, and the simple schemes are evident from Figures 44 and 45. On 30 March, all schemes show the largest DOT over the Gobi Desert, while on 2 April the maximum DOT is observed over the Gurban Tunggut and Taklamakan. During the entire simulation period, MB95 produced the largest

DOT over the active source regions, followed by the simple and Shao96 schemes. The mean DOT (Figure 46) of MB95 and Shao96 differs by a factor of 10 over the Gobi Desert. Differences in the emitted dust mass are especially evident by the different values of DOT along the easterly mid-range transport route across the Yellow Sea and Japan.

One can also see from Figures 44, 45 and 46 that the spatial patterns of the modeled DOT exhibit some similarities - maximum DOT are observed for all schemes over the Inner Mongolia, which coincide with the maximum surface winds. It can be concluded that during strong winds the physically-based and the simple schemes show good agreement in DOT spatial patterns because surface winds are the dominant driving factor. Over regions where surface winds are weaker (in this case in the Taklamakan and Gurban Tunggut), the three schemes tend to disagree because the land surface parameters start to play an equal role with the meteorological parameters during the dust emission process.

An useful tool to investigate the similarity in the temporal behavior between two variables x and y is the sample cross-correlation coefficient at lag k, which is defined as

$$r_{xy}(k) = \frac{\sum_{i=1}^{N-k}(x_i - \bar{x})(y_{i+k} - \bar{y})}{\sigma_x \sigma_y}$$

where $\bar{x}$ and $\bar{y}$ are the mean, and σ_x and σ_y are the standard deviations of x and y.

Analysis of the autocorrelation at lag k can be used to determine the characteristic time over which there are no significant changes in a variable x

$$R_x(k) = r_{xx}(k)$$

In order to investigate the temporal DOT differences, we calculated the cross- correlation at lag zero for each pair of schemes. Figure 47 shows the correlation maps at lag 0 hours between the three schemes. The figure confirms that over Inner Mongolia and along the mid-range transport route downwind, the schemes show high positive correlation, because these areas are primarily affected by the strong winds and dust emission from the Gobi. Over the Taklamakan and Gurban Tunggut deserts, and the areas that are affected by

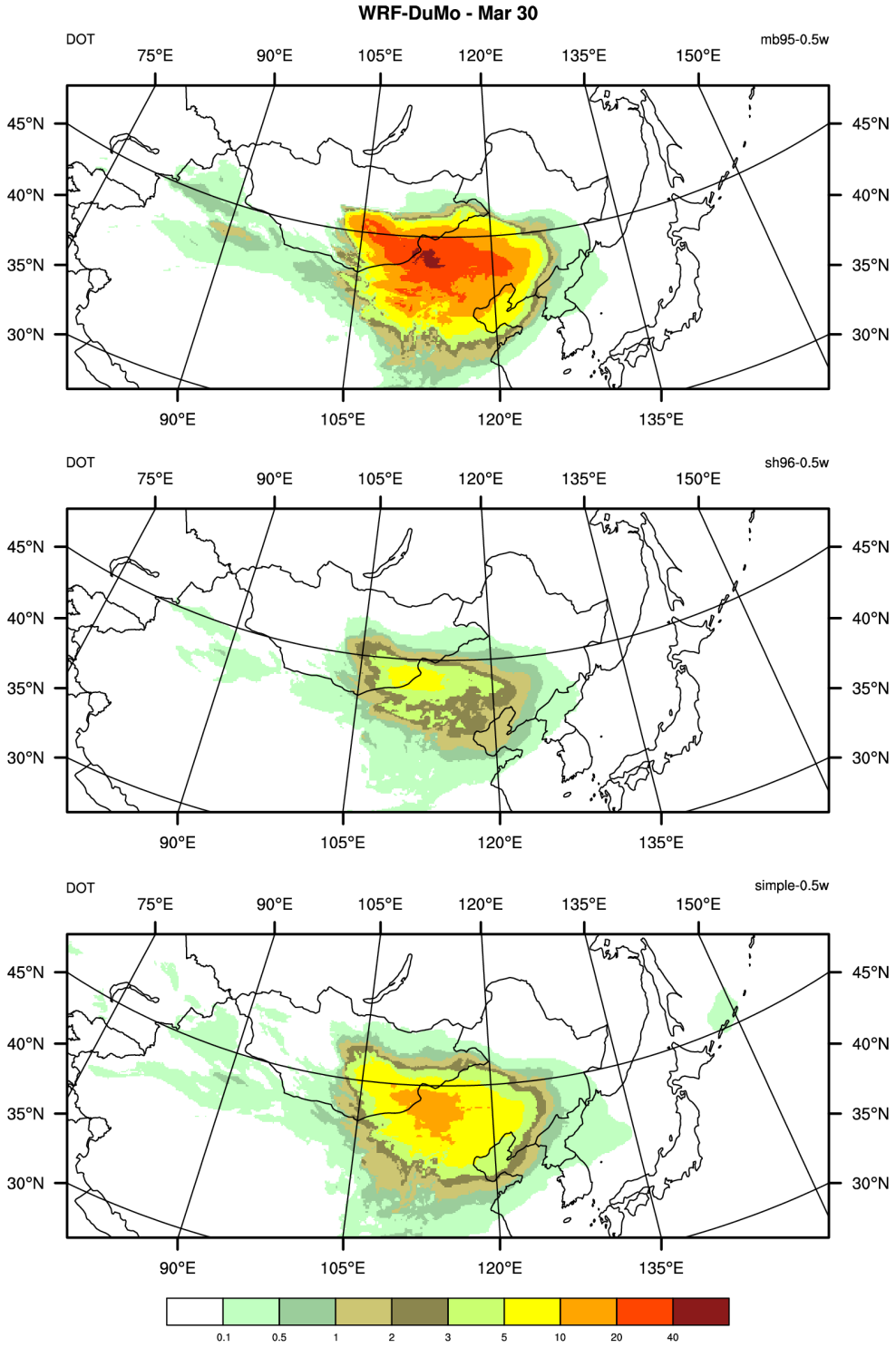

Figure 44: Daily DOT on March 30, 2007 calculated with MB95 (top), Shao96 (middle) and simple scheme (bottom).

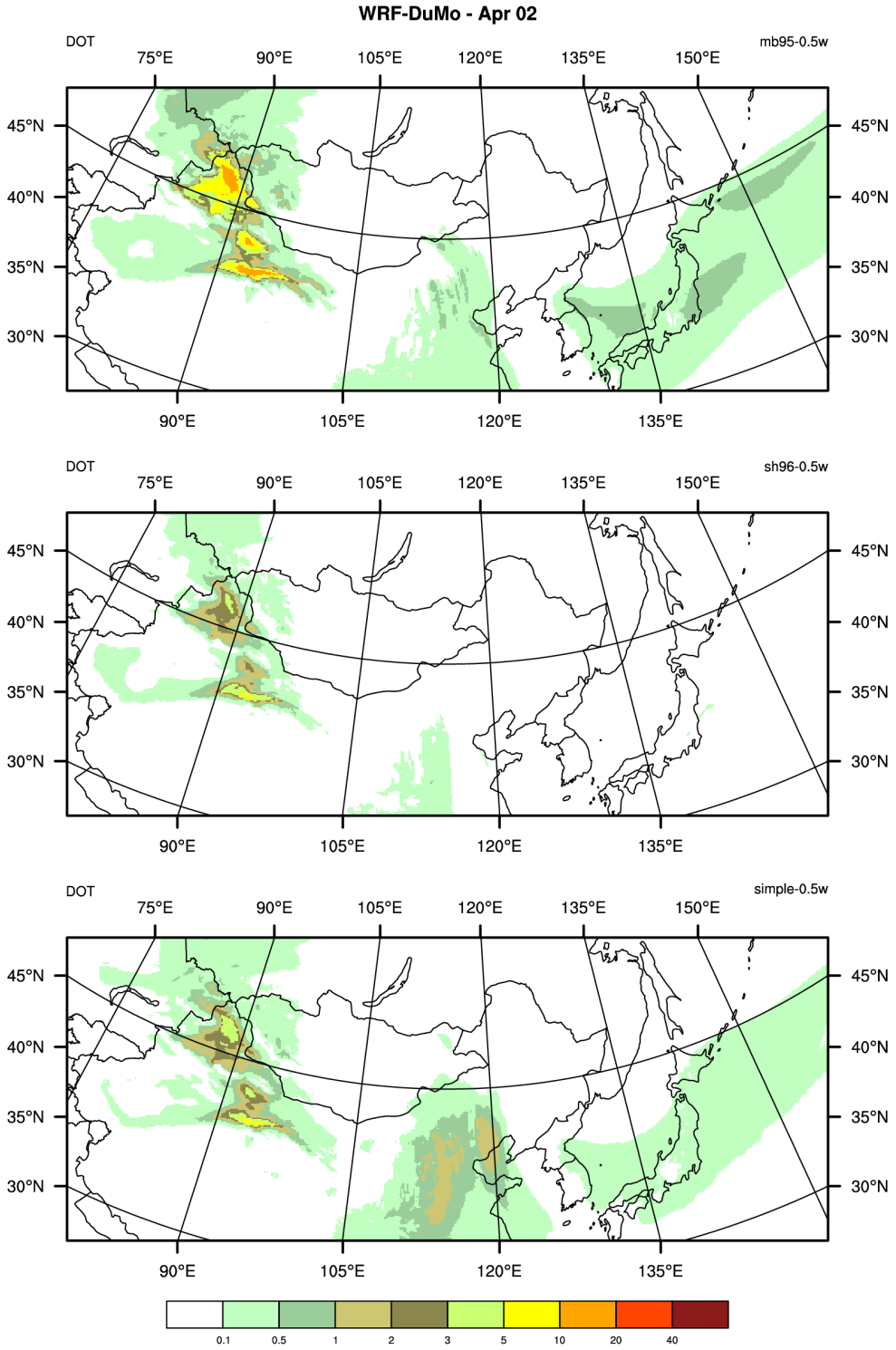

Figure 45: Daily DOT on April 2, 2007 calculated with MB95 (top), Shao96 (middle) and simple scheme (bottom).

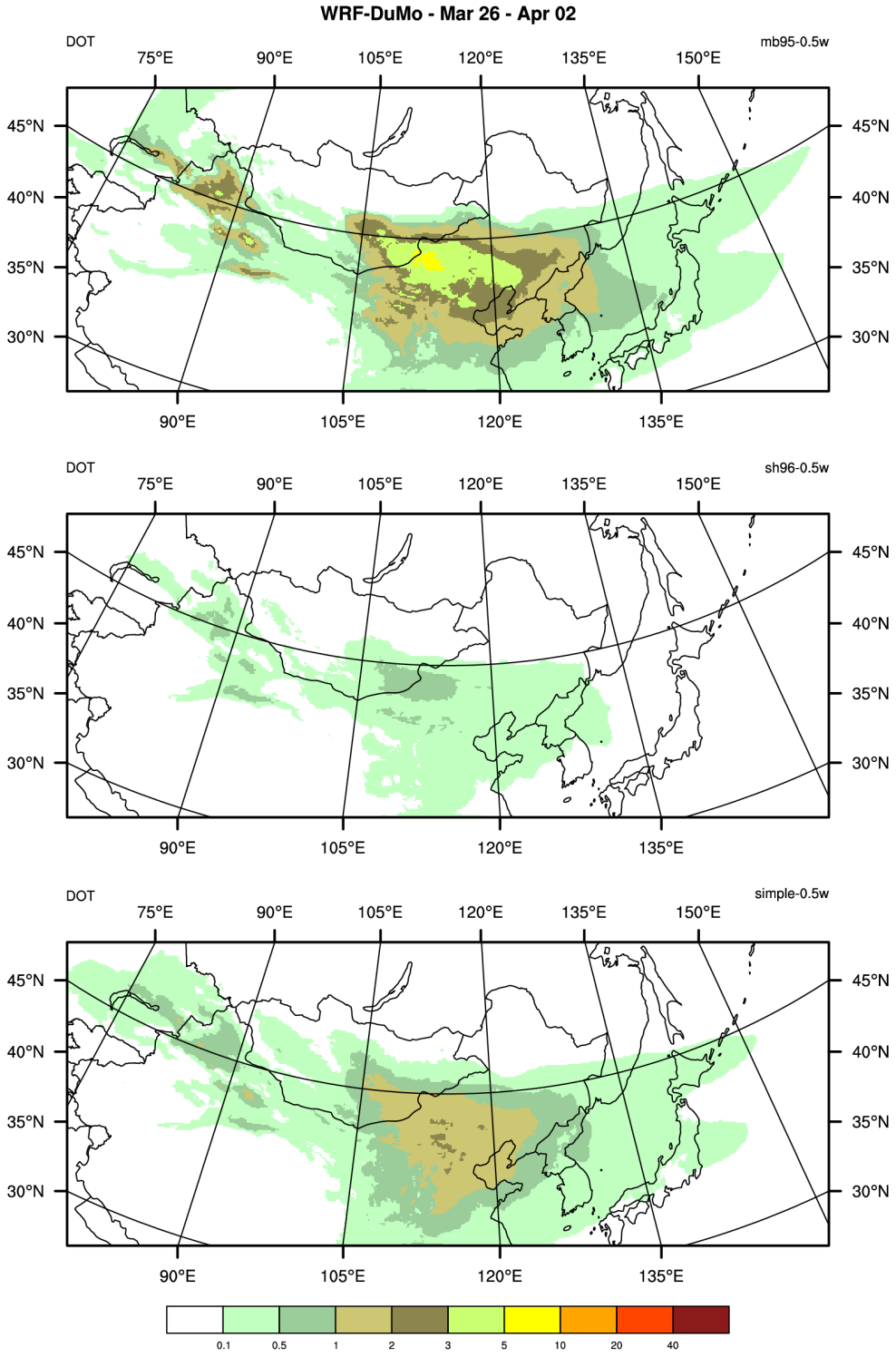

Figure 46: Mean DOT for the period 26 March – 2 April, 2007 calculated with MB95 (top), Shao96 (middle) and simple scheme (bottom).

dust originating in these sources, the correlation is highly variable. These differences can be attributed to the different onset of dust emission predicted by the schemes.

Figures 48 and 49 show the DOT autocorrelation for the three schemes at lag 3 and 6 hours, respectively. At lag 1 hour (not shown), the autocorrelation is high, especially over the areas with high dust loadings. Over the Taklamakan, however, even at lag 1 hour, the autocorrelation tends to be in the range 0.5–0.8 for MB95 and Shao96 schemes, while the simple scheme has areas with zero and negative autocorrelation values. At lag 3 hours, the autocorrelation decreases to about 0.5–0.7, indicating that 3 hours is close to the characteristic time over which DOT responds to the emission and removal processes. At lag 6 hours, the autocorrelation decreases further, and the large part of the domain shows close to zero and negative autocorrelation values.

The short time period of about 3 hours over which a significant decrease in the autocorrelation was found suggests that the common practice of generating global daily AOT products from near instantaneous AOT granules, retrieved from polar orbiting satellites, may introduce large errors, especially if the global AOT product is used over large geographical areas. In the case of MODIS, each granule consists of data collected from a 5 minutes swath along the ground track. Any adjacent 5min MODIS granules are at most separated by the time it takes the satellite to make full circle around the Earth, which is about 100 minutes, and according to our analysis it should be safe to use composite up to three granules wide (across the satellite track). However, it takes MODIS about 9 hours to cover our domain, and therefore, the assumption on time coherency of the observational data cannot be satisfied over the whole domain. Quantitative comparison between AOT retrieved from near polar orbiting satellite and modeled DOT is best to be done for individual granules. The short overpass time and the limited diurnal coverage of a polar orbiting satellite make it impossible to confirm the 3 hours over which the assumption about the temporal coherency of the AOT breaks. However, the time coherency of the modeled DOT can be validated with AOT retrieved from geostationary satellites, which offer a temporal

resolution up to 15 minutes.

4.4.2 Correlation analysis of modeled visibility fields

Modeled visibility on 30 March and 2 April, 2007 at 3 UTC is shown in Figures 50 and 51. Significant differences in the absolute values and the spatial patterns are observed on both days. The MB95 scheme produces the lowest visiblity, followed by the simple and the Shao96 scheme. This result is consistent with the DOT fields. Close comparison of the spatial patterns of DOT (Figures 40, 41 and 44) and visibility (Figure 50) calculated with the three dust emission schemes show overall agreement on 30 March - contours with low visibility overlap with the contours of high DOT. However, it is also apparent that DOT fields are smoother than the visibility field and the maximum DOT does not coincide exactly with the minimum visibility. Similar behavior of the two fields - DOT (Figure 45) and visibility (Figure 51) was also observed on 2 April. Figures 44 and 50 show that over certain regions (Taklamakan, Gurban Tunggut) the visibility is less than 5 km, while the DOT is between 0.1 and 0.5. This implies that dust is primarily located in the surface layer. In contrast, Figures 45 and 51 show DOT between 0.5 and 1 to the northeast of Japan, while the modeled visibility is above 50 km, which is indicative of an elevated dust layer not contributing to visibility reduction.

Similarly to DOT fields, we analyze the temporal visibility differences in terms of the cross-correlation at lag zero calculated for each pair of schemes. The visibility cross-correlations (Figure 52) show more variability over land compared to the DOT cross-correlations. Along the transport route, there is a high correlation, in particular between the visibility from MB95 and Shao96 schemes. Over the land, with the exception of the Gobi region, we see lower visibility correlation compared to the DOT correlations. Visibility depends on the dust concentration in the first model layer and is controlled by the dust emission and deposition, while the DOT is related to the dust mass in the entire atmospheric column. It is expected that the visibility magnitude, being directly related to dust emission

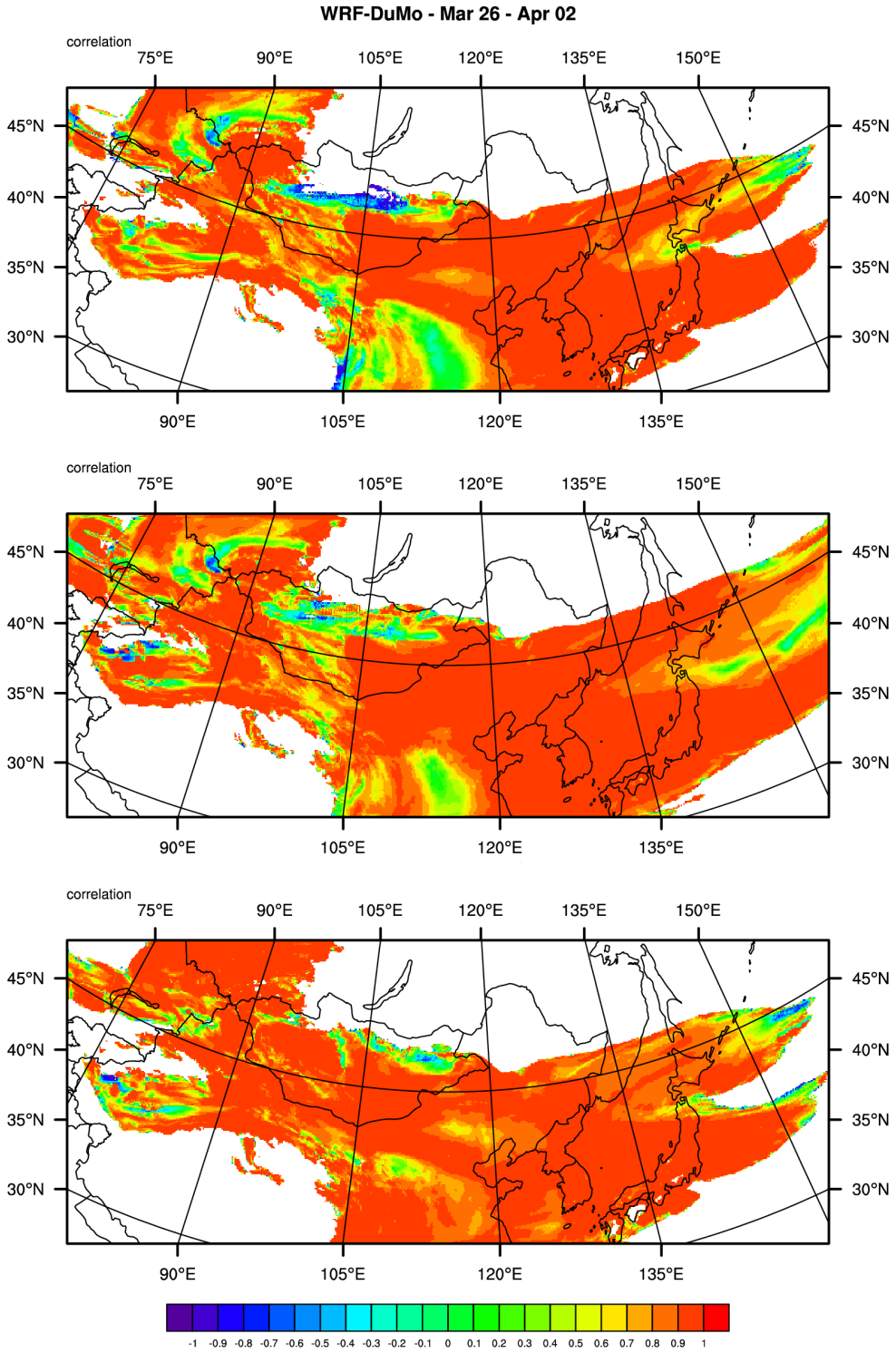

Figure 47: DOT correlation map at lag 0 between MB95 and Shao96 (top), MB95-simple (middle) and Shao96-simple (bottom).

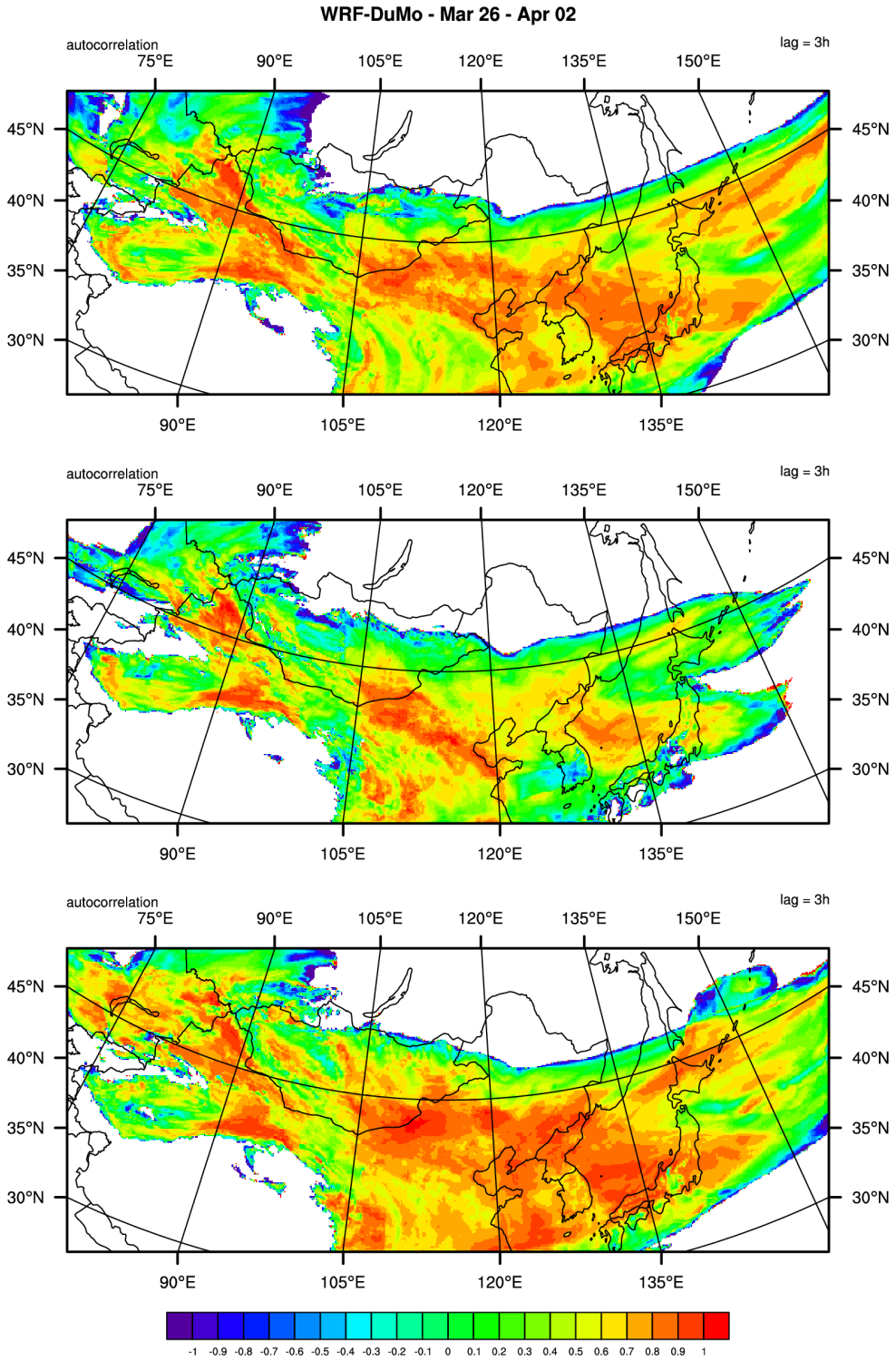

Figure 48: Autocorrelation map of DOT at lag 3h for MB95 (top), Shao96 (middle) and simple (bottom).

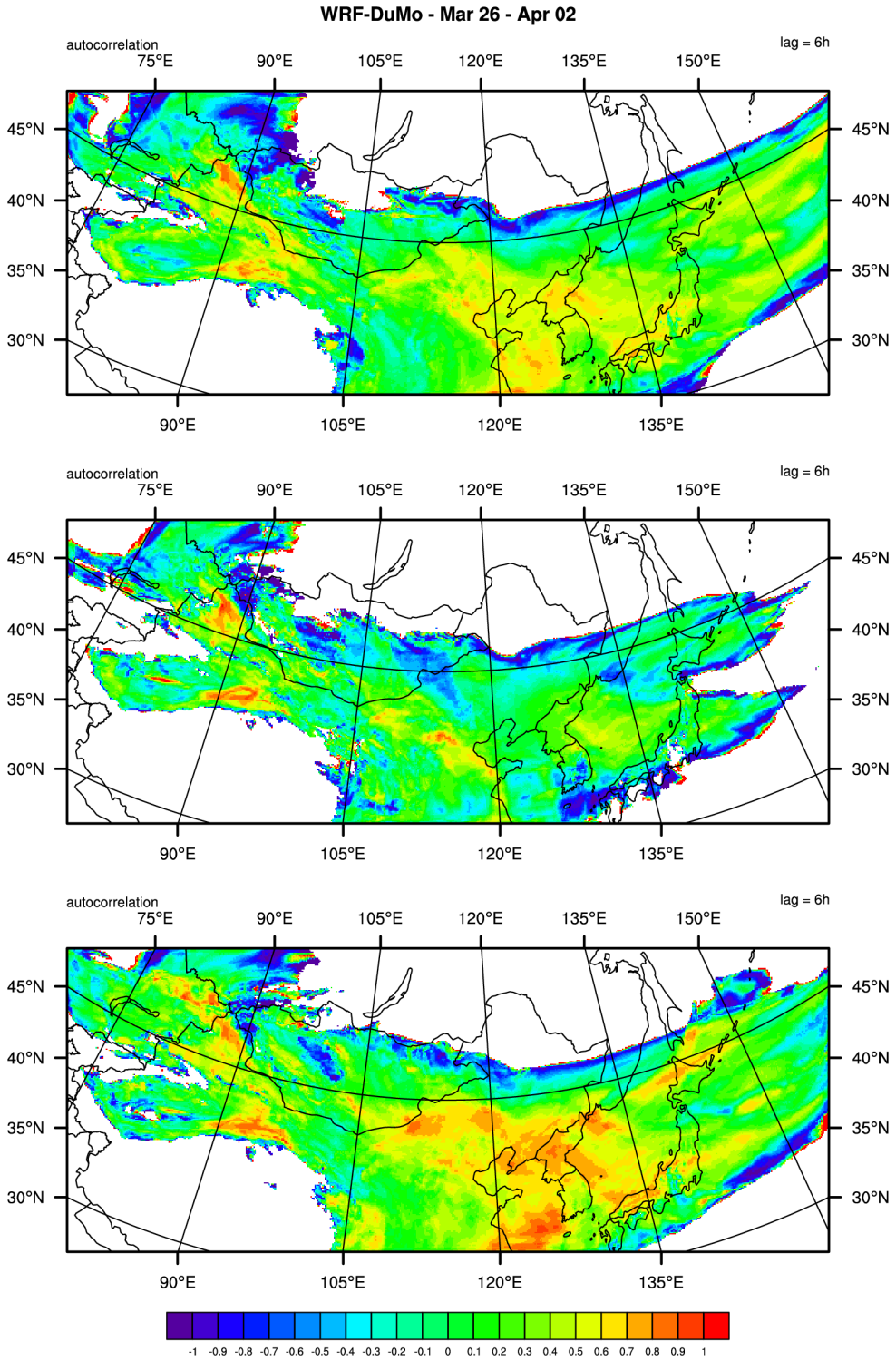

Figure 49: Autocorrelation map of DOT at lag 6h for MB95 (top), Shao96 (middle) and simple (bottom).

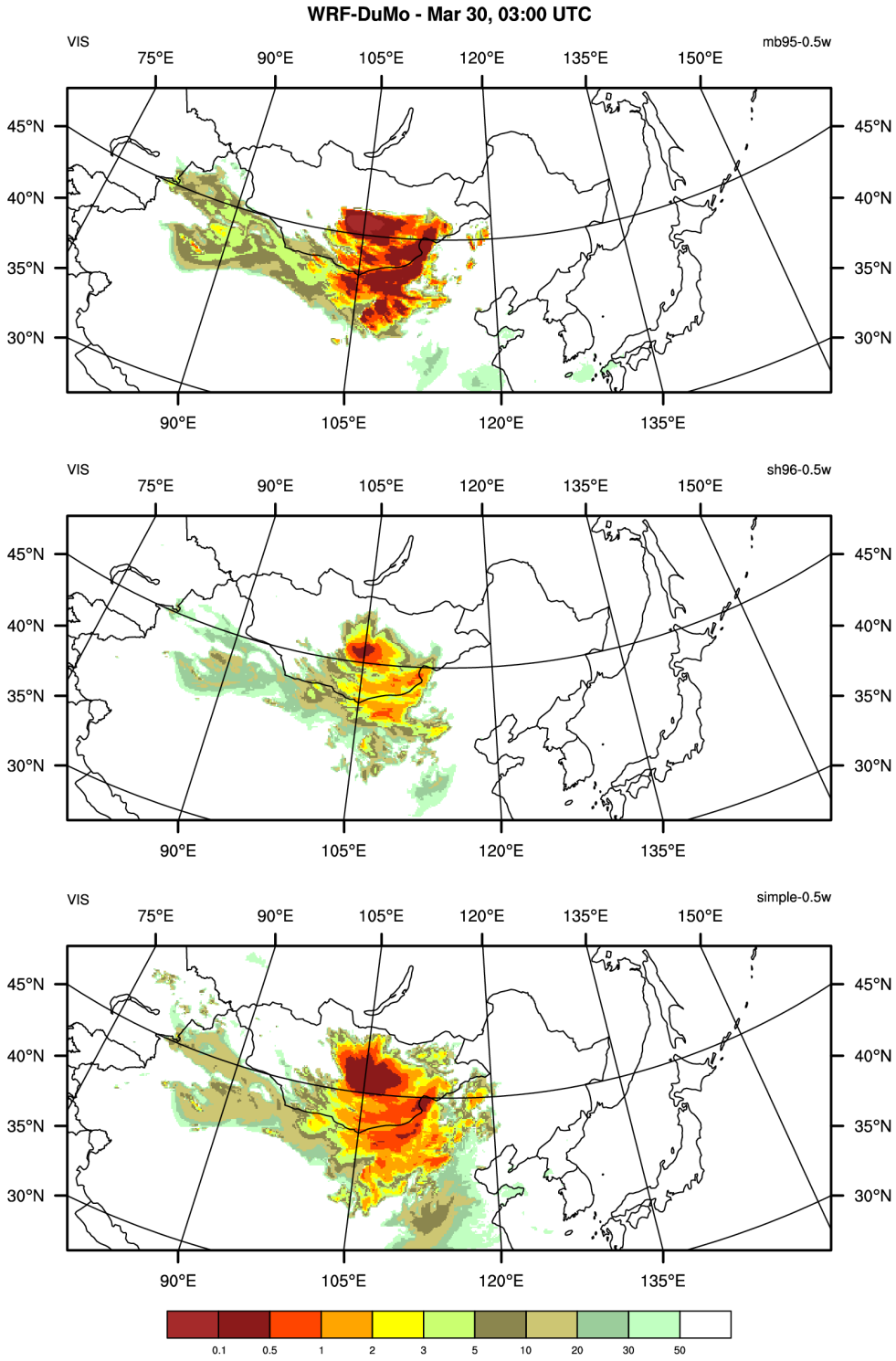

Figure 50: Visibility (in km) on 30 March, 2007 3UTC calculated with MB95 (top), Shao96 (middle) and simple scheme (bottom).

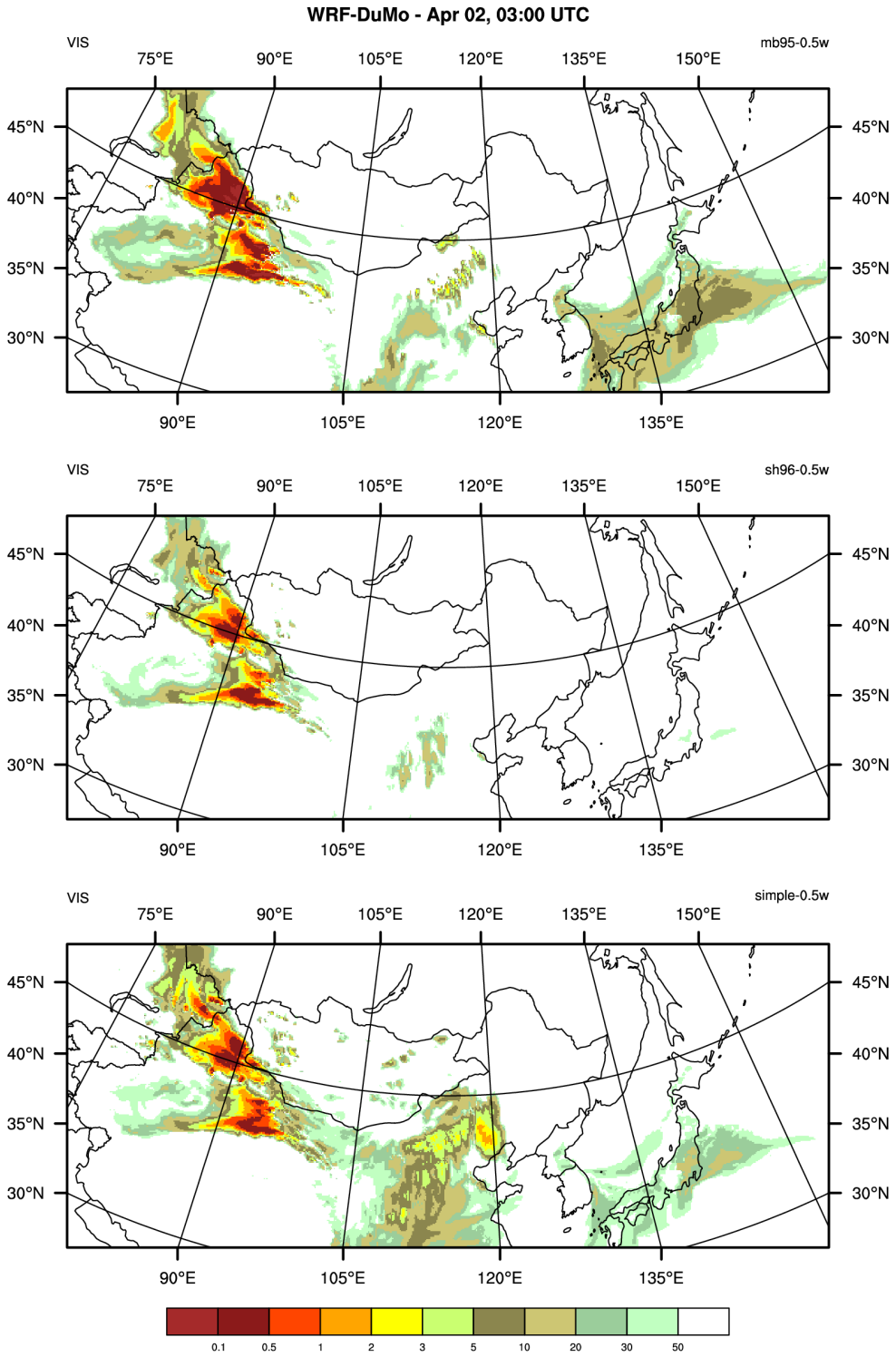

Figure 51: Visibility (in km) on 2 April, 2007 3UTC calculated with MB95 (top), Shao96 (middle) and simple scheme (bottom).

strength, will be strongly affected by the choice of the dust production scheme. As already shown (Figures 44 and 45), the patterns of DOT are smoothed out during the transport and deposition processes, thus DOT patterns bare weaker dependence on dust emission parameterizations. We can conclude that reliable visibility measurements may be more beneficial in constraining dust production schemes than AOT observations.

Figures 53 and 54 show the visibility autocorrelation for the three schemes at lag 3 and 6 hours. Interestingly, at lag 1 hour (not shown) the visibility autocorrelation is not as high as the DOT autocorrelation. Lower autocorrelations mean higher temporal variability in the visibility calculated with the three schemes. This confirms that visibility fields are more inhomogeneous compared to the DOT fields because the former are more affected by intermittent and highly variable dust emission process, especially in the sources. At lag 3 hours the autocorrelation decreases bellow 0.5, indicating that the characteristic time over which visibility responds to the emission and removal processes is less than 3 hours, and can be in the order of one hour. At lag 6 hours the autocorrelation decreases further and is close to zero or negative over the large portion of the domain.

The above results have several important implications for model validation and development of an integrated framework: 1) the DOT autocorrelation starts to decrease significantly after 3 hours, which can be regarded as the characteristic time over which DOT responds to the emission and removal processes. This finding may prove useful in comparing observations and modeling at different time intervals. 2) Smaller visibility autocorrelations show higher sensitivity to dust emission parameterizations. This means that accurate visibility measurements can be used to constrain dust emission fluxes and their spatiotemporal patterns better than AOT measurements. 3) High spatial variability of the modeled visibility means that one needs to be careful with interpolating the visibility from meteorological stations. Also, it is better to use the point observations for the purpose of comparison with the modeled visibility or data assimilation, rather than interpolating observations from the limited number of stations over the large model domain.

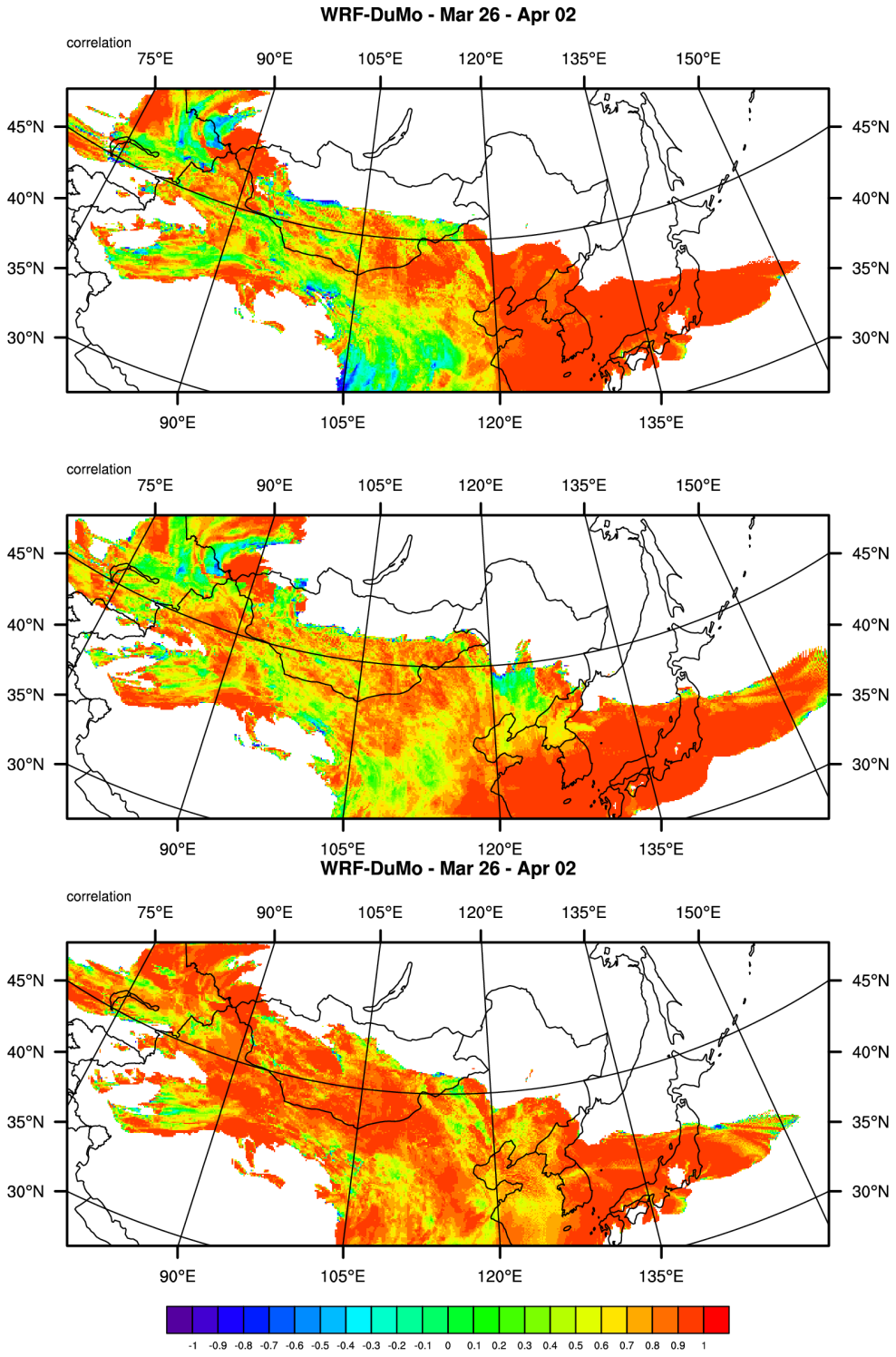

Figure 52: Visibility correlation map at lag 0 between MB95 and Shao96 (top), MB95-simple (middle) and Shao96-simple (bottom).

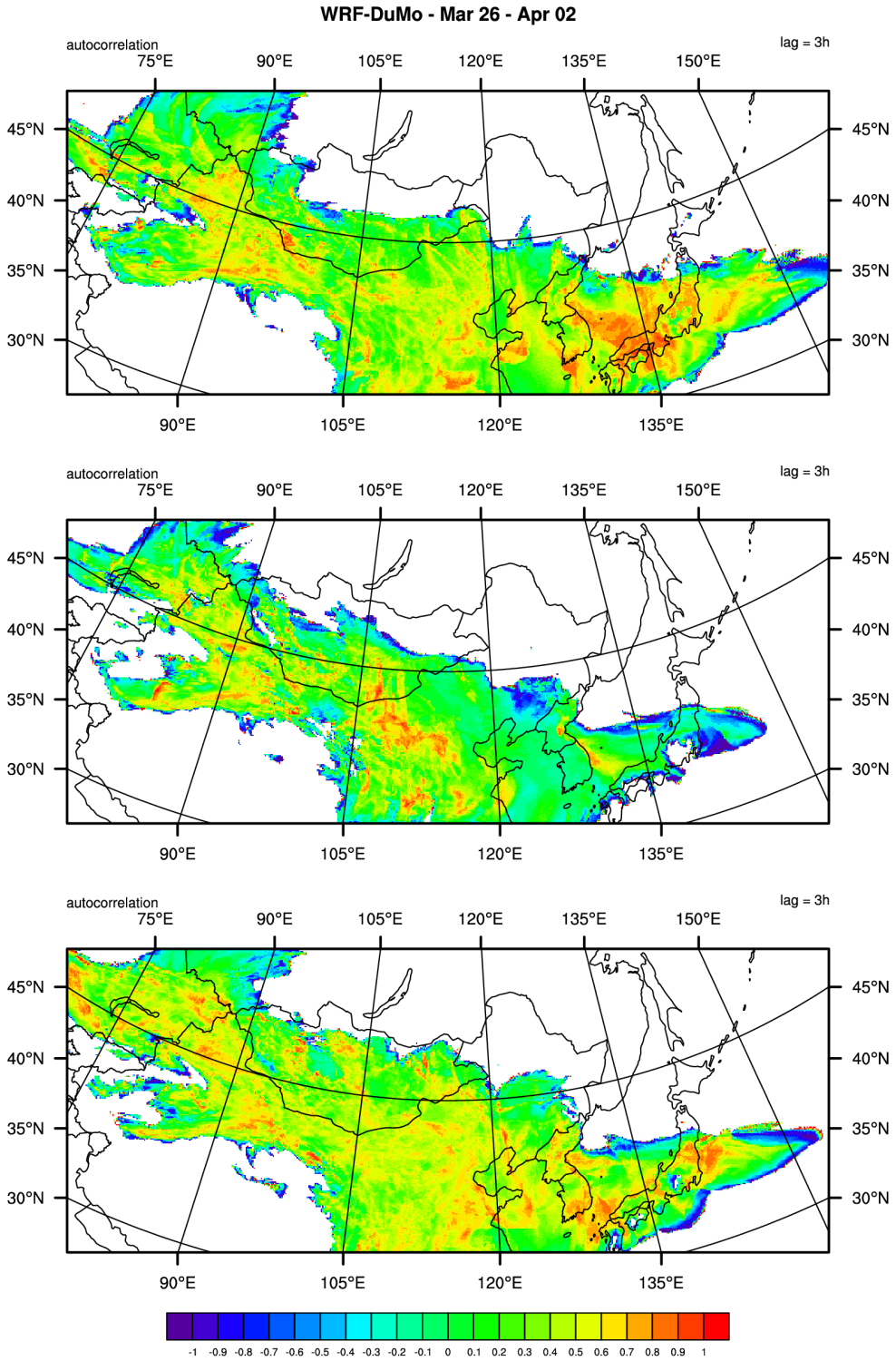

Figure 53: Autocorrelation map of visibility at lag 3h for MB95 (top), Shao96 (middle) and simple (bottom).

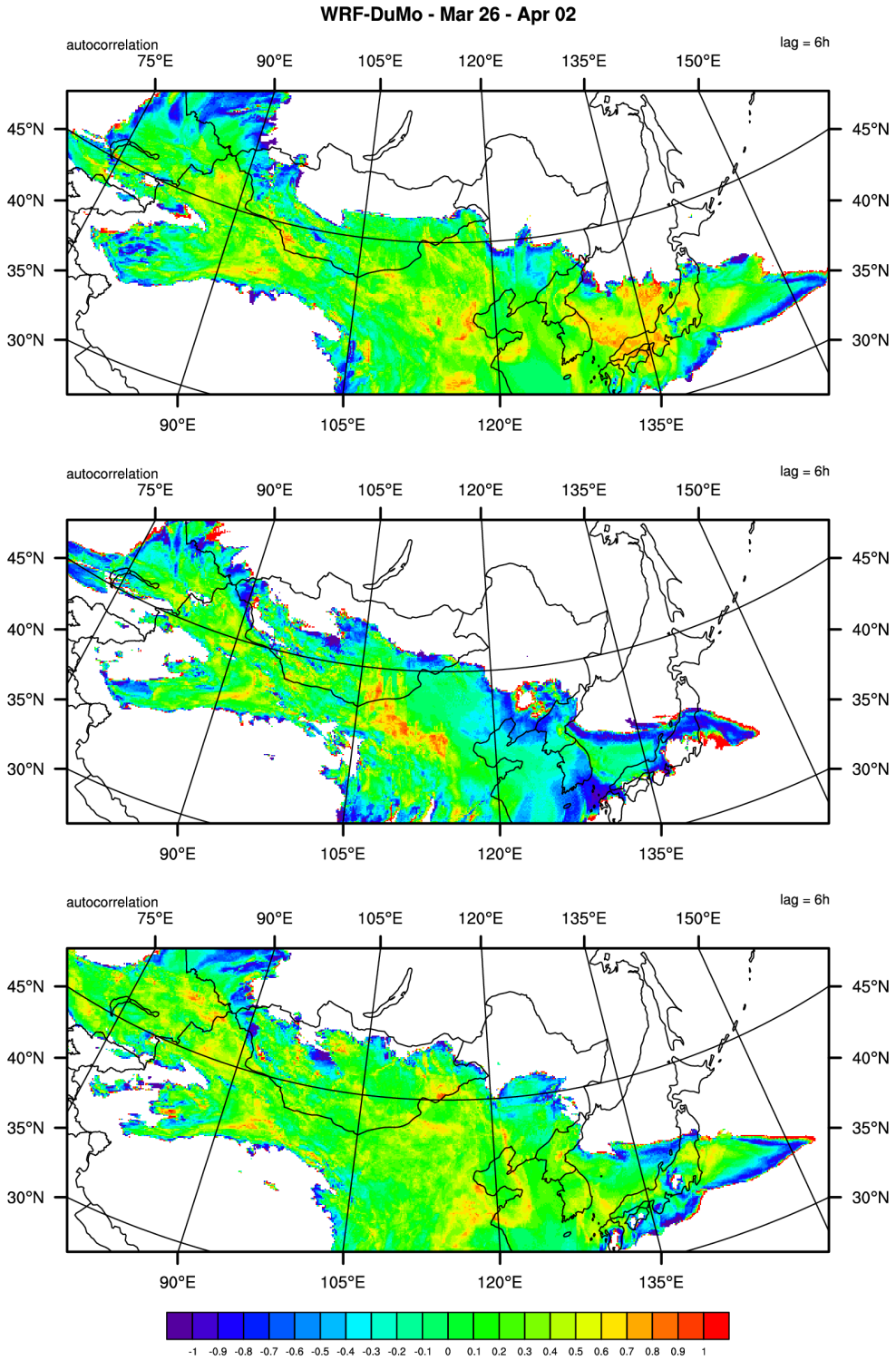

Figure 54: Autocorrelation map of visibility at lag 6h for MB95 (top), Shao96 (middle) and simple (bottom).

4.5 Validation of WRF-DuMo against observations

4.5.1 Comparison of modeled DOT with MODIS AOT

To validate the modeled DOT against observations, we compared the daily averaged DOT (Figures 44 and 45) against AOT retrieved from MODIS-Aqua. To facilitate the intercomparison, we created composites of MODIS-Aqua AOTs for the period 30 March – 2 April, 2007 (Figure 55). The AOT composites are comprised of two data sets that are provided by the MYD04_L2 product - the 'Dark Target' aerosol optical thickness at 0.55 μm for both Ocean and Land, and aerosol optical thickness based on the "Deep Blue" algorithm over land. The patchy appearance of the retrieved AOT is caused by the presence of clouds, or bad retrievals.

From the MODIS retrievals it is evident that the Taklamakan Desert was an active dust source during the period 30 March – 2 April, 2007. The retrieved AOT, with values from 0.5 to 5, indicate an increase in the dust loading as time progresses. WRF-DuMo captures this tendency. However, modeled DOTs are consistently smaller compared to the observations. This suggests that WRF-DuMo underpredicts the dust emission in the Tarim Basin. There are two possible reasons. First, this region has a complex topography and the ability of WRF to reproduce mesoscale topographically forced circulations is uncertain. The second one is that we decreased the roughness length over bare and sparsely vegetated surfaces (such as Taklamakan). Roughness length is directly related to the geometrical height of the roughness elements, e.g., grasslands and shrublands have smaller roughness lengths compared to forests. Thus, decreasing the roughness lengths (smoother surface) will decrease the friction velocity. This finding may require additional tuning of friction velocity and soil moisture over Taklamakan to be able to reproduce DOT comparable with the observations.

In contrast, over the Gobi, WRF-DuMo produces DOT much higher than MODIS AOT. Visual inspection of MODIS true color images reveals significant cloud coverage over the Gobi during the simulation period, which explains the lack of AOT measurements from MODIS. From the analysis of the true color images we also found that on 30 March there

was a clearly visible dust plume, which was not obscured by clouds. However, AOT was not retrieved over that area. The lack of AOT retrievals in this particular case suggests that the cloud-aerosol mask in the aerosol algorithm misclassified the dust as cloud. Over the Pacific Ocean, MODIS AOTs are higher than model predicted DOTs. This is likely due to overestimation of sedimentation and dry removal of dust in WRF-DuMo.

4.5.2 Comparison of modeled DOT with CALIPSO AOT

We calculated DOT closest in time with CALIPSO overpasses over the considered domain. DOTs were calculated with the two physically-based dust emission schemes and compared with CALIPSO aerosol feature optical thickness (FOT). DOT and FOT data for 30 March, 6:00UTC and 31 March, 20:20 UTC are shown in Figures 56 and 57, respectively. The CALIPSO transect is shown as a solid black line on the maps. The 30 March CALIPSO pass coincides with a very strong dust event in the Gobi Desert, as it is seen from the high DOTs modeled with both MB95 and Shao96 schemes. The intense dust emission is also confirmed by the MODIS-Aqua AOT retrievals (Figure 55) and the resulting high AOT values in the following days along the transport route. Clouds obscured a large part of the path, and the lidar signal was totally attenuated according to the vertical feature mask (VFM) making FOT retrieval impossible, including the area with the largest DOT predicted by WRF-DuMo. Modeled DOTs are in a good agreement with CALIPSO retrievals over a very small section of the transect, in particular, between 39N; 109E and 37N; 110E. On can also see that MB95 produces about 7 times higher DOT compared to the Shao96 scheme, and its maximum DOT exceeds 100, indicating a significant overestimation of the dust load. The next opportunity to compare WRF-DuMo with CALIPSO was on 31 March at 20:20 UTC when CALIPSO passed over the Taklamakan. According to the CALIPSO feature mask there were no clouds to obstruct the aerosol retrievals. Both schemes produced DOTs that are in a very good agreement with CALIPSO FOT.

On 2 April, 16:40 UTC, CALIPSO passed over the dust plume at a time when it was

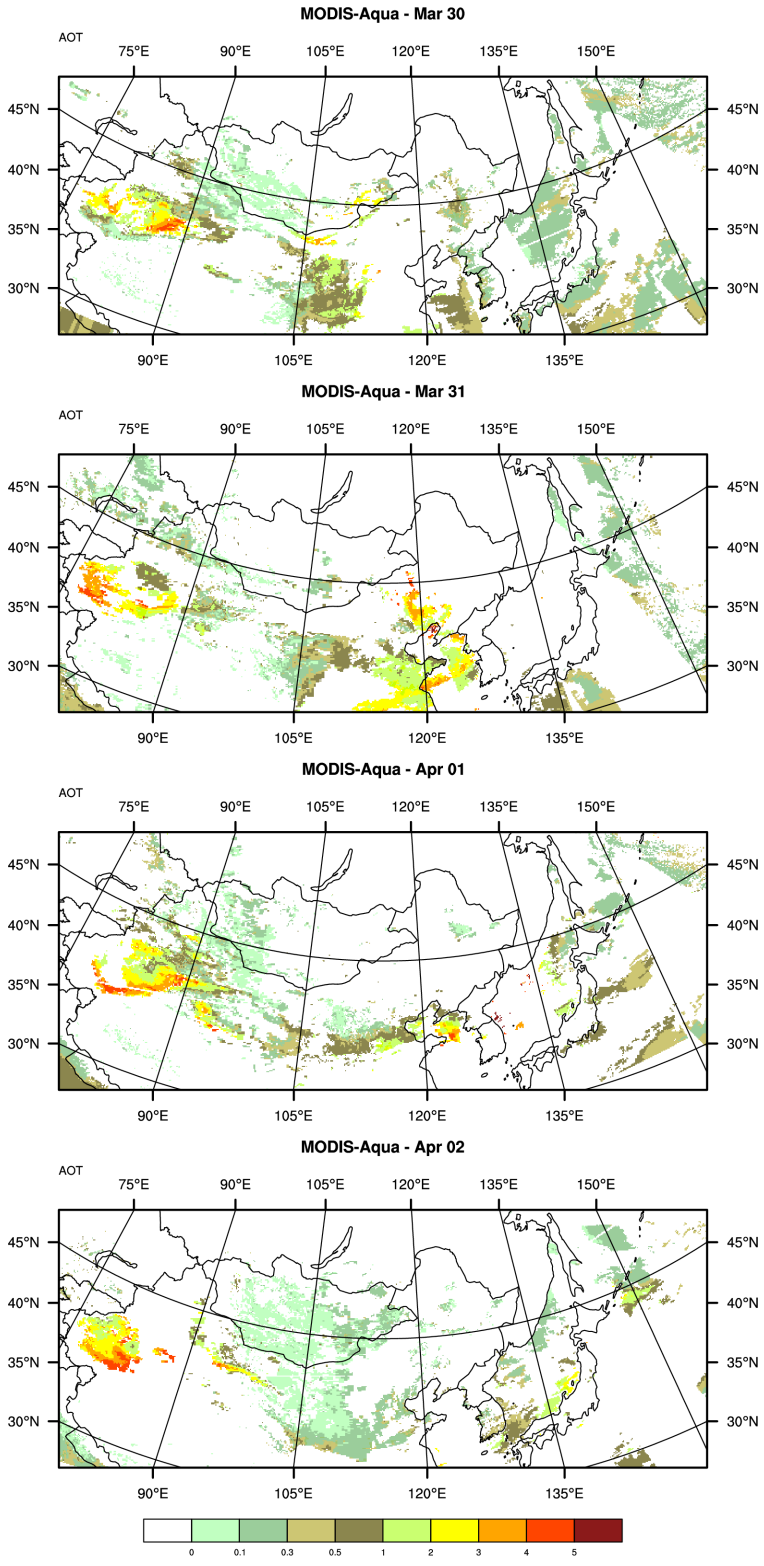

Figure 55: MODIS-Aqua AOT composite for 30 March 30 – 2 April, 2007. AOT data is comprised of two MYD04_L2 datasets - optical depth over land and ocean, and "Deep Blue" optical depth over land.

already transported to the northeast of Japan (Figure 58). One can see that the higher MB95 dust loadings over land compared to those calculated with the Shao96 scheme result in DOT over Japan in the range of 0.1-1, while the Shao96 scheme practically shows no dust loading (DOT below 0.1) present at that time and location. CALIPSO VFM shows that the dust plume extends vertically above 6km. Again, we see that clouds attenuate the lidar signal and a very small section of the CALIPSO transect contains FOT data, from which we see that WRF-DuMo underestimates the dust loading, especially the Shao96 scheme.

Our comparison against MODIS-Aqua AOT and CALIPSO FOT data suggests that WRF-DuMo shows pronounced biases in the modeled DOT. Over the land, the aerosol optical depth is systematically underestimated in the Tarim Basin and significantly overestimated over the Gobi Desert, while the mid-range transport shows underestimation of the dust loading. This can be explained by an underestimation of the dust emission in the Taklamakan and by an overestimation in the Gobi Desert. Excessive dry removal along the mid-range transport might also be a factor. We also observed significant cloud cover, which affects the aerosol retrievals and thus creating a challenge for merging the datasets. On the other hand, the lack of aerosol retrievals in the presence of clouds clearly shows the need of an integrated approach in order to create a complete picture of the dust fields.

4.6 Towards an integrated observational and modeling dust framework

As a proxy for the presence of dust, we introduce a model dust index, DI_{DOT}, which is defined by setting a threshold background DOT_{bg} value:

$$DI_{DOT} = \begin{cases} 0 & DOT \leq DOT_{bg} \\ 1 & DOT > DOT_{bg} \end{cases} \tag{32}$$

Equation 32 can be applied to either instantaneous or time averaged DOT fields. Furthermore, the model DI definition can be easily extended in the case of an ensemble of N modeling experiments, where each experiment (or model run) is defined by a unique set up

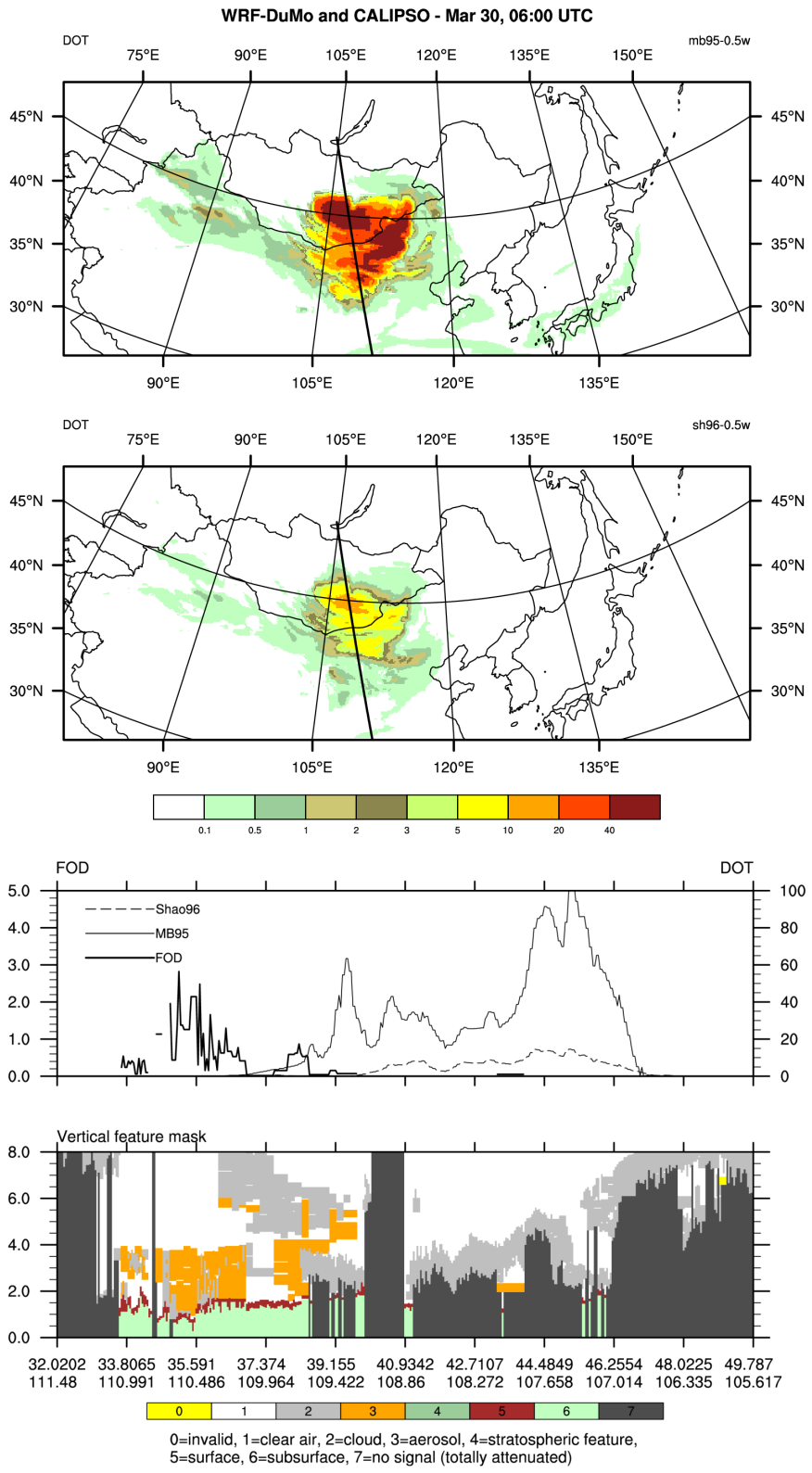

Figure 56: DOT maps for MB95 (top) and Shao96 (middle). Shown are also CALIPSO FOT and VFM, and modeled DOTs along the CALIPSO path (bottom) on 30 March, 2007 6:00UTC. CALIPSO path is shown on the maps as a solid black line.

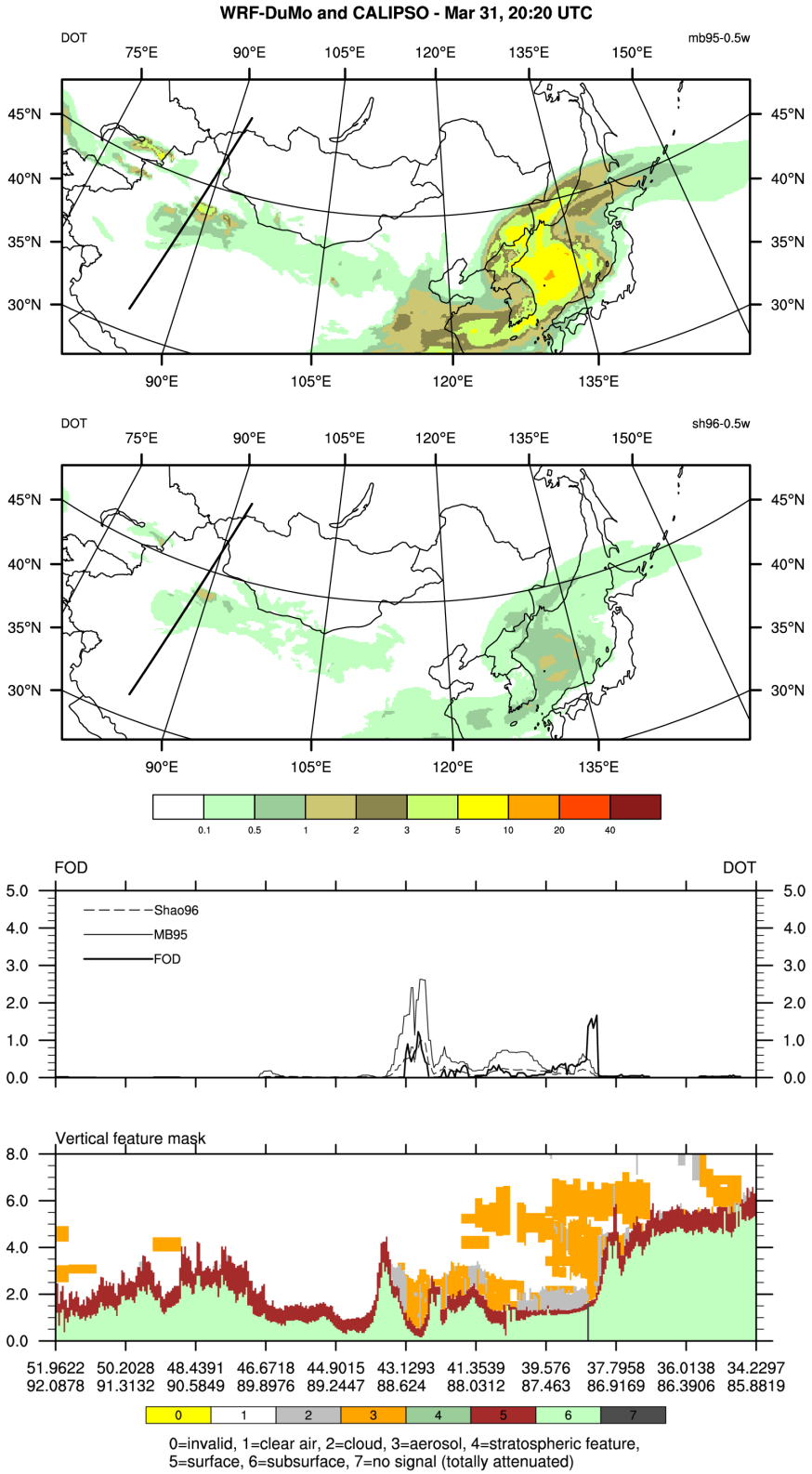

Figure 57: Same as Figure 56, except for 31 March, 2007 20:20UTC.

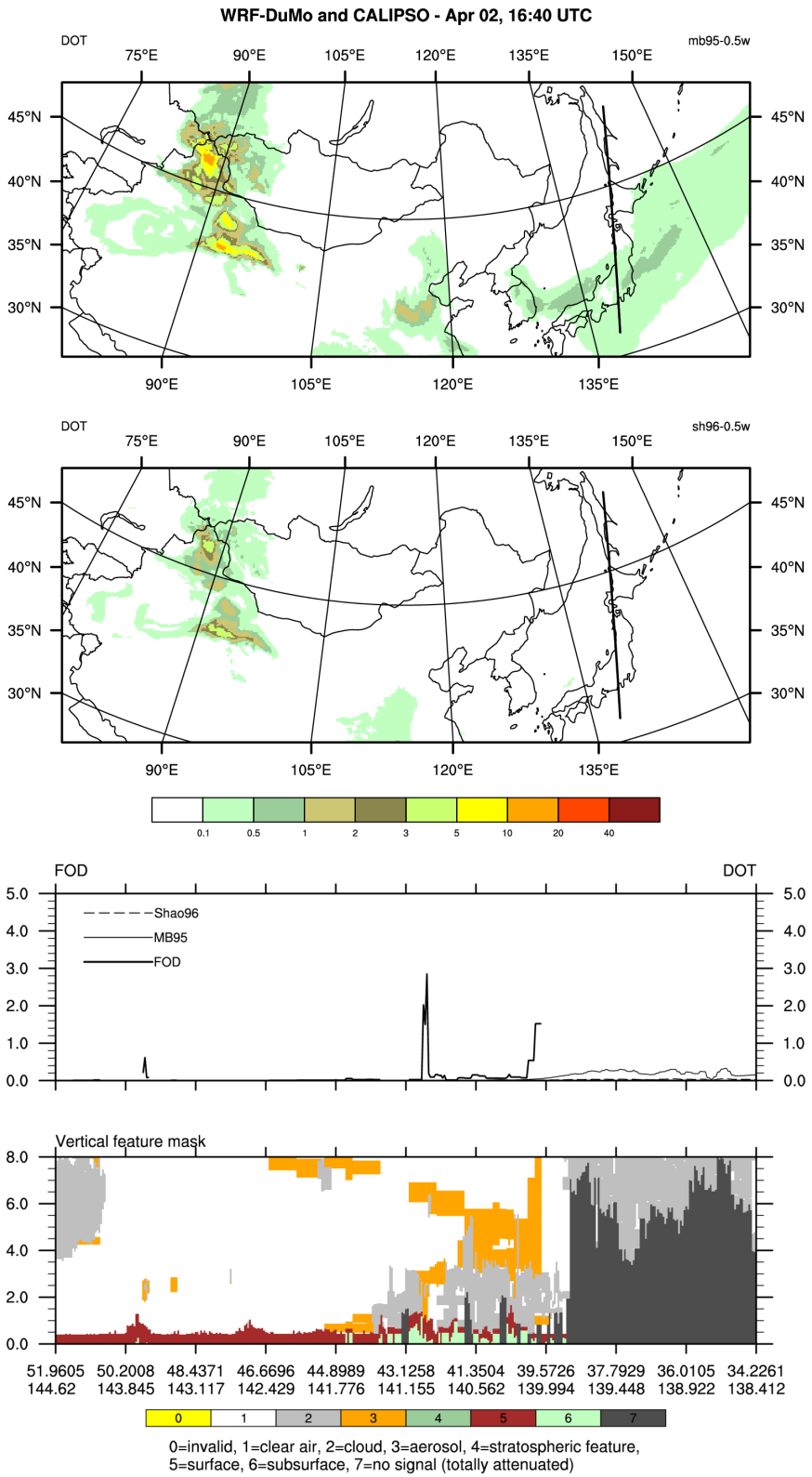

Figure 58: Same as Figure 56, except for 2 April, 2007 16:40UTC.

of the dust modeling system:

$$DI_{DOT} = \sum_{i=1}^{N} \mu_i DI^i_{DOT} \tag{33}$$

where the index i denotes the ith experiment with dust index DI^i_{DOT} calculated using Equation 32, and the weights μ_i that are assigned to each experiment sum to unity. If the experiments are equally well representative, their weights are the same, and Equation 33 becomes

$$DI_{DOT} = \frac{1}{N} \sum_{i=1}^{N} DI^i_{DOT} \tag{34}$$

The modeled dust index values are in the interval [0, 1], with 0 indicating that none of the experiments satisfies the criterion for dust presence, and 1 indicating that all of the experiments predict the presence of dust, or in the other words, when $DI = 0$ there is 100% agreement that dust is not present (0% that it is present) and when $DI = 1$ there is 100% agreement that dust is present. If one defines the agreement Q_{DOT} for dust to be present as the percentage of the experiments with DI equal to 1, then

$$Q_{DOT} = \frac{1}{N} \sum_{i=1}^{N} DI^i_{DOT} \times 100\% \tag{35}$$

Comparing Equations 34 and 35 reveals that there is a direct linkage between the experiments agreement and the ensemble dust index when the experiments are weighted equally:

$$Q_{DOT} = DI_{DOT} \times 100\% \tag{36}$$

and therefore Q_{DOT} can be interchangeably used with DI_{DOT}.

Similarly to DOT, one can introduce a dust index based on visibility, that is, a criterion for dust presence will be defined by introducing a background visibility VIS_{bg}

$$DI_{VIS} = \begin{cases} 0 & VIS \geq VIS_{bg} \\ 1 & VIS < VIS_{bg} \end{cases} \tag{37}$$

or in the case of multiple experiments

$$DI_{VIS} = \sum_{i=1}^{N} \mu_i DI^i_{VIS} \tag{38}$$

Equations 35 and 36 are also applicable if one substitutes DI_{DOT} with DI_{VIS}. There is an important difference, however, between these indexes. While DI_{DOT} reflects the conditions throughout a vertical column in the atmosphere, DI_{VIS} reflects the conditions at the surface. Also, low DI_{VIS} implies high DI_{DOT} but not vice versa. To illustrate the two model derived indexes we calculated DI_{DOT} from the daily averaged DOT for the three dust production schemes, using value of 0.1 (typical value for clean conditions) for DOT_{bg}. DI_{VIS} was calculated in a similar manner using VIS_{bg} of 10 km. Modeled DI_{DOT} and DI_{VIS} for the period 30 March – 2 April, 2007 are shown in Figures 59 and 60 respectively. On 30 March, 2007 the DI_{DOT} and DI_{VIS} patterns are somewhat similar, because both DOT and visibility are controlled by the ongoing emission mainly from Gobi. However, after the emission decreases, at surface level the visibility decreases, while the DOT remains high, because of the remaining dust mass in the atmosphere.

Here the definition of the model dust index is based on a simple step function. One can certainly employ a different function, e.g., a linear function between 0 and DOT_{bg} with corresponding values of 0 and 1. However, we are generally interested in values of DOT exceeding the DOT_{bg}, and we do not expect the criterion function to significantly affect the DI when DOT is close or exceeds DOT_{bg}. Despite its simplicity, DI_{DOT} can be used to aid satellite retrievals especially over land or in the presence of clouds when the detection of dust is a challenging task.

4.6.1 Integration of WRF-DuMo with observations

OMI-AI is more robust compared to MODIS AOT, especially over land and in the case of high dust loadings (see Chapter 3). Being a qualitative parameter and a good proxy for the presence of dust, OMI-AI is a good candidate to investigate how one can approach the problem of integrating WRF-DuMo simulations with observations to achieve improved capabilities of dust field characterization.

OMI-AI is reported as global-daily averaged product at a 1×1 degree spatial resolution.

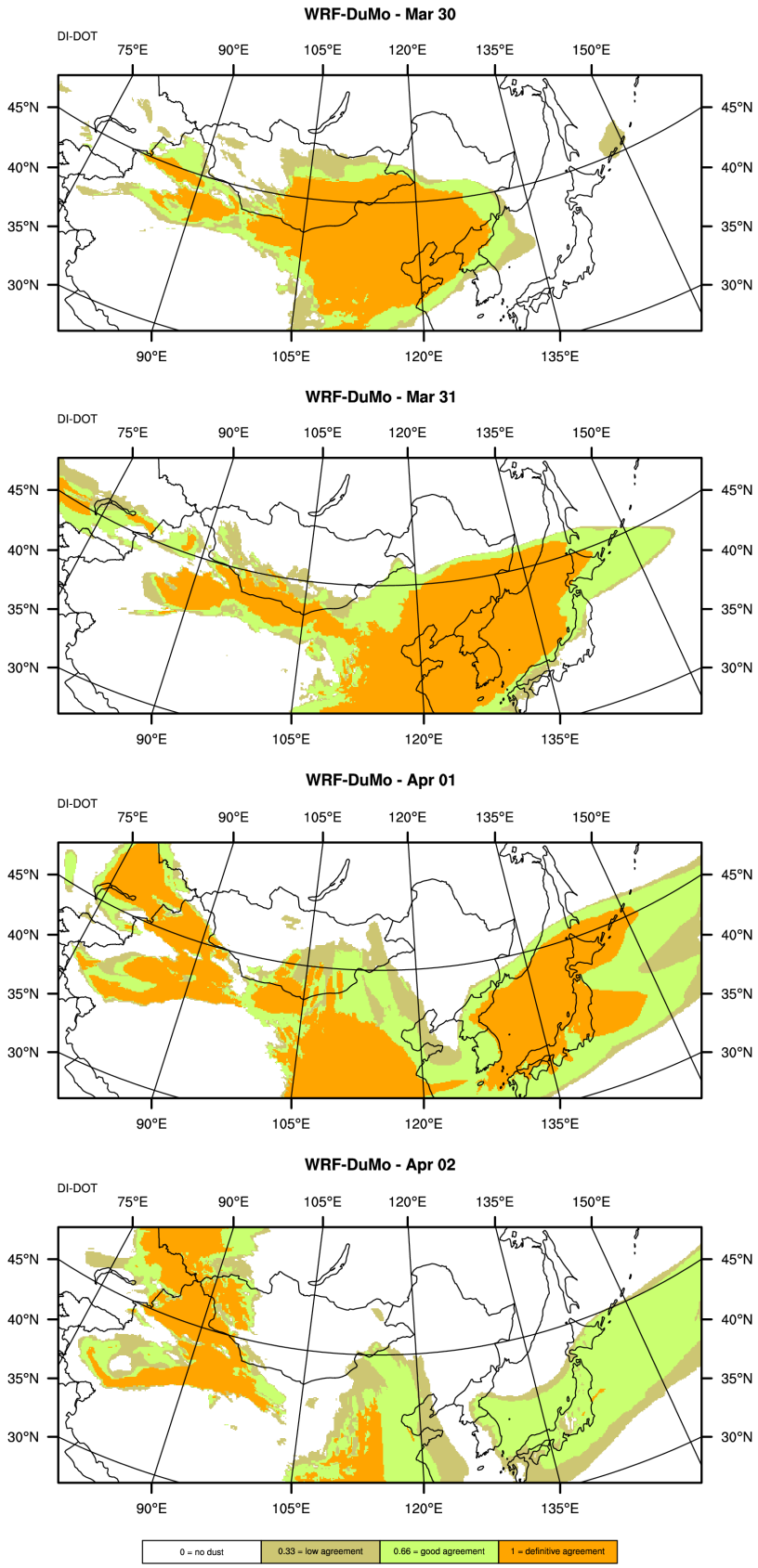

Figure 59: DI_{DOT} for the period 30 March – 2 April, 2007.

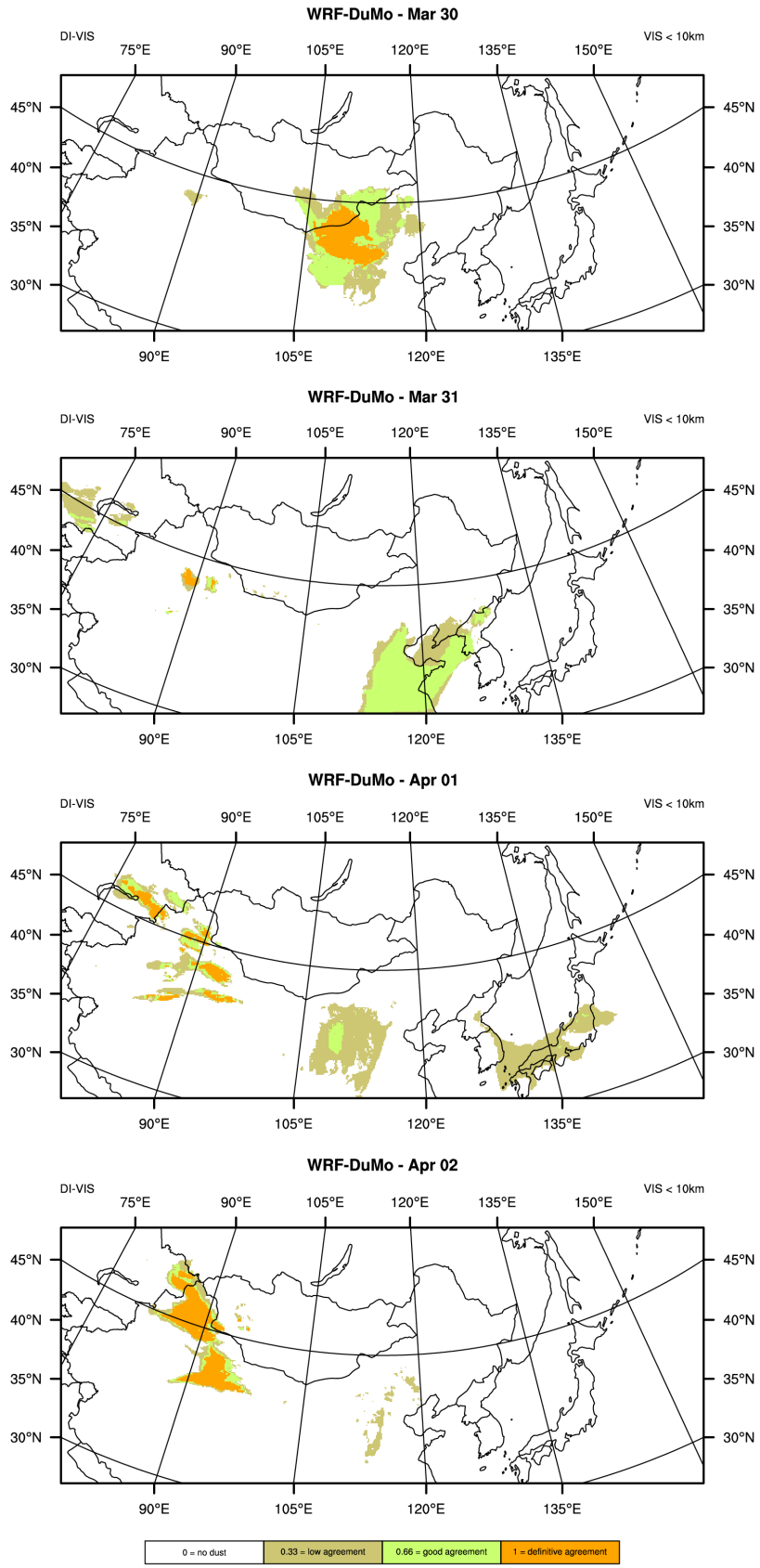

Figure 60: DI_{VIS} for the period 30 March – 2 April, 2007.

For the sake of simplicity, we will consider that the daily OMI-AI represents well enough the daily averaged dust loadings over our domain. OMI-AI values for the period 30 March – 2 April, 2007 are shown in Figure 61 (there are no retrievals on 1 April, 2007). We see that OMI-AI is less patchy compared to MODIS-AOT (see Figure 55) and correctly detects dust presence over the Gobi and along the eastern transport route on 30 and 31 March, 2007. Positive values of OMI-AI are a good indicator for presence of dust and therefore, one can create a dust mask based on the OMI-AI sign.

The DI_{DOT} shown in Figure 59 was calculated considering an ensemble of three modeling experiments, one for each dust production scheme, which are assumed to be equally representative and hence have the same weights. Therefore, one can apply Equation 34 from which it follows that the possible DI_{DOT} values are 0, 0.33, 0.66 and 1. These values correspond to the following categories for dust presence based entirely on the modeling simulations: 0% - no dust, 33% - low agreement, 66% - good agreement, and 100% definite agreement. If no observational data are available, DI_{DOT} in conjunction with the ensemble mean DOT would be the best estimate of the confidence and the value of the DOT fields.

Our approach on integrated analysis of observations and modeling is illustrated in Figures 62 and 63 where OMI-AI was overlayed with DI_{DOT} and the ensemble mean DOT. The darker palette colors indicate the areas where OMI-AI and WRF-DuMo agree on the presence of dust. Agreement between the observations and the model DI increases our confidence that dust is present. We see a very good agreement between WRF-DuMo and OMI over the Gobi and to the north on 30 March, 2007, as well as very good agreement over the Taklamakan and along the mid-range transport on 2 April, 2007. Where OMI-AI is not retrieved (e.g., because of clouds) the modeling is the only source of information.

4.6.2 Recommendations for the development of an integrated dust framework

Our work considered dust events that originated from the East Asia. Dust sources in East Asia have diverse land surface properties. The Taklamakan desert is comprised of sand,

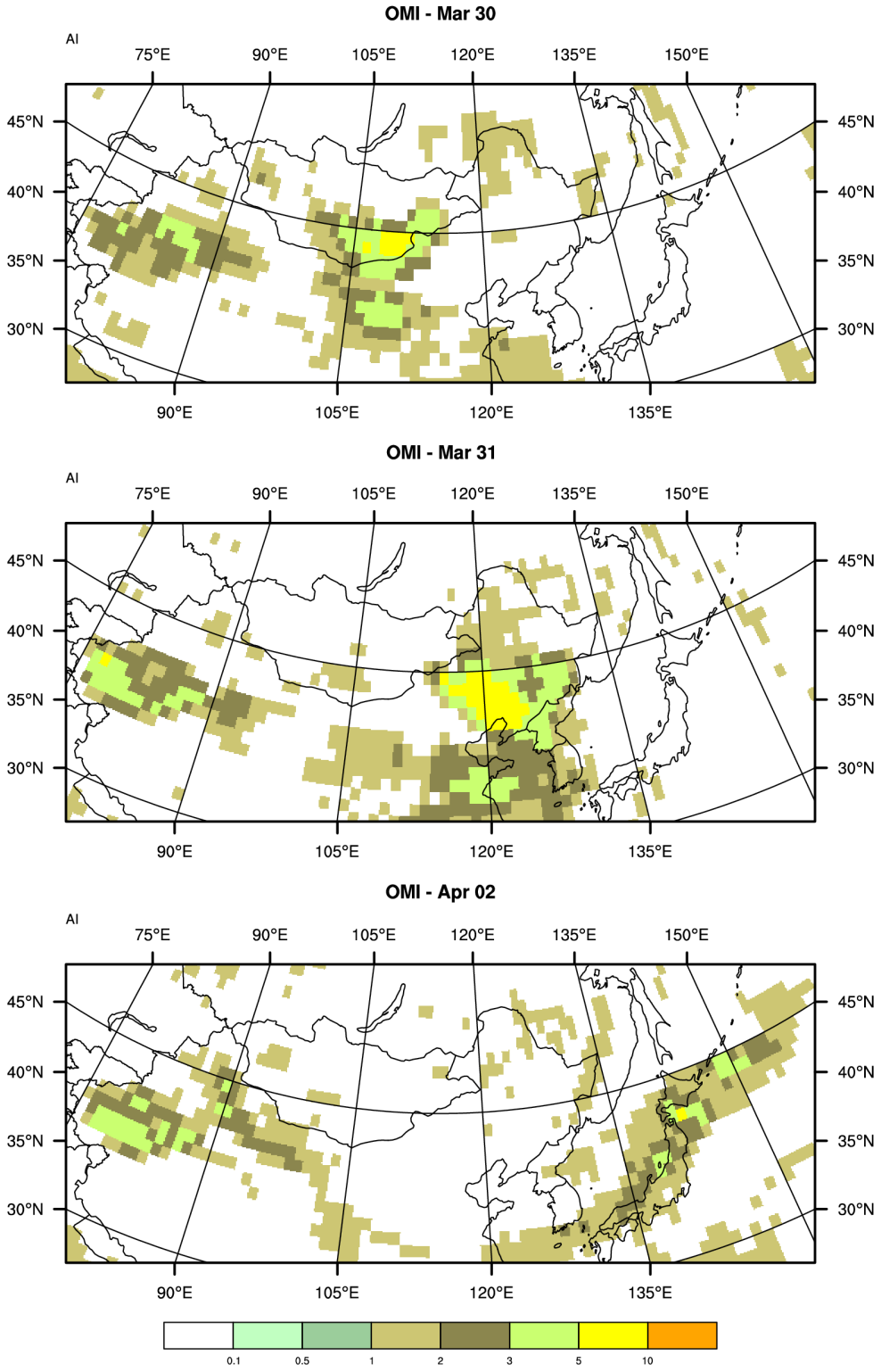

Figure 61: OMI-AI on 30, 31 March and 2 April, 2007.

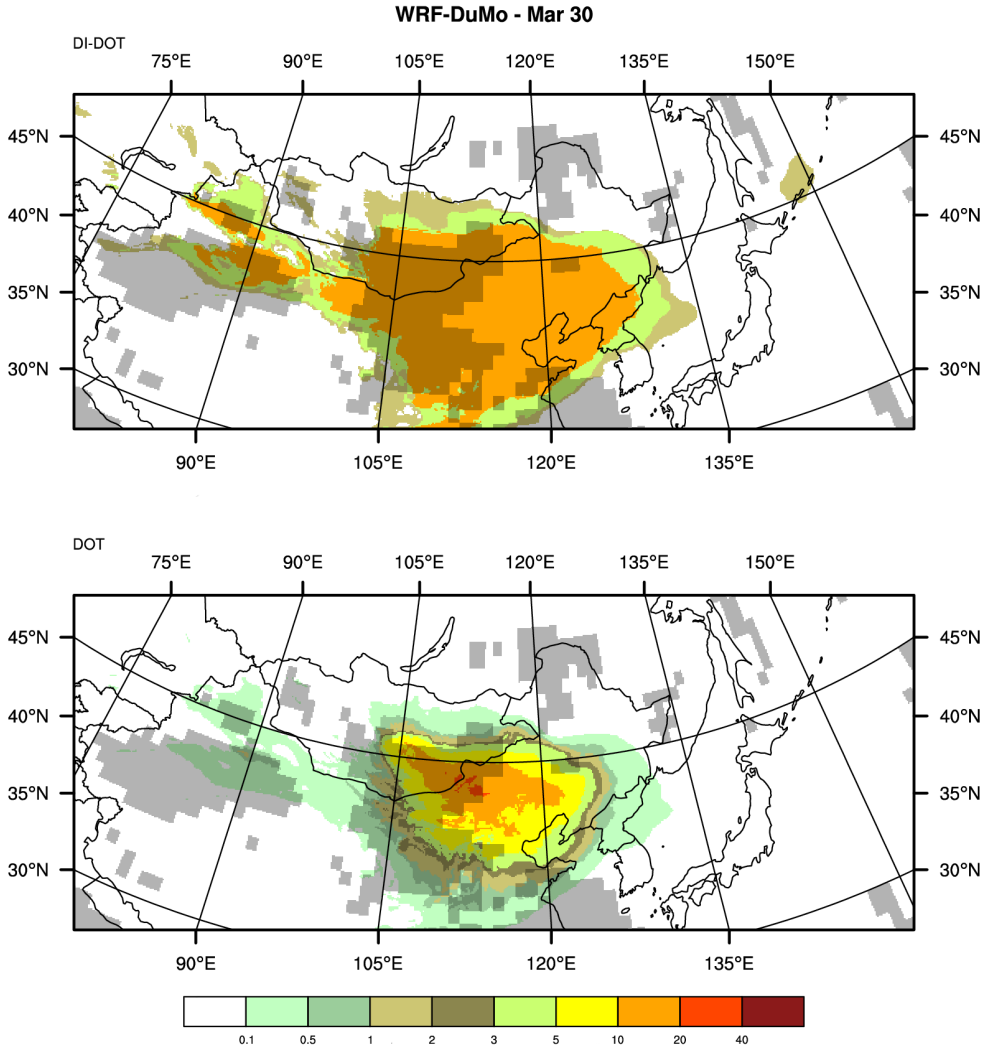

Figure 62: Integrated DI based on OMI-AI and model derived DI_{DOT} (top), and ensemble mean DOT (bottom) on 30 March, 2007.

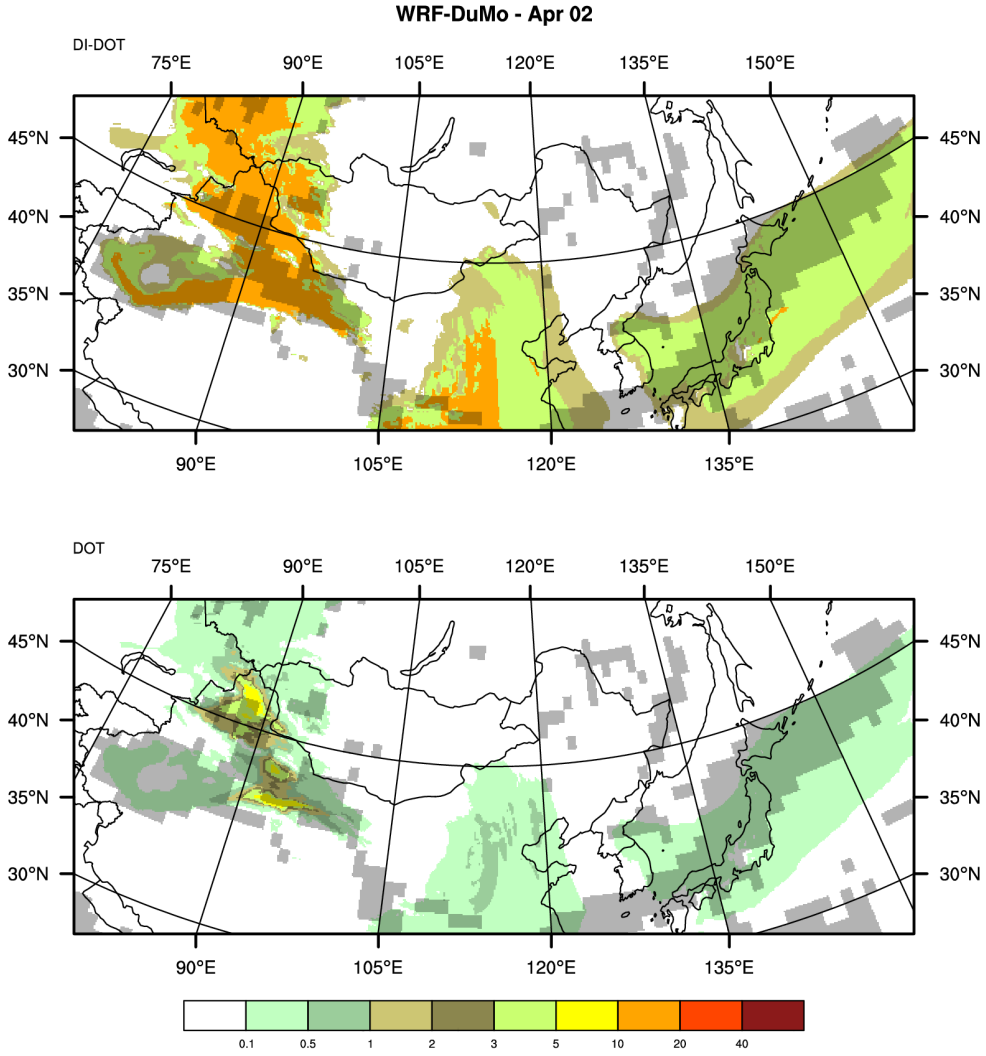

Figure 63: Same as Figure, except for 2 April, 2007.

while the Gobi desert is a complex mixture of sandy lands, gravel surfaces and shurblands. The two physically-based schemes implemented in WRF-DuMo were parameterized against quite different land surface properties. MB95 vertical flux parameterization was developed by using data from the Sahara desert and arid lands in Spain [*Alfaro et al.*, 1998; *Alfaro and Gomes*, 2001], while Shao96 scheme was fitted with data obtained from the Australian deserts [*Shao et al.*, 1996]. In some sense the individual schemes are biased towards surfaces with similar properties for which the parameterizations were derived. Applying the two emission schemes to calculate the emission at location with specific meteorological and surface conditions will result in two different answers. It is difficult to point out which scheme performs better without comparing them to direct emission measurements. It is quite possible that one of the schemes will perform better for some type of sources, while for other sources the other scheme might be a better choice. Therefore, we propose to calculate the best estimate of the vertical dust flux as a linear combination of the MB95 and Shao96 dust fluxes:

$$F = c_{MB95} F_{MB95} + c_{Shao96} F_{Shao96} \tag{39}$$

Furthermore, to match the dust emission scales with the WRF model dynamics scales, we introduce aeolian scaling parameters with which the wind speed u_{WRF} and the soil moisture w_{WRF} from the WRF model need to be adjusted before using them as an input to the emission schemes:

$$u_{DPS} = \alpha u_{WRF} \tag{40}$$

$$w_{DPS} = \beta w_{WRF} \tag{41}$$

$$F_{MB95} = F_{MB95}(u_{DPS}, w_{DPS}) \tag{42}$$

$$F_{Shao96} = F_{Shao96}(u_{DPS}, w_{DPS}) \tag{43}$$

It is not necessary for the parameters c_{MB95} and c_{Shao96}, and the aeolian scaling parameters α and β to have the same values over the simulation domain. If indeed there is a

significant regional difference in the performance of these schemes, the parameters might be source dependent.

The best estimates for the parameter values can be found by performing a minimization against observations such as aerosol optical depth and/or visibility. Because the modeled dust optical depth and visibility greatly depend on the initial dust particle size distribution (see Chapter 2), the parameter values found from the minimization procedure will be specific to a particular model setup. Because the aeolian scale parameters express a general relationship between the model dynamics and the dust emission scales, one can expect that they are uniquely dependent on the source region rather than on the time of the simulation, unless there is a significant seasonal bias in the model meteorology. Hence, it is probably safe to assume that once their values are determined, they can be considered constants. In this way one can effectively decrease the free parameters to only c_{MB95} and c_{Shao96} using the a priori determined values of α and β.

The c_{MB95} and c_{Shao96} parameters can be determined by minimizing the model output and observations for a particular event. If the tuning from the regional to the aeolian scales is good, one can further restrict the possible values by rewriting Equation 39 as

$$F = c[kF_{MB95} + (1 - k)F_{Shao96}] \tag{44}$$

and forcing the parameter c to be close to one. Here the parameter k determines the weight with which each dust production schemes is represented in the best estimate of the model flux, while the parameter c is responsible for fine tuning of the dust emission.

The approach we outlined above will find the best estimate of the dust emission, given the availability of some observations that depend on the size resolved dust concentrations. How unique and realistic is our solution for the dust emission, depends entirely on the available data and the quality of our model. In the absence of dust emission measurements the modeled dust emission will best match observations rather than the true emission. Further more, the solution is not unique, in a sense that it depends on the microphysical properties of the dust particles if the most commonly available data such as AOT and visibility is

used. For example, assuming different size distributions of fresh dust particles will result in different values of the free parameters and hence in different dust emission. The minimization between the modeled output and observations is beneficial because it will allow to seemingly fill the gaps in the data with the best guess values from the model. Merging the modeled dust fields and the particular type of observations involves a post processing of the model output so that it matches the spatiotemporal resolution of the data followed by replacing the missing values with the modeled values.

4.7 Conclusions

Neither standalone numerical dust modeling nor individual aerosol/dust observational datasets can provide a complete and accurate characterization of 3D dust distributions. A logical step in overcoming the limitations of existing data is to merge the model output with the observations thus combining the advantage of the continuous spatiotemporal fields from modeling and the robustness and reliability of the measurements. Despite the straightforwardness of the strategy, its realization poses a challenging problem - from both scientific and technical points of view. Before even attempting to integrate models and observations, one has to test and verify the performance of a dust emission module. The lack of direct measurements of dust fluxes creates an obstacle in testing the dust emission schemes. Using the newly developed WRF-DuMo regional modeling system, we performed a rigorous intercomparison between the modeled visibility and dust optical thickness calculated with MB95, Shao96 and the simple dust emission scheme to assess the role of dust emission parameterizations. We found significant differences in model predicted dust fluxes by individual dust schemes that will require further detailed investigation. Until the discrepancies between the dust schemes remain large any assimilation of observational data at this stage is rather questionable.

In this chapter we proposed an approach for the development of an integrated observational and modeling dust framework. Previous studies attempted minimization/assimilation

of modeling and observations; however, they considered only a simple dust emission scheme, which simplified significantly the minimization problem. In our study we outlined the framework for performing a minimization between measurements and dust emission calculated with the physically-based schemes. We also introduced an ensemble model dust index (MDI), which gives the probability for dust to be present based on the modeled dust optical thickness (or visibility). The MDI also can be used in conjunction with satellite dust retrievals to verify the presence of dust.

Below we summarize our major findings from testing the WRF-DuMo and the integration with observational datasets:

We found that both MB95 and Shao96 schemes are very sensitive to the soil moisture content w. Our modeling experiments showed that WRF predicts larger w in the source regions compared to observations, which can completely shut off the dust emission in the Gobi. Therefore, soil moisture content has to be adjusted when used by the dust emission schemes. Decreasing w value uniformly over the domain by factor of 0.5 gives reasonable values and spatial pattern of emitted dust fluxes.

The cross-correlation analysis of the modeled DOT revealed that over the Inner Mongolia and along the mid-range transport route, dust emission schemes show high positive correlation, because these areas were primarily affected by the strong winds and transport of dust from the Gobi. Over the Taklamakan and Gurban Tunggut deserts and downwind, the correlation is highly variable. These differences can be attributed to the different onset of the dust emission predicted by the schemes. The visibility cross-correlations showed more variability over land compared to DOT cross-correlations. This can be explained by the fact that visibility is a quantitative measure of the dust loadings in the first model layer, which experience highest fluctuations due to the sporadic nature of dust outbursts. Along the transport route we found high correlations, in particular between the visibility from MB95 and Shao96 schemes. Over land, with the exception of the Gobi desert region, we found smaller visibility correlations compared to the DOT correlations.

From the analysis of the modeled DOT and visibility autocorrelations at different time lags, we found that the DOT autocorrelation decreases significantly at lag of about 3 hours, while the visibility autocorrelation decreases significantly at lag of less than 3 hours. The short time period of about 3 hours over which a significant decrease in the autocorrelation was found suggests that the common practice of generating global daily AOT products from near instantaneous AOT granules, retrieved from polar orbiting satellites, may introduce large errors, especially if the global AOT product is used over large geographical areas.

We concluded that the short time, over which time coherency can be achieved, requires that quantitative comparison between satellite AOT and modeled DOT is performed using instantaneous satellite products.

We compared the modeled DOT against CALIPSO FOT and MODIS AOT to identify differences between the modeling and observations. WRF-DuMo reproduces well the dust emission dynamics, however we see that the modeled DOT consistently underestimates the observations over the Taklamakan and during the mid-range transport. Shao96 consistently produces 5 to 7 times smaller DOT than that of the MB95 scheme.

We defined two types of model dust indexes DI_{DOT} and DI_{VIS}, which are representative for dust presence in the vertical column in the atmosphere and at the surface, respectively. These indexes are based on the criterion that dust is present if the modeled DOT/visibility is larger/smaller than a background value. If no observational data are available, DI_{DOT} in conjunction with the ensemble mean DOT would be the best estimate of the confidence that dust is present and the value of the DOT fields. We introduced an integrated dust index based on the integration of OMI-AI and DI_{DOT}. The integrated dust index reflects our confidence that dust is present based on both the observational and modeled data. The best estimate for the DOT remains the ensemble mean DOT.

We outlined a framework for integrating observations and model results. We suggest calculating the best estimate of the vertical dust flux as a linear combination of the MB95 and Shao96 dust fluxes. Furthermore, to match the dust emission scales with the WRF

model dynamics scales, we introduced aeolian scaling parameters, with which the input parameters from the WRF model need to be adjusted before using them as an input into the emission schemes. Finally, the best estimates for the parameter values can be found by performing a minimization against observations such as aerosol optical depth and/or visibility. The minimization between the modeled output and observations is beneficial because it will allow us to seemingly fill the gaps in the data with our best guess values from the model. Merging the modeled dust fields and particular observations involves post processing of the model output so that it matches the spatiotemporal resolution of the data followed by replacing the missing values with the modeled values.

CHAPTER V

CONCLUSIONS

Diverse regionally dependent properties of dust and its complex distribution on large span of spatiotemporal scales render the characterization of dust life cycle a difficult problem. Individual in situ and remote sensing observations provide valuable information about dust aerosols, though they are limited in space and time. On the other hand modeling facilitates quantification of dust fields by providing continuous non-intermittent fields (both in historical and forecast mode) although representation of related physical processes is heavily parameterized and in some instances significantly simplified. Thus, developing an integrated framework that combines the strengths of both modeling and observations and lessens the limitations of individual datasets can greatly benefit the scientific community. The main goal of this study was to improve simulations of mineral aerosols and to explore the capabilities of ground-based and satellite data to aid to characterization of dust in the source areas and downwind. A new coupled regional dust modeling system WRF-DuMo was developed to overcome some important shortcomings of existing models.

The newly developed WRF-DuMo consists of three coupled components: (1) a meteorological modeling system, (2) a terrestrial preprocessor and dust module for emission, injection and optics, and (3) a dust transport-deposition module for simulation of the atmospheric dust evolution. A significant advantage of WRF-DuMo compared to other models is that it includes a suite of simple and physically-based dust emission schemes. Having dust emission schemes with different complexity enables one to bracket the uncertainties in dust simulated fields caused by model-dependent parameterizations and by biases in input parameters. Constraining model uncertainties is critical for the integration of models with observations, which are also subject to errors. WRF-DuMo links the emitted fluxes with

the initial dust size distribution, which can be selected by the modeler or provided by the emission scheme. The injection schemes implemented in WRF-DuMo offer an enhanced flexibility in modeling the vertical distribution and mixing of freshly emitted dust. Different injection schemes can also be used to represent different synoptic conditions during dust events (e.g., migratory anticyclones versus cyclonic circulations).

The advanced capabilities of WRF-DuMo enabled us to perform an in-depth study of the effect of the initial dust size distribution and vertical mixing on 3D spatiotemporal dust fields in the Asian source regions and downwind. In particular, we analyzed the time series of the dust particle MMDs, DOT and visibility during a representative dust outbreak in different locations within source regions and downwind. We found that the effect of initial sizes is more prominent close to dust sources and decreases along the mid- and long-range transport route of the dust plume. The fine mode shows a very weak response to changes in the initial weights in dust source regions. This can be explained by the fact that the dry removal rate of fine particles is negligible compared to the emission rate when the sources are active. Initial weights start to play a role downwind from the sources where their effect becomes comparable to that of the initial size. We also found that the choice of the injection scheme on the modeled dust particle diameters is negligible compared to that of the initial sizes and weights.

We also investigated the effect of the initial size distributions and injection schemes on column integrated quantities (such as dust optical depth) and vertical distribution of the concentrations over the entire simulation domain. Our analysis showed that their magnitude and spatiotemporal distribution is mainly influenced by the selection of the initial dust size distribution. Our numerical experiments show large variability in the modeled dust fields (for instance, one order of magnitude difference in the simulated DOT) in response to changes of ±30% in the initial MMDs and weights. The analyzed column integrated fields showed a weak dependence on the injection scheme. The negligible effect of the initial vertical mixing profile might be a result from the underestimation of the modeled PBL

height over source regions and/or efficient mixing by the WRF PBL scheme.

Our extensive modeling experiments for two representative dust events in East Asia revealed that the selection of the initial size distributions are of critical importance to the modeling of dust fields. It has to be pointed out that the above findings were derived based on dust fluxes calculated with a simple dust emission scheme. However, this conclusion will be relevant in the case of advanced dust emission schemes as well. While the physically based emission schemes do provide size resolved dust fluxes, the amount of mass emitted for a particular size range is parameterized against land surface and meteorological properties that do not necessarily reflect the specific conditions in Central and East Asia. In case that size resolved emission schemes are used, we recommend that a similar sensitivity analysis is performed (in terms of varying the internal parameters of the schemes that control the emission size spectra) to be able to bracket the range of uncertainty in the predicted initial size distributions.

A large extent of this work examined the capability of ground-based and satellite observations to detect and characterize dust in the atmosphere, focusing on the regional signature of dust. We analyzed multi-year MODIS data in the thermal-IR to investigate the radiative signature of atmospheric dust on a regional basis and point out implications to dust detection. Our analysis demonstrated that automated discrimination between cloudy and dusty pixels based on the split-window or the trispectral approach with a fixed BTD threshold that has been used by past studies is not reliable. We concluded that the regional radiative signature of dust observed in the MODIS data is likely due to the different mineralogical composition controlled by the diverse dust sources, although the multilayered vertical distribution may also be important. Thus, one has to consider the origin of atmospheric dust in order to utilize the BT difference techniques in their full potential. In turn, the regional IR signature may be helpful in identifying the origin of dust plumes.

We also examined the discrimination of dust from clouds with solar MODIS channels. A new statistical approach was proposed and tested with multi-year MODIS data of dust

and dust-cloud mixed scenes. In addition to improved discrimination of dust from clouds, it provides information about the skill of the classification (discrimination) unlike the simple yes/no mask that is currently used operationally by many sensors (e.g., MODIS and AVHRR). This is a key advantage over the fixed STD approach because it enables determining the confidence level of the data to be of a certain type, and can be used to evaluate the quality of the retrievals.

In-depth analysis of modeling results and observations over East Asia revealed significant limitations of the individual datasets to describe the regional specifics of dust aerosols. Acknowledging the challenging task of the development of an integrated observational and modeling dust framework we laid out the methodological aspects for synergy of modeling and observations. As a first step, we validated the model dust fields against observations to identify the optimal parameters for the WRF-DuMo model. We found that both physically-based schemes (MB95 and Shao96) are highly sensitive to the soil moisture content w. Our modeling experiments showed that WRF overpredicts w in the dust source regions, which can completely shut off dust emission over the Gobi Desert contrary to the observations. Therefore, we modified the soil moisture content used by the dust emission schemes, decreasing its value uniformly over the domain by a factor of 0.5.

The cross-correlation analysis of the modeled dust optical thickness (DOT), revealed that over the Inner Mongolia and along the mid-range transport route, the dust emission schemes show high positive correlations, because these areas are affected by strong winds. Over the Taklamakan and the Gurban Tunggut deserts and downwind, the correlation patterns are highly variable. Differences between the results from the dust production schemes can be attributed to the differences in the onset of dust emission predicted by the schemes. The cross-correlations of visibility, show higher spatial variability over land compared to cross-correlations of DOT. This can be explained by the fact that visibility is a measure of the dust loadings in the first model layer, which experience the highest fluctuations due to the sporadic nature of dust outbursts. Along the transport route, we found high correlations,

in particular between the visibility from MB95 and Shao96 schemes. Over land, with the exception of the Gobi Desert region, we found smaller visibility correlation compared to the DOT correlations.

From the analysis of the modeled DOT and visibility autocorrelations at different time lags, we found that the DOT autocorrelation decreases significantly at lag of about 3 hours, while the visibility autocorrelation decreases significantly at lag of less than 3 hours. We concluded that the short time, over which time coherency can be achieved, requires that quantitative comparison between satellite aerosol optical thickness (AOT) and modeled DOT should be performed by using instantaneous satellite products.

We also compared the modeled DOT against CALIPSO feature optical thickness (FOT) and MODIS AOT. WRF-DuMo reproduces well the dust emission dynamics, however we found that the modeled DOT underestimates the observations over the Taklamakan and along the mid-range transport. Shao96 consistently produces 5 to 7 times smaller DOT than the DOT obtained with the MB95 scheme.

We defined two types of model dust indexes DI_{DOT} and DI_{VIS}, which are proxies for dust presence in the vertical column in the atmosphere and at the surface, respectively. These indexes are based on the criterion that dust is present when the modeled DOT/visibility is larger/smaller than a background value. If no observational data are available, DI_{DOT} in conjunction with the ensemble mean DOT would be the best estimate of the presence of dust and its loading, respectively. We introduced an integrated dust index based on the integration of OMI-AI and DI_{DOT}. The integrated dust index represents the level of confidence whether dust is present based on the observational and modeled data. The best estimate for the dust optical thickness remains the ensemble mean DOT. We suggest to define the confidence level of the modeled DOT using the ensemble dispersion.

We outlined a framework for integrating observations and modeling. In particular, we suggested calculating the best estimate of the vertical dust flux as a linear combination of the MB95 and Shao96 dust fluxes. Furthermore, to match the dust emission scales with the

WRF model dynamics scales, we introduced aeolian scaling parameters, with which the input parameters from the WRF model need to be adjusted before using them as an input to the emission schemes. Finally, the best estimates of the scaling parameters can be found by performing a minimization against observations, such as aerosol optical depth and/or visibility. The minimization between the modeled output and the observations is beneficial because it will allow to seemingly fill the gaps in the observational data with the best guess values from the model. Merging the modeled dust fields and the particular observations involves post processing of the model output so that it matches the spatiotemporal resolution of the data followed by replacing the missing values with the model predicted values.

Merging modeling and observations seems to be a promising strategy; however, it is greatly impeded by the intrinsic limitations of the individual datasets and the existing differences between the physical parameterizations of dust emission. Integration of dust models, dust observations from fixed surface stations and dust retrievals from space borne platforms can greatly benefit both the models and the observations. The model output can be constrained by the available observations, while assimilation of different data products can be a sound technique for merging independent data sources.

Recommendations:

1. This work showed significant differences in the modeled dust fields as a result of the variation of the parameters of the initial size distributions. Until now very limited observational data on initial size distributions in source regions existed. A database compiling all current measurements is urgently needed for the purpose of dust modeling.

2. Modelers should be aware that different initial size distributions, mixing heights and emission parameterizations can produce significant differences in the model dust fields within a single modeling framework. If modeling intercomparisons are performed additional biases are introduced as a result of different modeling platforms and parameterizations. This also has to be taken into consideration when dust fields

from different models are compared.

3. Develop data assimilation system and optimize the modeled dust emission by assimilating data from satellites and surface stations.

4. The ability of individual dust modeling systems to reproduce land surface and meteorological variables over arid regions should be carefully evaluated.

5. The regional differences of dust need to be taken into account in the next generation of dust detection algorithms.

APPENDIX A

IMPLEMENTATION OF DUST EMISSION SCHEMES IN THE DUST MODULE DUMO

A.0.1 Implementation of simple dust production scheme

In simple dust emission schemes the vertical dust flux is commonly assumed to be directly proportional to the saltation flux and is expressed in the general form as

$$F = CfW, \tag{45}$$

where F is the vertical dust flux, C is the dimensional, scheme-specific constant of proportionality, f is the erodible fraction, and W is the saltation flux. In DuMo vertical dust flux is calculated using the cubic dependence of dust emission on friction velocity:

$$F = CEu_*^3\left(1 - \frac{u_{*t}^3}{u_*^3}\right). \tag{46}$$

where E is the erodible fraction. Currently $u_{*t} = 60\,\mathrm{cm/s}$ and the constant of proportionality $C = 1 \times 10^{-13}\,\mathrm{gs^2cm^{-5}}$ was selected to match the emitted dust mass calculated with the physically based MB95 scheme described below for representative dust events.

It is interesting to note that the constant of proportionality used in previous studies varies by several orders of magnitude (see Table 11), which indicates the significant uncertainty that currently exist in the estimation of regional and global dust loads.

A.0.2 Implementation of Marticorena and Bergametti, 1995 dust production scheme (MB95)

A.0.2.1 Threshold friction velocity

The threshold friction velocity for an arbitrary surface is commonly expressed as:

$$u_{*t}(D, \lambda, w) = \frac{u_{*ts}(D)}{R(\lambda)}H(w) \tag{47}$$

Table 11: Simple dust emission schemes used in previous studies.

Study	C[a]	Dust production scheme
Tegen and Fung [1995]	$0.4–1.2 \times 10^{-9}$	$F = CU_{10}^2(U_{10} - U_{10t})$
Uno et al. [2001]	1×10^{-9}	$F = CU_{10}^2(U_{10} - U_{10t})$
Liu and Westphal [2001]	4.37×10^{-9}	$F = fCU_{10}^2(U_{10} - U_{10t})$
Perlwitz et al. [2001]	$2–5 \times 10^{-9}$	$F = CU_{10}^2(U_{10} - U_{10t})$
Chin et al. [2003]	1×10^{-9}	$F = CS\,s_p U_{10}^2(U_{10} - U_{10t})$
Takemura et al. [2002]	$1.5 \times 10^{-9}\frac{w_t - w}{w_t}$	$F = CU_{10}^2(U_{10} - U_{10t})$
Mukai et al. [2004]	$1.3 \times 10^{-9}\frac{w_t - w}{w_t}$	$F = CU_{10}^2(U_{10} - U_{10t})$
Liu and Westphal [2001]	1.42×10^{-5}	$F = fCu_*^4$
Nickovic et al. [2001]	0.96×10^{-4}	$F = CU_{10}^3(U_{10} - U_{10t})$
Lunt and Valdes [2002]	2.6×10^{-5}	$F = Cc\frac{\rho_a}{g}\left(1 + \frac{u_{*t}}{u_*}\right)\left(1 - \frac{u_{*t}^2}{u_*^2}\right)$

[a] $[C] = kgs^2m^{-5}$ except for *Lunt and Valdes* [2002] where $[C] = m^{-1}$

where $u_{*ts}(D)$ is the threshold friction velocity over a smooth surface, $H(w)$ and $R(\lambda)$ are independent functions accounting for the effect of soil moisture and roughness elements, respectively, and D is the diameter of soil particles. The drag partition correction $R(\lambda)$ accounts for the presence of nonerodible elements (rocks, pebble, vegetation, etc.) in natural land surfaces. The roughness elements decrease the dust emission potential by sheltering the surface from aeolian erosion and by consuming part of the wind momentum otherwise transferred to the erodible surface. The moisture correction $H(w)$ is introduced to account for the suppression of the soil erosion in wet soils due to increased cohesion.

The threshold friction velocity over a smooth surface is calculated following the *Iversen and White* [1982] and *Greeley and Iversen* [1985] approach:

$$u_{*ts}(D) = \begin{cases} \frac{0.129K}{\left(1.928Re^{0.092} - 1\right)^{0.5}} & 0.03 < Re \leq 10 \\ 0.129K\left(1 - 0.0858e^{-0.0617(Re-10)}\right) & Re > 10 \end{cases} \tag{48}$$

Marticorena and Bergametti [1995] parameterized the Reynolds number for typical arid conditions as a power function of particle diameter:

$$Re = aD^X + b \tag{49}$$

The required for the parameterization parameters are given by:

$$\begin{aligned} X &= 1.56 \\ a &= 1331\,\mathrm{cm}^{-\mathrm{X}} \\ b &= 0.38 \\ K &= \left(\frac{2\rho_p g D}{2\rho_a}\right)^{0.5}\left(1+\frac{0.006}{\rho_p g D^{2.5}}\right) \end{aligned} \tag{50}$$

where $\rho_p = 2.65\,\mathrm{g/cm^3}$ and $g = 981\,\mathrm{cm/s^2}$. Air density ρ_a is available from WRF.

A.0.2.2 Roughness correction

To accommodate higher roughness lengths for shrublands, grasslands and agricultural lands we used the *MacKinnon et al.* [2004] formulation of the roughness correction:

$$R(\lambda) = 1 - \frac{ln\left(\frac{z_0}{z_{0s}}\right)}{ln\left[0.7\left(\frac{12225\,\mathrm{cm}}{z_{0s}}\right)^{0.8}\right]} \tag{51}$$

where z_0 and z_{0s} are the aerodynamic roughness length (in cm) and roughness length over smooth surface (in cm) respectively. The latter is assumed to be $1/30$ of the coarser mass median diameter of the soil size distribution [*Marticorena et al.*, 1997].

A.0.2.3 Moisture correction

The *Fécan et al.* [1999] parameterization was applied to account for suppression of soil erosion due to increased soil wetness.

$$H(w) = \begin{cases} 1 & w < w' \\ [1 + 1.21(w - w')0.68]^{-0.5} & w \geq w', \end{cases} \tag{52}$$

where $w'(\%) = 0.0014(\%clay)^2 + 0.17(\%clay)$ is the residual soil moisture and w is the gravimetric soil moisture (in kg/kg).

To convert from gravimetric to volumetric soil moisture the following conversion is applied:

$$w\left[\frac{kg}{kg}\right] = w\left[\frac{m^3}{m^3}\right] \times \frac{\rho_{water}}{\rho_b} \tag{53}$$

The volume percentage clay in the soil is taken from the STATSGO dataset that gives the relative amounts of sand, silt and clay in the < 2 mm fraction of the component layer. The soil bulk density ρ_b is assumed to be equal to $1.42\,\mathrm{g/cm^3}$.

A.0.2.4 Horizontal (saltation) flux

The horizontal dust mass flux or streamwise saltation flux $Q_h(D)$ for uniform sand particles describes the intensity of saltation. Q_h is calculated using the *White* [1979] sand flux equation:

$$Q_h(D) = c\frac{\rho_a}{g}u_*^3\left(1 + \frac{u_{*t}(D)}{u_*}\right)\left(1 - \frac{u_{*t}^2(D)}{u_*}\right), \tag{54}$$

where c is a constant of proportionality equal to 2.61.

The total horizontal (streamwise) sand flux for all particle sizes represents the integral of the size dependent saltation flux $Q_h(D)$ over the relative surface covered by sand particles within the size range D_{smin} and D_{smax}.

$$G(D) = \int_{D_{smin}}^{D_{smax}} c\frac{\rho_a}{g}u_*^3\left(1 + \frac{u_{*t}(D)}{u_*}\right)\left(1 - \frac{u_{*t}^2(D)}{u_*}\right) dS_{rel}(D) \tag{55}$$

A.0.2.5 Vertical flux

The calculation of the vertical dust flux follows the energy-based model of *Alfaro and Gomes* [2001]. To compute the horizontal flux for a given soil particle size:

$$dG(D) = Q(D)dS_{rel}(D), \tag{56}$$

where $dS_{rel}(D)$ is the percentage of soil particles with diameter D relative to the total surface covered by soil particles. Then, the individual kinetic energy of the soil particles with size D is calculated as:

$$dF_{kin}(D) = \beta G(D), \tag{57}$$

where β is an empirically derived parameter equal to $6.300\,\mathrm{cm/s^2}$. For each one of the three dust emission modes (i=1, 2, 3) given in *Alfaro and Gomes* [2001], the vertical dust particle

number flux is computed as:

$$dN_i(D) = dF_{kin}(D)p_i(D)/e_i, \tag{58}$$

where e_i and $p_i(D)$ are the binding energy attached to the emission mode i and fraction of kinetic energy required for the release of dust particle in the ith mode. The latter is calculated by comparing the individual soil particle kinetic energy:

$$e_c(D) = \rho_p \frac{\pi}{12} D^3 \left(20u_*\right)^2, \tag{59}$$

with the binding energy e_i in the ith mode. The last step is the calculation of the mass emission flux for the ith mode:

$$F_i = \frac{\pi}{6}\rho_p D_i^3 N_i, \tag{60}$$

where N_i is the integral of Equation 58 over the soil particle size range. The total vertical flux is represented by the sum of the mass flux for each mode:

$$F = E\left(F_1 + F_2 + F_3\right) \tag{61}$$

A.0.3 Implementation of Shao et al., 1996 dust production scheme (Shao96)

A.0.3.1 Threshold friction velocity

Similarly to MB95 scheme, the threshold friction velocity is calculated as:

$$u_{*t}(D, \lambda, w) = \frac{u_{*ts}(D)}{R} H(w) \tag{62}$$

The threshold friction velocity for a dry (unsheltered) bed of uniform soil particles of size D is calculated following *Shao and Lu* [2000]:

$$u_{*ts}(D) = \sqrt{A_N \left(\frac{\rho_p g D}{\rho_a} + \frac{\Gamma}{\rho_a D}\right)}, \tag{63}$$

where $\Gamma = 3 \times 10^{-4}\,\mathrm{kg/s^2}$, $A_N = 0.0123$, $\rho_p = 2.65\,\mathrm{g/cm^3}$.

A.0.3.2 Roughness correction

We used modified double drag partitioning parameterization (*Shao*, personal communication, *2007*) which accounts for the coexisting solid and porous roughness elements:

$$R(\lambda) = (1-\sigma_V m_V \lambda_V)^{-0.5}(1+m_V\beta_V\lambda_V)^{-0.5} \times \left(1-\sigma_B m_B \frac{\lambda_B}{1-A_V}\right)^{-0.5}\left(1+m_B\beta_B\frac{\lambda_B}{1-A_V}\right)^{-0.5}, \quad (64)$$

where solid obstacles present in bare surface are parameterized by:

$$\beta_B = 90; \quad m_B = 0.5; \quad \sigma_B = 1$$

and vegetation is parameterized by:

$$\beta_B = 202; \quad m_B = 0.26; \quad \sigma_V = 1.45$$

Vegetation lateral cover is given by $\lambda_V = -C_\lambda ln\,(1-A_V)$, where A_V is the WRF model predicted vegetation fraction and C_λ is a coefficient equal to 0.35, that is appropriate for stubble roughness. The solid elements lateral cover is given by a landuse type following the representative values measured by *Marticorena et al.* [2006].

A.0.3.3 Moisture correction

Following *Fécan et al.* [1999] parameterization. For details see Section A.0.2.3.

A.0.3.4 Horizontal (saltation) flux

The horizontal dust mass flux or streamwise saltation flux $Q_h(D)$ for uniform sand particles describes the intensity of saltation. Q_h is calculated using the *Owen* [1964] sand flux equation:

$$Q_h(D) = \begin{cases} c_S(D)\rho_a \frac{u_*^3}{g}\left(1-\frac{u_{*t}^2(D)}{u_{*t}^2}\right) & u_* > u_{*t} \\ 0 & u_* \le u_{*t} \end{cases} \quad (65)$$

where $c_S(D)$ is of order of 1 [*Shao et al.*, 2002].

The total horizontal (streamwise) sand flux for all particle sizes represents the weighted integral of the saltation flux $Q_h(D)$ over all sand particle sizes D_s.

$$G(D) = \int_{D_{smin}}^{D_{smax}} Q(D_s)p(D_s)\delta D_s, \tag{66}$$

where $p(D_s)$ is the geometric area soil particle size distribution.

A.0.3.5 Vertical flux

The Shao vertical flux of dust particles with size D_d induced by bombardment of saltating particles with size D_s is expressed as:

$$\tilde{F}(D_d, D_s) = \alpha(D_d, D_s)Q(D_s), \tag{67}$$

where $\alpha(D_d, D_s)$ is the sandblasting mass efficiency with units of m^{-1} and

$$\alpha(D_d, D_s) = \frac{2}{3}\frac{\rho_p}{\rho_a}\frac{\beta\gamma g}{u_{*t}^2(D_d)}, \tag{68}$$

where γ is a dimensionless constant of 2.5, g is the acceleration of gravity and ρ_p and ρ_a are particle and air density, respectively. $\beta = \beta(D_d, D_s)$ is a dimensionless empirical function of D_d and D_s derived from the wind-tunnel observations of *Shao et al.* [1996] and is expressed as:

$$\beta(D_d, D_s) = \left[0.125 \times 10^{-4} ln(D_s) + 0.328 \times 10^{-4}\right] exp(-140.7D_d + 0.37) \tag{69}$$

with D_d and D_s in millimeters. The dust flux can be estimated as a double integration:

$$F = E \int_{d_1}^{d_2} \int_{0}^{d_1} \tilde{F}(D_d, D_s)p(D_d)p(D_s)\delta D_d \delta D_s \tag{70}$$

where d_1 and d_2 define the saltation particle size range ($d_1 < D_s < d_2$) and $p(D_d)$ and $p(D_s)$ are the mass and surface soil particle size distributions, respectively.

A.0.4 Terrestrial preprocessor

Terrestrial preprocessor consists of several programs that perform regrinding and interpolation of external datasets onto WRF domain grid. The external datasets are: Aeolian

roughness derived from POLDER instrument and undisturbed soil particle size distributions. In addition it also has implemented disturbed USDA soil texture based particle size distributions.

A.0.4.1 Aeolian roughness

Two datasets of Aeolian roughnesses are currently available: Eastern Asia (35.5°– 47° N; 73°– 125° E) and Central Asia (32°– 50° N; 42°– 80° E). The spatial resolution is 1/12, each value is defined at the center of a 1/12°× 1/12° pixel on a cylindrical regular grid. The data is interpolated/regridded in the beginning of each WRF simulation to fill empty values and to for the irregular WRF grid. Three different interpolations are used depending on the number of missing POLDER grid points - nearest neighbor, weighted average and 4-point bilinear interpolation. If the WRF domain borders are outside of the POLDER roughness domains then the default WRF aerodynamic roughness is assigned.

A.0.4.2 USPS distribution

The physically based dust emission schemes require undisturbed dry-sieved soil particle size distributions that better reflect the condition of the erodible surface during wind erosion event. Undisturbed distributions for Central and East Asia are utilized from *Laurent et al.* [2006] and *Petrov* [1976] respectively. The USPS distributions are assigned to individual dust sources in Central and East Asia, which are defined on the basis of their geographical location (latitude, longitude), soil texture, elevation and land use type. Since in situ measurements of USPS distributions are not available for each dust source a geomorphological analogs were used for deserts with similar origin and land properties were assigned the same USPS distributions.

A.0.4.3 USDA distribution

The wet sieved USDA soil particle size distribution is based on soil textures [*Zobler*, 1986; *Zakey et al.*, 2006].

APPENDIX B

NAMELIST OPTIONS CONTROLLING THE DUST MODULE DUMO

WRF-DuMo namelist file contains a block **&dumo** with all DuMo specific options. The following is a description of the DuMo namelist variables. The variables that are function of nest are indicated by (max_dom) following the variable name.

Variable Names	Value	Description
&dumo		
dps_opt (max_dom)	0	no dust emission
	1	simple dust production scheme
	2	MB scheme
	3	Shao scheme
dps_soil_distribution	1	USDA - STATSGO database
	2	USPS - DuMo undisturbed soil database
polder_ea	'./polder_ea_nn.nc'	POLDER roughness over East Asia with filled data gaps
	'./polder_ea.nc'	POLDER roughness over East Asia
polder_ca	'./polder_ca_nn.nc'	POLDER roughness over Central Asia with filled data gaps
	'./polder_ca.nc'	POLDER roughness over Central Asia
soil_properties	'./soil_properties.in'	Soil size distributions file

dps_simple_const (max_dom)	1.e-13	Dimensional constant [g s2 cm-5] of proportionality required by the simple scheme
dps_simple_ust_th (max_dom)	60.0	Threshold friction velocity [cm/s] required by the simple scheme
dps_simple_mapped_sources (max_dom)	.true.	Allow emission from predefined sources for the simple scheme
	.false.	Allow emission from the entire domain for the simple scheme
dps_shao96_dmin	0.e-4	Lower limit of integration for dust sized particles [cm]
dps_shao96_dmax	50.e-4	Upper limit of integration for dust sized particles [cm]
	0	No dust injection in the atmosphere
dis_opt (max_dom)	1	Injection in the first model layer
	2	Homogeneous injection in PBL - in terms of mass concentration
	3	Exponential injection in PBL - in terms of mass concentration
	4	Homogeneous injection in PBL - in terms of mass mixing ratio
dust_ufine_sigma	1.7	Ultra-fine mode geometric standard deviation

dust_fine_sigma	1.7	Fine mode geometric standard deviation
dust_coarse_sigma	1.6	Coarse mode geometric standard deviation
dust_ufine_mmd	0.03e-6	Ultra-fine mode MMD [m]
dust_fine_mmd	1.0e-6	Fine mode MMD [m]
dust_coarse_mmd	5.33e-6	Coarse mode MMD [m]
dust_ufine_weight	0.0	Ultra-fine mode weight
dust_fine_weight	0.2	Fine mode weight
dust_coarse_weight	0.8	Coarse mode weight

POLDER roughness files and the soil properties file are part of DuMo installation and can be found in `$(dumo)/share/fdumo/data/preprocessor/`, where `$(dumo)` is the DuMo installation prefix.

References

Ackerman, S. A. (1997), Remote sensing aerosols using satellite infrared observations, *J. Geophys. Res.*, *102*(D14), 17,069–17,079.

Ackerman, S. A., K. I. Strabala, W. P. Menzel, R. A. Frey, C. C. Moeller, and L. E. Gumley (1998), Discriminating clear-sky from clouds with MODIS, *J. Geophys. Res.*, *103*(D24), 32,141–32,157.

Ackermann, I. J., H. Hass, M. Memmesheimer, A. Ebel, F. S. Binkowski, and U. Shankar (1998), Modal aerosol dynamics model for Europe: development and first applications, *Atmospheric Environment*, *32*(17), doi:10.1016/S1352-2310(98)00006-5.

Ahn, H., S. Park, and L. Chang (2007), Effect of Direct Radiative Forcing of Asian Dust on the Meteorological Fields in East Asia during an Asian Dust Event Period, *Journal of Applied Meteorology and Climatology*, *46*(10), 1655–1681, doi:10.1175/JAM2551.1.

Alexandrov, M. D., A. Marshak, B. Cairns, A. A. Lacis, and B. E. Carlson (2004), Automated cloud screening algorithm for MFRSR data, *Geophys. Res. Lett.*, *31*(4), L04118, doi:10.1029/2003GL019105.

Alfaro, S. C., and L. Gomes (2001), Modeling mineral aerosol production by wind erosion: Emission intensities and aerosol size distributions in source areas, *J. Geophys. Res.*, *106*(D16).

Alfaro, S. C., A. Gaudichet, L. Gomes, and M. Maillé (1998), Mineral Aerosol Production by Wind Erosion: Aerosol Particle Sizes and Binding Energies, *Geophys. Res. Lett.*, *25*(7), 991–994.

Andreae, M., and D. Rosenfeld (2008), Aerosol-cloud-precipitation interactions. Part 1. The nature and sources of cloud-active aerosols, *Earth-Science Reviews*, *89*(1–2), doi: 10.1016/j.earscirev.2008.03.001.

Barnum, B. H., et al. (2004), Forecasting dust storms using the CARMA-dust model and MM5 weather data, *Environmental Modelling & Software*, *19*(2), 129–140, doi:10.1016/S1364-8152(03)00115-4.

Bian, H., and C. S. Zender (2003), Mineral dust and global tropospheric chemistry: Relative roles of photolysis and heterogeneous uptake, *J. Geophys. Res.*, *108*(D21), doi: 10.1029/2002JD003143.

Binkowski, F. S., and U. Shankar (1995), The Regional Particulate Matter Model 1. Model description and preliminary results, *J. Geophys. Res.*, *100*(D12), 26,191–26,209.

Cakmur, R. V., R. L. Miller, and O. Torres (2004), Incorporating the effect of small-scale circulations upon dust emission in an atmospheric general circulation model, *J. Geophys. Res.*, *109*, D07201, doi:10.1029/2003JD004067.

Cakmur, R. V., R. L. Miller, J. Perlwitz, I. V. Geogdzhayev, P. Ginoux, D. Koch, K. E. Kohfeld, I. Tegen, and C. S. Zender (2006), Constraining the magnitude of the global dust cycle by minimizing the difference between a model and observations, *J. Geophys. Res.*, *111*, D06207, doi:10.1029/2005JD005791.

Caquineau, S., A. Gaudichet, L. Gomes, and M. Legrand (2002), Mineralogy of saharan dust transported over northwestern tropical Atlantic Ocean in relation to source regions, *J. Geophys. Res.*, *107*(D15), 4251, doi:10.1029/2000JD000247.

Chiapello, I., G. Bergametti, B. Chatenet, P. Bousquet, F. Dulac, and E. Santos Soares (1997), Origins of African dust transported over the northeastern tropical Atlantic, *J. Geophys. Res.*, *102*(D12), 13,701–13,709.

Chin, M., et al. (2003), A global aerosol model forecast for the ACE-Asia field experiment, *J. Geophys. Res.*, *108*(D23), doi:10.1029/2003JD003642.

Christopher, S. A., J. Wang, Q. Ji, and S.-C. Tsay (2006), Estimation of diurnal shortwave dust aerosol radiative forcing during PRIDE, *J. Geophys. Res.*, *108*(D19), 8596, doi: 10.1029/2002JD002787.

Claquin, T., M. Schulz, and Y. J. Balkanski (1999), Modeling the mineralogy of atmospheric dust sources, *J. Geophys. Res.*, *104*(D18), 22,243–22,256, doi:10.1029/1999JD900416.

Colarco, P. R., et al. (2003), Saharan dust transport to the Caribbean during PRIDE: 2. Transport, vertical profiles, and deposition in simulations of in situ and remote sensing observations, *J. Geophys. Res.*, *108*(D19), doi:10.1029/2002JD002659.

d'Almeida, G. A. (1987), On the Variability of Desert Aerosol Radiative Characteristics, *J. Geophys. Res.*, *92*(D3).

Darmenova, K., I. N. Sokolik, and A. Darmenov (2005), Characterization of east Asian dust outbreaks in the spring of 2001 using ground-based and satellite data, *J. Geophys. Res.*, *110*, D02204, doi:10.1029/2004JD004842.

Darmenova, K., I. N. Sokolik, Y.Shao, B. Marticorena, and G. Bergametti (2008), Development of a physically-based dust emission module within the Weather Research and Forecasting (WRF) model: Assessment of dust emission parameterizations and input parameters for source regions in Central and East Asia, *J. Geophys. Res.*, *submitted*.

DeMott, P. J., K. Sassen, M. R. Poellot, D. Baumgardner, D. C. Rogers, S. D. Brooks, A. J. Prenni, and S. M. Kreidenweis (2003), African dust aerosols as atmospheric ice nuclei, *Geophys. Res. Lett.*, *14*(30), doi:10.1029/2003GL017410.

Di Girolamo, L., et al. (2004), Analysis of Multi-angle Imaging SpectroRadiometer (MISR) aerosol optical depths over greater India during winter 2001–2004, *Geophys. Res. Lett.*, *31*, L23115, doi:10.1029/2004GL021273.

Dunion, J. P., and C. S. Velden (2004), The impact of the Saharan Air Layer on Atlantic tropical cyclone activity, *Bull. Am. Meteorol. Soc.*, *85*(3), 353–365, doi:10.1175/BAMS-85-3-353.

Evan, A. T., J. Dunion, J. A. Foley, A. K. Heidinger, and C. S. Velden (2006a), New evidence for a relationship between Atlantic tropical cyclone activity and African dust outbreaks, *Geophys. Res. Lett.*, *33*, L19813, doi:10.1029/2006GL026408.

Evan, A. T., A. K. Heidinger, and P. Knippertz (2006b), Analysis of winter dust activity off the coast of West Africa using a new 24-year over-water advanced very high resolution radiometer satellite dust climatology, *J. Geophys. Res.*, *111*, D12210, doi:10.1029/2005JD006336.

Evan, A. T., A. K. Heidinger, and M. J. Pavolonis (2006c), Development of a new over-water Advanced Very High Resolution Radiometer dust detection algorithm, *International Journal of Remote Sensing*, *27*(18), 3903–3924, doi:10.1080/01431160600646359.

Evan, A. T., A. K. Heidinger, R. Bennartz, V. Bennington, N. M. Mahowald, H. Corrada-Bravo, C. S. Velden, G. Myhre, and J. P. Kossin (2008), Ocean temperature forcing by aerosols across the atlantic tropical cyclone development region, *Geochem. Geophys. Geosyst.*, *9*, Q05V04, doi:10.1029/2007GC001774.

Fan, S.-M., W. J. Moxim, and H. L. II (2006), Aeolian input of bioavailable iron to the ocean, *Geophys. Res. Lett.*, *33*, L07602, doi:10.1029/2005GL024852.

Fécan, F., B. Marticorena, and G. Bergametti (1999), Parametrization of the increase of the aeolian erosion threshold wind friction velocity due to soil moisture for arid and semi-arid areas, *Annales Geophysicae*, *17*(1), doi:10.1007/s00585-999-0149-7.

Foltz, G., and M. McPhaden (2008), Impact of Saharan Dust on Tropical North Atlantic SST, *Journal of Climate*, *21*(19), doi:10.1175/2008JCLI2232.1.

Foret, G., G. Bergametti, F. Dulac, and L. Menut (2006), An optimized particle size bin scheme for modeling mineral dust aerosol, *J. Geophys. Res.*, *111*, D17310, doi:10.1029/2005JD006797.

Fung, I. Y., S. K. Meyn, I. Tegen, S. C. Doney, J. G. John, and J. K. B. Bishop (2000), Iron supply and demand in the upper ocean, *Global Biogeochemical Cycles*, *14*(1), 281–295.

Gao, Y., S.-M. Fan, and J. L. Sarmiento (2003), Aeolian iron input to the ocean through precipitation scavenging: A modeling perspective and its implication for natural iron fertilization in the ocean, *J. Geophys. Res.*, *108*(D7), doi:10.1029/2002JD002420.

Gong, S. L., and X. Y. Zhang (2008), CUACE/Dust – an integrated system of observation and modeling systems for operational dust forecasting in Asia, *Atmos. Chem. Phys.*, *8*(9).

Gong, S. L., X. Y. Zhang, T. L. Zhao, I. G. McKendry, D. A. Jaffe, and N. M. Lu (2003), Characterization of soil dust aerosol in China and its transport and distribution during 2001 ACE-Asia: 2. Model simulation and validation, *J. Geophys. Res.*, *108*(D9), doi: 10.1029/2002JD002633.

Goudie, A. S., and N. J. Middleton (1992), The changing frequency of dust storms through time, *Climatic Change*, *20*(3), doi:10.1007/BF00139839.

Greeley, R. J., and D. Iversen (1985), *Wind as a Geological Process: On Earth, Mars, Venus and Titan*, Cambridge University Press.

Grell, G. A. G., S. E. Peckham, R. Schmitz, S. A. McKeen, G. Frost, W. C. Skamarock, and B. Eder (2005), Fully coupled "online" chemistry within the WRF model, *Atmospheric Environment*, *39*(37), 6957–6975, doi:10.1016/j.atmosenv.2005.04.027.

Grini, A., P. Tulet, and L. Gomes (2006), Dusty weather forecasts using the MesoNH mesoscale atmospheric model, *J. Geophys. Res.*, *111*, D19205, doi:10.1029/ 2005JD007007.

Guenther, A., P. Zimmerman, and M. Wildermuth (1994), Natural volatile organic compound emission rate estimates for U. S. woodland landscapes, *Atmospheric Environment*, *28*(6), 1197–1210.

Heinold, B., J. Helmert, O. Hellmuth, R. Wolke, A. Ansmann, B. Marticorena, B. Laurent, and I. Tegen (2007), Regional modeling of Saharan dust events using LM-MUSCAT: Model description and case studies, *J. Geophys. Res.*, *112*, D11204, doi: 10.1029/2006JD007443.

Heinold, B., I. Tegen, K. Schepanski, and O. Hellmuth (2008), Dust radiative feedback on saharan boundary layer dynamics and dust mobilization, *Geophys. Res. Lett.*, *35*, L20817, doi:10.1029/2008GL035319.

Hsu, N., S.-C. Tsay, M. King, and J. Herman (2004), Aerosol properties over bright-reflecting source regions, *IEEE Trans. Geosci. Remote Sensing*, *42*(3), 557–569, doi: 10.1109/TGRS.2004.824067.

Hsu, N., S.-C. Tsay, M. King, and J. Herman (2006), Deep Blue Retrievals of Asian Aerosol Properties During ACE-Asia, *IEEE Trans. Geosci. Remote Sensing*, *44*(11), 3180–3195, doi:10.1109/TGRS.2006.879540.

Hu, X. Q., N. M. Lu, T. Niu, and P. Zhang (2008), Operational retrieval of Asian sand and dust storm from FY-2C geostationary meteorological satellite and its application to real time forecast in Asia, *Atmos. Chem. Phys.*, *8*(6), 1649–1659.

Husar, R. B., et al. (2001), Asian dust events of April 1998, *J. Geophys. Res.*, *106*(D16), 18,317–18,330.

Iversen, J. D., and B. R. White (1982), Saltation threshold on earth, mars and venus, *Sedimentology*, *29*(1), 111–119.

Jeong, G.-R., and I. N. Sokolik (2007), Effect of mineral dust aerosols on the photolysis rates in the clean and polluted marine environments, *J. Geophys. Res.*, *112*, D21308, doi:10.1029/2007JD008442.

Kalashnikova, O. V., and R. Kahn (2006), Ability of multiangle remote sensing observations to identify and distinguish mineral dust types: 2. Sensitivity over dark water, *J. Geophys. Res.*, *111*, D11207, doi:10.1029/2005JD006756.

Kalashnikova, O. V., R. Kahn, I. N. Sokolik, and W.-H. Li (2005), Ability of multiangle remote sensing observations to identify and distinguish mineral dust types: Optical models and retrievals of optically thick plumes, *J. Geophys. Res.*, *110*, D18S14, doi: 10.1029/2004JD004550.

Kelly, J. T., C. C. Chuang, and A. S. Wexler (2007), Influence of dust composition on cloud droplet formation, *Atmospheric Environment*, *41*(14), doi:10.1016/j.atmosenv.2006.12.008.

Kohfeld, K. E., R. L. Reynolds, J. D. Pelletier, and B. Nickling (2005), Linking the scales of observation, process, and modeling of dust emissions, *Eos Trans. AGU*, *86*(11), doi: 10.1029/2005EO110005.

Kumar, P., I. N. Sokolik, and A. Nenes (2008), Parameterization of cloud droplet formation for global and regional models: including adsorption activation from insoluble CCN, *Atmos. Chem. Phys. Discuss.*, *8*(4), 16,851–16,890.

Laurent, B., B. Marticorena, G. Bergametti, and F. Mei (2006), Modeling mineral dust emissions from Chinese and Mongolian deserts, *Global and Planetary Change*, *52*(1–4), 121–141, doi:10.1016/j.gloplacha.2006.02.012.

Legrand, M., A. Plana-Fattori, and C. N'Doumé (2001), Satellite detection of dust using the IR imagery of Meteosat, 1, Infrared difference dust index, *J. Geophys. Res.*, *106*(D16), 18,251–18,274.

Levin, Z., A. Teller, E. Ganor, and Y. Yin (2005), On the interactions of mineral dust, sea-salt particles, and clouds: A measurement and modeling study from the Mediterranean Israeli Dust Experiment campaign, *J. Geophys. Res.*, *110*, D20202, doi:10.1029/2005JD005810.

Liu, M., and D. L. Westphal (2001), A study of the sensitivity of simulated mineral dust production to model resolution, *J. Geophys. Res.*, *106*(D16).

Liu, M., D. L. Westphal, S. Wang, A. Shimizu, N. Sugimoto, J. Zhou, and Y. Chen (2003), A high-resolution numerical study of the Asian dust storms of April 2001, *J. Geophys. Res.*, *108*(D23), doi:10.1029/2002JD003178.

Lu, H., and Y. Shao (2001), Toward quantitative prediction of dust storms: an integrated wind erosion modelling system and its applications, *Environmental Modelling & Software*, *16*(3), doi:10.1016/S1364-8152(00)00083-9.

Lu, S., L. Q. X., J. Z., W. M., L. Z., W. F., and S. L. (2007), Mineralogy of Inhalable Particulate Matter (pm_{10}) in the Atmosphere of Beijing, China, *Water, Air, & Soil Pollution*, *186*(1–4), doi:10.1007/s11270-007-9470-5.

Lunt, D. J., and P. J. Valdes (2002), The modern dust cycle: Comparison of model results with observations and study of sensitivities, *Journal of Geophysical Research (Atmospheres)*, *107*, 4669–+, doi:10.1029/2002JD002316.

MacKinnon, D. J., G. D. Clow, R. K. Tigges, R. L. Reynolds, and P. S. Chavez (2004), Comparison of aerodynamically and model-derived roughness lengths (z_0) over diverse surfaces, central Mojave Desert, California, USA, *Geomorphology*, *63*(1–2), doi:10.1016/j.geomorph.2004.03.009.

Mahowald, N. M., and L. M. Kiehl (2003), Mineral aerosol and cloud interactions, *Geophys. Res. Lett.*, *30*(9), 1475, doi:10.1029/2002GL016762.

Mahowald, N. M., A. R. Baker, G. Bergametti, N. Brooks, R. A. Duce, T. D. Jickells, N. Kubilay, J. M. Prospero, and I. Tegen (2005), Atmospheric global dust cycle and iron inputs to the ocean, *Global Biogeochemical Cycles*, *19*, GB4025, doi:10.1029/2004GB002402.

Marticorena, B., and G. Bergametti (1995), Modeling the atmospheric dust cycle: 1. Design of a soil-derived dust emission scheme, *Geophys. Res. Lett.*, *100*(D8).

Marticorena, B., G. Bergametti, B. Aumont, Y. Callot, C. N'Doumé, , and M. Legrand (1997), Modeling the atmospheric dust cycle 2. Simulation of Saharan dust sources, *J. Geophys. Res.*, *102*(D4), 4387–4404.

Marticorena, B., et al. (2006), Surface and aerodynamic roughness in arid and semiarid areas and their relation to radar backscatter coefficient, *J. Geophys. Res. – Earth Surface*, doi:0.1029/2006JF000462.

Martins, J. V., D. Tanré, L. Remer, Y. Kaufman, S. Mattoo, and R. Levy (2002), MODIS cloud screening for remote sensing of aerosols over oceans using spatial variability, *Geophys. Res. Lett.*, *29*(12), 8009, doi:10.1029/2001GL013252.

Menut, L., G. Forêt, and G. Bergametti (2007), Sensitivity of mineral dust concentrations to the model size distribution accuracy, *J. Geophys. Res.*, *112*, D10210, doi:10.1029/2006JD007766.

Miller, R., and I. Tegen (1998), Climate response to Soil Dust Aerosols., *Journal of Climate*, *11*(12).

Miller, R. L., J. Perlwitz, and I. Tegen (2004a), Feedback upon dust emission by dust radiative forcing through the planetary boundary layer, *J. Geophys. Res.*, *109*, D24209, doi:10.1029/2004JD004912.

Miller, R. L., I. Tegen, and J. Perlwitz (2004b), Surface radiative forcing by soil dust aerosols and the hydrologic cycle, *J. Geophys. Res.*, *109*, D04203, doi:10.1029/2003JD004085.

Miller, S. D. (2003), A consolidated technique for enhancing desert dust storms with modis, *Geophys. Res. Lett.*, *30*(20), 2071, doi:10.1029/2003GL018279.

Mukai, M., T. Nakajima, and T. Takemura (2004), A study of long-term trends in mineral dust aerosol distributions in asia using a general circulation model, *J. Geophys. Res.*, *109*(D19204), doi:10.1029/2003JD004270.

Nee, J. B., C.-W. Chiang, H. Hu, S. Hu, and J.-Y. Yu (2007), Lidar measurements of asian dust storms and dust cloud interactions, *J. Geophys. Res.*, *112*, D15202, doi:10.1029/2007JD008476.

Nickovic, S., G. Kallos, A. Papadopoulos, and O. Kakaliagou (2001), A model for prediction of desert dust cycle in the atmosphere, *J. Geophys. Res.*, *106*(D16), 18,113–18,129.

Ooyama, K. V. (1990), A thermodynamic foundation for modeling the moist atmosphere, *Journal of the Atmospheric Sciences*, *47*, 2580–2593.

Owen, P. R. (1964), Saltation of uniform grains in air, *Journal of Fluid Mechanics*, *20*(2), doi:10.1017/S0022112064001173.

Park, S. H., et al. (2007), Simulation of entrainment and transport of dust particles within north america in april 2001 ("red dust episode"), *J. Geophys. Res.*, *112*, D20209, doi:,10.1029/2007JD008443.

Pérez, C., S. Nickovic, G. Pejanovic, J. M. Baldasano, and E. Özsoy (2006), Interactive dust-radiation modeling: A step to improve weather forecasts, *J. Geophys. Res.*, *111*, D16206, doi:10.1029/2005JD006717.

Perlwitz, J., I. Tegen, and R. L. Miller (2001), Interactive soil dust aerosol model in the GISS GCM: 1. Sensitivity of the soil dust cycle to radiative properties of soil dust aerosols, *Journal of Geophysical Research (Atmospheres)*, *106*, 18,167–18,192, doi:10.1029/2000JD900668.

Petrov, M. P. (1976), *Deserts of the World*, New York: Halsted Press (John Wiley & Sons).

Pleim, J., A. Venkatram, and R. Yamartino (1984), ADOM/TADAP model development program. Volume 4: The dry deposition module.

Prata, A. J. (1989), Observations of volcanic ash clouds in the 10–12 μm window using AVHRR/2 data, *International Journal of Remote Sensing*, *10*(4&5), 751–761, doi:10.1080/01431160600975337.

Prata, A. J., and I. F. Grant (2001), Retrieval of microphysical and morphological properties of volcanic ash plumes from satellite data: Application to Mt. Ruapehu, New Zealand, *Q. J. R. Meteorol. Soc.*, *127*(576), 2153–2179, doi:10.1002/qj.49712757615.

Prospero, J. M. (1999), Long-term measurements of the transport of African mineral dust to the southeastern United States: Implications for regional air quality, *J. Geophys. Res.*, *104*(D13), 15,917–15,927.

Prospero, J. M., P. Ginoux, O. Torres, S. E. Nicholson, and T. E. Gill (2002), Environmental characterization of global sources of atmospheric soil dust identified with the NIMBUS 7 Total Ozone Mapping Spectrometer (TOMS) absorbing aerosol product, *Reviews of Geophysics*, *40*(1), 1002, doi:10.1029/2000RG000095.

Qian, W., L. Quan, and S. Shi (2001), Variations of the dust storm in China and its climatic control, *Journal of Climate*, *15*(10), doi:10.1175/1520-0442(2002)015⟨1216:VOTDSI⟩2.0.CO;2.

Remer, L. A., et al. (2005), The MODIS Aerosol Algorithm, Products and Validation, *Journal of the Atmospheric Sciences*, *62*(4), 947–973, doi:10.1175/JAS3385.1.

Rosenfeld, D., Y. Rudich, and R. Lahav (2001), Desert dust suppressing precipitation: A possible desertification feedback loop, *Proceedings of the National Academy of Science*, *98*, 5975–5980.

Rudich, Y., O. Khersonsky, and D. Rosenfeld (2002), Treating clouds with a grain of salt, *Geophys. Res. Lett.*, *29*(22), 2060, doi:10.1029/2002GL016055.

Sassen, K., P. J. DeMott, J. M. Prospero, and M. R. Poellot (2003), Saharan dust storms and indirect aerosol effects on clouds: CRYSTAL-FACE results, *Geophys. Res. Lett.*, *30*(12), doi:10.1029/2003GL017371.

Satake, S., et al. (2004), Characteristics of Asian aerosol transport simulated with a regional-scale chemical transport model during the ACE-Asia observation, *J. Geophys. Res.*, *109*, D19S22, doi:10.1029/2003JD003997.

Seinfeld, J., and S. Pandis (1998), *Atmospheric Chemistry and Physics: From Air Pollution to Climate Change*, John Wilsey & Sons, New York, USA.

Shao, Y. (2001), A model for mineral dust emission, *J. Geophys. Res.*, *106*(D17), 20,239–20,254.

Shao, Y. (2004), Simplification of a dust emission scheme and comparison with data, *J. Geophys. Res.*, *109*, D10202, doi:10.1029/2003JD004372.

Shao, Y., and C. Dong (2006), A review on east asian dust storm climate, modelling and monitoring, *Global and Planetary Change*, *52*(1–4), 1–22, doi:10.1016/j.gloplacha.2006.02.011.

Shao, Y., and H. Lu (2000), A simple expression for wind erosion threshold friction velocity, *J. Geophys. Res.*, *105*(D17), 22,437–22,443.

Shao, Y., M. R. Raupach, and J. F. Leys (1996), A model for predicting aeolian sand drift and dust entrainment on scales from paddock to region, *Australian Journal of Soil Research*, *34*(3), 309–342.

Shao, Y., E. Jung, and L. M. Leslie (2002), Numerical prediction of northeast Asian dust storms using an integrated wind erosion modeling system, *J. Geophys. Res.*, *107*(D24), 4814, doi:10.1029/2001JD001493.

Simpson, D., A. Guenther, C. N. Hewitt, and R. Steinbrecher (1995), Biogenic emissions in europe 1. estimates and uncertainties, *J. Geophys. Res.*, *100*(D11), 22,875–22,890.

Slinn, S., and W. Slinn (1980), Prediction for particle deposition on natural waters, *Atmospheric Environment*, *14*, 1013–1016.

Sokolik, I. N. (2002), The spectral radiative signature of wind-blown mineral dust: Implications for remote sensing in the thermal IR region, *Geophys. Res. Lett.*, *29*(24), 2154, doi:10.1029/2002GL015910.

Sokolik, I. N., and O. B. Toon (1996), Direct radiative forcing by anthropogenic airborne mineral aerosols, *Nature*, *381*, 681–683.

Sokolik, I. N., O. B. Toon, and R. W. Bergstrom (1998), Modeling the radiative characteristics of airborne mineral aerosols at infrared wavelengths, *J. Geophys. Res.*, *103*(D8), 8813–8826, doi:10.1029/98JD00049.

Sokolik, I. N., D. M. Winker, G. Bergametti, D. A. Gillette, G. Carmichael, Y. J. Kaufman, L. Gomes, L. Schuetz, and J. E. Penner (2001), Introduction to special section: Outstanding problems in quantifying the radiative impacts of mineral dust, *J. Geophys. Res.*, *106*(D16), 18,015–18,027.

Stier, P., et al. (2005), The aerosol-climate model ECHAM5-HAM, *Atmos. Chem. Phys.*, *11*(4).

Sun, J., M. Zhang, and T. Liu (2001), Spatial and temporal characteristics of dust storms in China and its surrounding regions, 1960–1999: Relations to source area and climate, *J. Geophys. Res.*, *106*(D10), 10,325–10,333.

Sun, J., L. Zhao, S. Zhao, and R. Zhang (2006), An integrated dust storm prediction system suitable for east Asia and its simulation results, *Global and Planetary Change*, *52*(1–4), 71–87, doi:10.1016/j.gloplacha.2006.02.005.

Takemura, T., I. Uno, T. Nakajima, A. Higurashi, and I. Sano (2002), Modeling study of long-range transport of asian dust and anthropogenic aerosols from East Asia, *Geophys. Res. Lett.*, *29*(24), doi:10.1029/2002GL016251.

Tang, Y., et al. (2004), Impacts of dust on regional tropospheric chemistry during the ACE-Asia experiment: A model study with observations, *J. Geophys. Res.*, *109*, D19S21, doi:10.1029/2003JD003806.

Tanré, D., et al. (2003), Measurement and modeling of the Saharan dust radiative impact: Overview of the Saharan Dust Experiment (SHADE), *J. Geophys. Res.*, *108*(D18), 8574, doi:10.1029/2002JD003273.

Tegen, I. (2003), Modeling the mineral dust aerosol cycle in the climate system, *Quaternary Science Reviews*, *22*(18–19), 1821–1834, doi:10.1016/S0277-3791(03)00163-X.

Tegen, I., and I. Fung (1995), Contribution to the atmospheric mineral aerosol load from land surface modification, *J. Geophys. Res.*, *100*, 18,707–18,726.

Uno, I., H. Amano, S. Emori, K. Kinoshita, I. Matsui, and N. Sugimoto (2001), Trans-pacific yellow sand transport observed in april 1998: A numerical simulation, *J. Geophys. Res.*, *106*(D16).

Uno, I., K. Yumimoto, A. Shimizu, Y. Hara, N. Sugimoto, Z. Wang, Z. Liu, and D. M. Winker (2008), 3d structure of asian dust transport revealed by calipso lidar and a 4dvar dust model, *Geophys. Res. Lett.*, *35*, L06803, doi:10.1029/2007GL032329.

Uno, I., et al. (2003), Regional chemical weather forecasting system CFORS: Model descriptions and analysis of surface observations at Japanese island stations during the ACE-Asia experiment, *J. Geophys. Res.*, *108*(D23), doi:10.1029/2002JD002845.

Uno, I., et al. (2004), Numerical study of Asian dust transport during the springtime of 2001 simulated with the Chemical Weather Forecasting System (CFORS) model, *J. Geophys. Res.*, *109*, D19S24, doi:10.1029/2003JD004222.

Uno, I., et al. (2006), Dust model intercomparison (DMIP) study over Asia: Overview, *J. Geophys. Res.*, *111*, D12213, doi:10.1029/2005JD006575.

Wang, Y. Q., X. Y. Zhang, S. L. Gong, C. H. Zhou, X. Q. Hu, H. L. Liu, T. Niu, and Y. Q. Yang (2008), Surface observation of sand and dust storm in East Asia and its application in CUACE/Dust, *Atmos. Chem. Phys.*, *8*(3), 545–553.

Warner, T. T. (2004), *Desert Meteorology*, Cambridge Univ. Press.

Wesley, M. (1989), Parameterization of surface resistances to gaseous dry deposition in regional scale numerical models, *Atmospheric Environment*, *23*, 1293–1304.

White, B. (1979), Soil transport by winds on mars, *J. Geophys. Res.*, *84*.

Wilks, D. S. (2005), *Statistical Methods in the Atmospheric Sciences*, *International Geophysics*, vol. 91, second edition ed., Academic Press, ISBN-10: 0127519661, ISBN-13: 978-0127519661.

Yin, Y., S. Wurzler, Z. Levin, and T. G. Reisin (2002), Interactions of mineral dust particles and clouds: Effects on precipitation and cloud optical properties, *J. Geophys. Res.*, *107*(D23), 4724, doi:10.1029/2001JD001544.

Yoshioka, M., N. M. Mahowald, A. J. Conley, W. D. Collins, D. W. Fillmore, C. S. Zender, and D. B. Coleman (2007), Impact of Desert Dust Radiative Forcing on Sahel Precipitation: Relative Importance of Dust Compared to Sea Surface Temperature Variations, Vegetation Changes, and Greenhouse Gas Warming, *Journal of Climate*, *20*(8), 1445–1467, doi:10.1175/JCLI4056.1.

Yumimoto, K., I. Uno, N. Sugimoto, A. Shimizu, and S. Satake (2007), Adjoint inverse modeling of dust emission and transport over east asia, *Geophys. Res. Lett.*, *34*, L08806, doi:10.1029/2006GL028551.

Zakey, A. S., F. Solmon, and F. Giorgi (2006), Implementation and testing of a desert dust module in a regional climate model, *Atmos. Chem. Phys.*, *6*(12), 4687–4704.

Zender, C. S., H. Bian, and D. Newman (2003), The mineral Dust Entrainment and Deposition (DEAD) model: Description and 1990s dust climatology, *J. Geophys. Res.*, *108*(D14), 10.1029/2002JD002775.

Zhang, X. Y., et al. (2003), Characterization of soil dust aerosol in China and its transport and distribution during 2001 ACE-Asia: 1. Network observations, *J. Geophys. Res.*, *108*(D9), doi:10.1029/2002JD002632.

Zhao, T. L., S. L. Gong, X. Y. Zhang, A. Abdel-Mawgoud, and Y. P. Shao (2006), An assessment of dust emission schemes in modeling east Asian dust storms, *J. Geophys. Res.*, *111*, D05S90, doi:10.1029/2004JD005746.

Zhu, A., V. Ramanathan, F. Li, and D. Kim (2007), Dust plumes over the Pacific, Indian, and Atlantic oceans: Climatology and radiative impact, *J. Geophys. Res.*, *112*, D16208, doi:10.1029/2007JD008427.

Zobler, L. A. (1986), World soil file for global climate modeling, *Tech. rep.*

VITA

Anton Darmenov was born in 1974 in Kazanlak, Bulgaria, where he finished high school specializing in mathematics and natural sciences in 1993. He attended Sofia University, Bulgaria for his Masters degree. Anton acquired a M.Sc. in Physics in 1998 with specialization in Nuclear Physics and Elementary Particles. He moved to Columbus, Ohio, USA, in 2000, where he worked as a research scientist at the Scientific Forming Technologies, Inc. In the spring of 2002, Anton moved to Boulder, Colorado to pursue his Ph.D. in atmospheric sciences at the University of Colorado. He transferred to the Georgia Institute of Technology in 2003 and he acquired Ph.D. in atmospheric sciences in May 2009. His research interests include remote sensing, cloud-aerosol interactions and atmospheric aerosol physics with a focus on mineral dust and regional modeling.